

**Structural and magnetic properties  
of ultrathin Fe<sub>3</sub>Si layers  
epitaxially grown on GaAs(001) and GaAs(110)**

DISSERTATION

zur

Erlangung des Grades

„Doktor der Naturwissenschaften“

an der Fakultät für Physik und Astronomie  
der Ruhr-Universität Bochum

von

Sani Noor

aus

Düsseldorf

Bochum 2013

1. Gutachter: Prof. Dr. Ulrich Köhler
2. Gutachter: PD Dr. Oleg Petracic
- Datum der Disputation: 13.6.2013

# List of abbreviations

AFM	Atomic force microscope
AMR	Anisotropic magnetoresistance
ARMCO	American Rolling Mill Company
CEO	Cleaved edge overgrowth
CTR	Crystal truncation rod
CVD	Chemical vapour deposition
DCXRD	Double crystal x-ray diffraction
DFT	Density functional theory
DMS	Diluted magnetic semiconductor
DPSS	Diode-pumped solid-state
FC	Field-cooled
fcc	Face-centred cubic
FM	Ferromagnet
FMR	Ferromagnetic resonance
GMR	Giant magnetoresistance
IBA	Ion bombardment and annealing
IGP	Ion getter pump
LEED	Low energy electron diffraction
LDOS	Local density of states
LED	Light emitting diode
LMOKE	Longitudinal magneto-optical Kerr effect
MBE	Molecular beam epitaxy
ML	Monolayer
MOKE	Magneto-optical Kerr effect
MRAM	Magnetoresistive random-access memory
PEM	Photoelastic modulator
QMA	Quadrupole mass analyzer
QMOKE	Quadratic magneto-optical Kerr effect
RBS	Rutherford backscattering spectrometry
rf SQUID	radio frequency SQUID

RHEED	Reflection high energy electron diffraction
RMS	Root mean square
RTA	Rapid thermal annealing
SC	Semiconductor
SEM	Scanning electron microscope
SPM	Superparamagnetism
SQUID	Superconducting quantum interference device
STM	Scanning tunnelling microscope
TMP	Turbo molecular pump
TMR	Tunnel magnetoresistance
TSP	Titanium sublimation pump
UMA	Uniaxial magnetic anisotropy
XPS	X-ray photoelectron spectroscopy
XRD	X-ray diffraction
ZFC	Zero-field-cooled

# Contents

<b>List of abbreviations</b>	<b>i</b>
<b>1 Introduction</b>	<b>1</b>
1.1 Review of literature . . . . .	2
1.2 Outline and structure . . . . .	6
<b>2 Theoretical aspects</b>	<b>9</b>
2.1 Thin film growth . . . . .	9
2.1.1 Energetic considerations . . . . .	9
2.1.2 Growth kinetics . . . . .	10
2.2 Magnetism of thin films . . . . .	14
2.2.1 Ferromagnetism . . . . .	14
2.2.2 Superparamagnetism . . . . .	22
<b>3 Experimental methods</b>	<b>25</b>
3.1 STM . . . . .	25
3.1.1 Theory of STM . . . . .	25
3.1.2 Experimental aspects of STM . . . . .	30
3.2 LEED . . . . .	30
3.3 MOKE . . . . .	33
3.4 SQUID . . . . .	40
3.5 FMR . . . . .	42
3.6 RBS . . . . .	43
<b>4 Experimental setups</b>	<b>45</b>
4.1 The existing UHV setup . . . . .	45
4.1.1 MBE sources . . . . .	47
4.1.2 The STM setup . . . . .	49
4.1.3 Sample holders . . . . .	50
4.2 Modifications of the experimental setup . . . . .	52
4.2.1 Electron beam Si evaporator . . . . .	53

4.2.2	MOKE/MBE chamber with cryostat . . . . .	56
4.3	Supplementary external setups . . . . .	63
<b>5</b>	<b>Fe<sub>3</sub>Si/GaAs(001)</b>	<b>65</b>
5.1	GaAs and its (001) surface . . . . .	65
5.2	Optimizing the layer morphology . . . . .	70
5.3	Atomic scale analysis . . . . .	78
5.3.1	The atomic structure . . . . .	78
5.3.2	Defects . . . . .	82
5.4	Magnetic behaviour of closed Fe <sub>3</sub> Si films . . . . .	86
5.4.1	In situ characterization . . . . .	86
5.4.2	Magnetic moments . . . . .	95
5.4.3	Quantitative analysis of the magnetic anisotropies . . . . .	97
5.5	Fe <sub>3</sub> Si/GaAs(001) at low coverage . . . . .	101
5.5.1	The structure and morphology at low coverage . . . . .	101
5.5.2	Magnetic behaviour at low coverage . . . . .	102
5.6	Structural and magnetic correlations . . . . .	105
<b>6</b>	<b>Fe<sub>3</sub>Si/GaAs(110)</b>	<b>107</b>
6.1	The (110) surface of GaAs . . . . .	108
6.2	Structural properties . . . . .	109
6.2.1	Surface morphology of closed layers . . . . .	109
6.2.2	Atomic arrangement . . . . .	111
6.3	Magnetic characterization . . . . .	112
<b>7</b>	<b>Summary, conclusion and outlook</b>	<b>117</b>
	<b>Bibliography</b>	<b>123</b>
	<b>Curriculum vitæ</b>	<b>131</b>
	<b>Acknowledgement</b>	<b>133</b>

# Chapter 1

## Introduction

The subject of this thesis is of fundamental interest to surface physics and thin film magnetism while at the same time it is embedded within spin-electronics also known as spintronics or magnetoelectronics. This field of study exploits the spin properties of electrons and aims at the fabrication of logical circuits in which the spins can be transported, manipulated and detected. While the anisotropic magnetoresistance (AMR) can be considered as the magnetoelectronic phenomenon discovered first, dating back to the 19<sup>th</sup> century, spintronics has attracted significantly more attention since the discovery of the tunnel magnetoresistance (TMR) [Jul75] and the giant magnetoresistance (GMR) [Bai88, Bin89]. This can undoubtedly be ascribed to the significance of these effects for technological applications such as MRAM, hard disks read heads or other sensors that use the field dependence of the electric resistance of magnetic heterostructures.

For other spintronic devices such as spin LEDs, which can be used e.g. for the optical modulation in communication systems, it is essential to generate spin-polarized carrier concentrations in semiconductor structures. This can be done in various ways where the most popular employ optical pumping with circularly polarized light or electrical pumping with a spin-polarized current. Another approach makes use of diluted magnetic semiconductors (DMS), materials which exhibit both ferromagnetic and semiconducting properties. While optical pumping is not practical for many applications, the spin injection by means of DMS such as  $\text{Ga}_{1-x}\text{Mn}_x\text{As}$  remains limited to low temperatures. In fact, the highest Curie temperature that could be reached up to now amounts to 173 K [Ohn98]. An overview of the spin injection efficiencies that could be attained for a selection of spin injection contact-semiconductor combinations is given in [Hol07].

Due to the limitations of the other approaches, electrical pumping with spin-polarized currents via ferromagnetic contacts is therefore a promising method that has been the subject of many studies. Typically, ferromagnetic metals are used as contacts. However, a number of requirements is imposed on the spin injection layer in conjunction with the semiconducting LED heterostructure and on the spin injection layer itself. These include a high interface quality, a high degree of spin polarization, thermal stability and a low conduc-

tivity mismatch between the ferromagnetic layer and the semiconductor. One approach to circumvent the limit set by the conductivity mismatch is the use of tunnel contacts [Ras00]. Another approach makes use of half-metallic materials such as Heusler alloys. Heusler alloys, of which a comprehensive review can be found in [Web69], are furthermore known to exhibit high thermal stability and, due to their half-metallic nature, a theoretical spin polarization of 100 %.

One of these Heusler alloys is  $\text{Fe}_3\text{Si}$ , also known as suessite after H. E. Suess, which as a natural occurrence was first discovered in 1982 as a result of the chemical analysis of a meteorite found in The North Haig (Australia) [Kei82]. In contrast to most other Heusler alloys  $\text{Fe}_3\text{Si}$  is not a ternary but a binary compound which facilitates its growth.

The ferromagnet/semiconductor (FM/SC) combination  $\text{Fe}_3\text{Si}/\text{GaAs}$  is a promising candidate for a spin injection structure as it is augured to fulfil the above mentioned requirements. Section 1.1 summarizes properties of this system according to reports found in the literature. An outline including the objectives and the structure of this work is given in section 1.2.

## 1.1 Review of literature

The Heusler alloy  $\text{Fe}_3\text{Si}$  and the FM/SC combination  $\text{Fe}_3\text{Si}/\text{GaAs}$  are systems of which many aspects have been subject to previous studies. Their prominent features, experimental findings but especially the properties relevant to this work will be summarized in this section based on a review of literature.

$\text{Fe}_3\text{Si}$  is a Heusler alloy crystallizing in the  $\text{D0}_3$  structure of which the unit cell is shown in figure 1.1. It consists of four interpenetrating fcc sublattices which are shifted in steps of  $\sqrt{3}/4 a$  along the  $[111]$  direction where  $a$  is the lattice constant amounting to 0.5642 nm [Ion05a]. Three of these sublattices are occupied by Fe and one by Si atoms. Because two of the Fe sublattices (Fe(A) and Fe(C)) are both crystallographically and also magnetically equivalent, the system can be written as  $(\text{Fe}_A)_2\text{Fe}_B\text{Si}$  or in a similar notation. As determined from XPS analyses [Bus97] the surface of  $\text{Fe}_3\text{Si}$  can be stabilized by the segregation of silicon to the surface leading to a CsCl structure of the iron silicide for the top two monolayers and an additional formation of a  $c(2 \times 2)$  arrangement of silicon atoms at the top. However, these stabilization mechanisms require annealing temperatures of 700 K and 880 K, respectively. Therefore, they do not play a vital role for most  $\text{Fe}_3\text{Si}/\text{GaAs}$  applications. The definition of a monolayer of (001)-oriented  $\text{Fe}_3\text{Si}$  is given by one intensity oscillation measured by diffractive methods such as XRD or RHEED during growth or by single step heights observed in AFM scans both of which occur at multiples of  $a/2$  which is 0.2821 nm [Kag08, Kag09]. The sublattices of bulk  $\text{Fe}_3\text{Si}$  are known to have magnetic moments of  $1.35 \mu_B$  for Fe(A,C),  $2.2 \mu_B$  for Fe(B) and a slightly diamagnetic contribution of  $-0.07 \mu_B$  in the case of Si yielding an average magnetic moment of  $1.175 \mu_B$  per atom

at 6.5 K [Hin76]. Its Curie temperature amounts to 840 K [Len06] which, as is typical for all Heusler alloys, is quite high. One property that makes these Heusler alloys interesting with regard to possible spin injections experiments and applications in conjunction with semiconductors is their half-metallicity or at least quasi half-metallicity which is the case for most full Heusler alloys.  $\text{Fe}_3\text{Si}$  for instance exhibits a pseudo-gap for the minority-spin density of states at the Fermi energy. Although the spin polarization only amounts to 43 % [Ion05b] which is comparable to that of bulk Fe [Sou98] there are other properties which will also be discussed in the following that make the growth of  $\text{Fe}_3\text{Si}$  on GaAs favourable compared to pure FM/SC combinations.

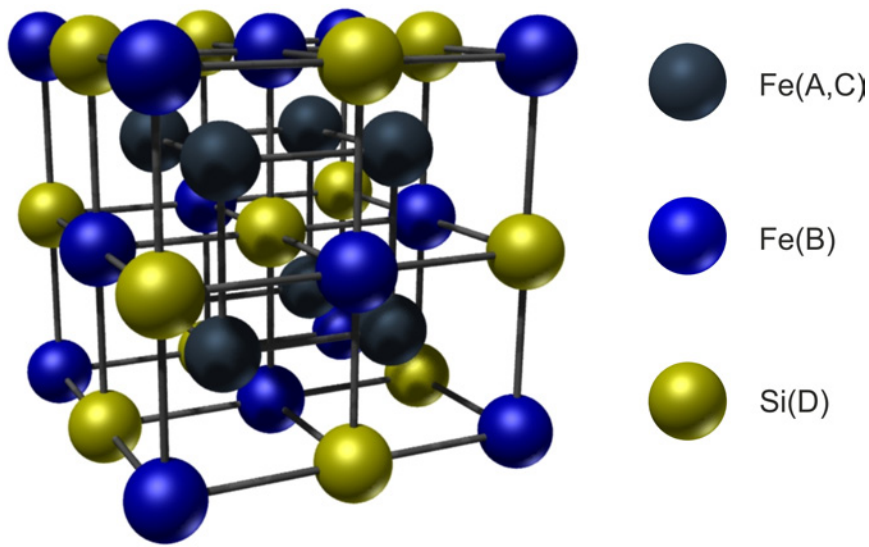


Figure 1.1: Unit cell of the  $\text{D0}_3$  structure of  $\text{Fe}_3\text{Si}$ .

One interesting property of the system  $\text{Fe}_3\text{Si}/\text{GaAs}$  is the low lattice mismatch of 0.2% at stoichiometry which is a good premise for epitaxial growth. From the observation of RHEED patterns the epitaxial relation between the adsorbate and (001)-oriented GaAs substrates is known to be  $(001)[110]\text{GaAs}|| (001)[110]\text{Fe}_3\text{Si}$  [Her04]. In the range of 10 to 30 at.% Si content the lattice mismatch shows a linear dependence on the composition of the iron silicide [Her03] which is used in many studies to determine deviations from stoichiometry. For the growth of  $\text{Fe}_3\text{Si}$  on GaAs, which is usually done by the co-evaporation of Fe and Si, a number of parameters, namely the growth rate, the growth temperature, the layer thickness, surface reconstructions of the substrate and the composition of the iron silicide, must be considered. Compared to other Heusler alloys such as  $\text{Co}_2\text{MnSi}$  the growth of  $\text{Fe}_3\text{Si}$  is relatively easy to control due to its binary nature and the wide range of the  $\text{D0}_3$  structure which covers silicon contents from 10 to 26.6 at.% [Kub82]. This is also illustrated in the iron-silicide phase diagram shown in figure 1.2. Although most studies, including this thesis, consider  $\text{Fe}_3\text{Si}$  films close to stoichiometry because these exhibit the highest degree

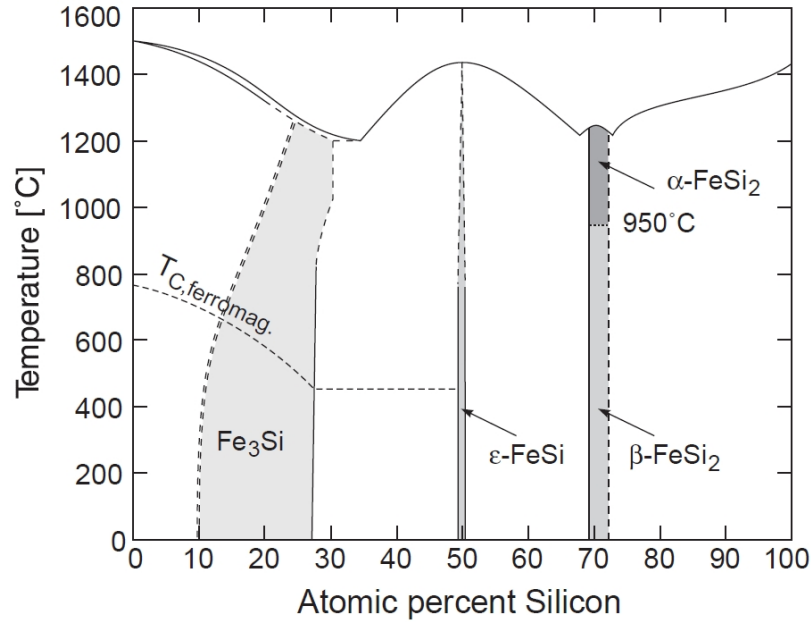


Figure 1.2: Phase diagram iron silicides [Sta01].

of interatomic ordering (for a detailed analysis of the influence of composition on the order parameters the reader is referred to [Jen05]) it is worthwhile to mention that certain properties such as the resistivity, which can be used to alter the FM/SC impedance mismatch, or the magnetic anisotropy can be tuned by changing the composition [Jen05, Her04, Len05]. Moreover, it has also been shown that the magnetic moments of the Fe sublattices can be tuned by the introduction of transition metal impurities into the  $\text{Fe}_3\text{Si}$  matrix [Pic75]. The interatomic order, however, beside surface reconstructions, surface segregations and interfacial quality, plays a vital role for the half-metallic behaviour of Heusler alloys [Sin04]. Generally, the growth rate and the growth temperature have a significant influence on the growth mode (see section 2.1), thus effecting the layer morphology. According to literature, a wide range of parameters with temperatures between  $200\text{ }^\circ\text{C}$  and  $300\text{ }^\circ\text{C}$  and growth rates between  $0.014\text{ nm min}^{-1}$  and  $0.4\text{ nm min}^{-1}$  results in long range epitaxial ordering of  $\text{Fe}_3\text{Si}$  [Her03, Ion05a, Jen05, Jen07]. Regarding interatomic ordering, however, the results are partly controversial. While in [Jen05] even at stoichiometry the order parameter  $\beta$ , which describes Si atoms taking on Fe(A,C) lattice sites and vice versa, is determined as 0.3, CTR analyses of XRD measurements performed in [Kag08] find the  $\text{Fe}_3\text{Si}$  layers to be fully ordered except in the topmost two monolayers. Also, DCXRD measurements in [Her03] indicate a high interface quality compared to Fe/GaAs(001) while the Mössbauer spectroscopy in [Kru09] shows a perturbed growth due to the interdiffusion of substrate and adsorbate atoms at the interface. However, the latter study finds that despite their determined interfacial disorder the calculated spin polarization at the Fermi energy is not significantly reduced as it decreases from the above-mentioned 43% to 36.8%.

Compared to Fe, Co and  $\text{Fe}_x\text{Co}_{1-x}$  on GaAs(001) where the growth temperatures need to be kept low in order to avoid the formation of interfacial compounds [Sch01, Nat01, Dum02] the optimum growth temperatures of  $\text{Fe}_3\text{Si}$  are considerably higher as mentioned above. Moreover, within the detection limit of DCXRD measurements  $\text{Fe}_3\text{Si}/\text{GaAs}$  is thermally stable up to approximately 425 °C [Her05] which makes it suitable for post growth treatment. At the same time, spin injection efficiencies similar to those for Fe/GaAs and MnAs/GaAs have been demonstrated using spin LED structures. Taking the spin relaxation time in the GaAs semiconductor into account an effective spin injection efficiency of 18 % could be observed [Kaw04].

Up to now, microscopic information of  $\text{Fe}_3\text{Si}$  layers on GaAs(001) in real space is very limited. In fact, the only microscopic image appears in [Jen07] in the form of an AFM micrograph where terraces with dendritically shaped edges can be recognized. Lorentzian fits of XRD rocking scans determine the average widths of these lateral features to be 55 nm and 3 nm, respectively. It is furthermore reported in [Her05] that beside the structural degradations observed by DCXRD rocking curves after rapid thermal annealing (RTA) also rectangular-shaped holes appear in AFM scans.

In contrast to that a wealth of information could be extracted from reciprocal space methods. A very thorough investigation based on CTR analyses of XRD measurements reveals the atomic structure of the  $\text{Fe}_3\text{Si}$  layers at the interface and the surface by considering several high-symmetry variants [Kag08]. It is found that two types of atomic ordering occur which most likely depends on the amount of As residues on the GaAs substrates. In one case, a mixed layer, i. e. a Fe-Si layer, is located on top of the GaAs surface where the Si sublattice atoms substitute the positions of the Ga atoms. In the second case, a Fe-Fe layer is located on top of the GaAs surface and the Si atoms take on the sites of the As atoms. A relaxation of 0.022 nm towards the GaAs substrate is observed in both cases. Also, regardless of the interface structure, the surface of the  $\text{Fe}_3\text{Si}$  film is found to be mixed terminated [Kag08]. Another study allows conclusions in terms of the growth mode of  $\text{Fe}_3\text{Si}/\text{GaAs}(001)$  as observed by XRD measurements during growth [Kag09]. These reveal the transitional appearance of 3D islands which above thicknesses of 7 monolayers changes into a quasi layerwise growth. As this is also one of the starting points of the investigations in this thesis, the origins of this growth behaviour will be discussed in greater detail within the framework of section 2.1 ('Thin film growth').

Several studies consider the magnetic properties of  $\text{Fe}_3\text{Si}/\text{GaAs}$  as these are also of fundamental interest for spintronic applications. In general, the magnetic anisotropy of  $\text{Fe}_3\text{Si}/\text{GaAs}(001)$  is a superposition of the magnetocrystalline anisotropy with easy axes along  $\langle 001 \rangle$  and a uniaxial magnetic anisotropy (UMA) where the latter was found to be smaller by about two orders of magnitude ( $K_1 = (3.1 \pm 0.6) \cdot 10^3 \text{ J m}^{-3}$  compared to  $K_u = (46 \pm 9) \text{ J m}^{-3}$  for 21 nm  $\text{Fe}_3\text{Si}/\text{GaAs}(001)$  at stoichiometry with  $T_G = 300 \text{ °C}$  [Ion05b]). The uniaxial anisotropy is small in comparison with Fe/GaAs where it is ascribed to the Fe-As or Fe-Ga bonding structure in which the dangling bonds of the topmost

layer only have a twofold symmetry. For stoichiometric  $\text{Fe}_3\text{Si}$  it is believed that the highly ordered structure of the Si atoms changes the bonding structure in a way that the twofold symmetry is suppressed and therefore the UMA is reduced [Len05]. The sign of the UMA or in other words its orientation is governed by the growth temperature and the layer thickness where higher growth temperatures and higher thicknesses favour the  $[\bar{1}10]$  direction [Her08]. Throughout the whole  $\text{D0}_3$  phase of  $\text{Fe}_3\text{Si}$  the coercive fields are found to be rather small ranging from 0.1 mT [Len05] to 0.75 mT [Ion05a]. Apart from the angular dependent MOKE measurements performed in [Ion05b] the coercive field is not known to exhibit any anisotropy. The onset of ferromagnetism for low temperatures ( $\approx 100$  K) is observed at layer thicknesses of about 3 monolayers while room temperature ferromagnetism sets in at a coverage of about 6 monolayers [Her08].

Up to here, the hybrid structure  $\text{Fe}_3\text{Si}/\text{GaAs}(001)$  was considered. However, when reviewing literature about  $\text{Fe}_3\text{Si}/\text{GaAs}(110)$  it appears that up to now no experimental work has been done so far. Information about this system, which is appealing due to its unreconstructed, non-polar surface in comparison to the manifold reconstructions of  $\text{GaAs}(001)$ , is restricted to the results of DFT calculations [Her08a]. Although the considered model is an  $\text{GaAs}/\text{Fe}_3\text{Si}/\text{GaAs}$  multilayer system in order to factor out the influence of the surface on the structure and the magnetic moments, the calculations permit the determination of the interfacial atomic structure while taking into account relaxation and interdiffusion effects. In contrast to  $\text{Fe}_3\text{Si}/\text{GaAs}(001)$  where the zincblende structure of  $\text{GaAs}$  is sustained by sublattices of the  $\text{Fe}_3\text{Si}$   $\text{D0}_3$  structure with only a slight relaxation along the surface normal the energetic minimum for the  $\text{Fe}_3\text{Si}$  species on  $\text{GaAs}(110)$  is assumed at interstitial positions. Slight lateral relaxational shifts occur along the  $[001]$  direction for As and along the  $[\bar{1}10]$  direction for Ga, Fe(B) and Si. Relaxations along the surface normal result in a reduction of the rippling observed for the free  $\text{GaAs}(110)$  surface from  $27^\circ$  [Mas82] down to  $2^\circ$ . Furthermore, the formation of the antiferromagnetic compound  $\text{Fe}_2\text{As}$  at the interface is predicted when heating the hybrid structure above  $320^\circ\text{C}$ . This has also been observed for  $\text{Fe}_3\text{Si}/\text{GaAs}(001)$  albeit only above  $500^\circ\text{C}$  [Her05]. The results from calculations in [Her08a] describe an augmented magnetic moment for a thickness of 1 monolayer ( $1.65 \mu_B$  per atom) which, under the consideration of relaxation effects, is still above the bulk value of  $1.175 \mu_B$  per atom at a thickness of 3 monolayers ( $1.35 \mu_B$  per atom). It is assumed that the bulk magnetic moment will be approached for higher layer thicknesses.

## 1.2 Outline and structure

Due to the lack of microscopic data the primary objective of the present thesis is to provide real space data of  $\text{Fe}_3\text{Si}/\text{GaAs}$  down to the atomic scale and to use this information to determine correlations between structural and magnetic properties. The first step towards this aim is the modification of an existing experimental setup to suit the requirements for

the fabrication and characterization of  $\text{Fe}_3\text{Si}/\text{GaAs}$  samples.

Considering that a large range of parameters for the epitaxial growth of  $\text{Fe}_3\text{Si}/\text{GaAs}(001)$  can be found in the literature as mentioned in the previous section, a series of experiments should be dedicated to determine the growth parameters that lead to an optimized layer morphology and surface atomic structure under the observation in real space by means of scanning tunnelling microscopy.

Due to the fact that one aim is to obtain data about the surface atomic structure in real space, this information should be used to get more insight on the electronic structure but also to possibly assign surface defects which have been reported based on the analysis of XRD measurements [Kag08].

Apart from determining correlations with the structural properties the magnetic measurements should furthermore be used to answer open questions like the thickness dependence of the magnetic moments especially towards lower coverage or to study the different contributions of the magnetic anisotropies.

Above that, the system  $\text{Fe}_3\text{Si}/\text{GaAs}$  should be studied for adsorbate layer thicknesses below which ferromagnetism sets in and below which the growth proceeds quasi layerwise (see section 2.1.2). While it can be presumed that the layer morphology is determined by the underlying Volmer-Weber growth mode it could also be interesting to study the magnetic behaviour in this thickness regime.

Analogously, the system  $\text{Fe}_3\text{Si}/\text{GaAs}(110)$ , on which up to now no experimental work has been done, shall be characterized.

Following the introduction which motivates the ongoing research and summarizes the status quo of literature of the FM/SC system  $\text{Fe}_3\text{Si}/\text{GaAs}$ , the theoretical aspects relevant to this work are considered in chapter 2. This includes energetic and kinetic considerations of thin film growth as well as the theory of magnetism of thin films. The experimental aspects are split into two chapters where chapter 3 provides the physical background information about the employed methods and chapter 4 describes the actual setups and the modifications that were done within the scope of this thesis. Chapter 5 features a study dedicated to the optimization of the layer morphology of  $\text{Fe}_3\text{Si}/\text{GaAs}(001)$  depending on the growth parameters. It also includes an extensive study of the structural and magnetic properties and their correlations for  $\text{Fe}_3\text{Si}/\text{GaAs}(001)$ . A first experimental study of  $\text{Fe}_3\text{Si}/\text{GaAs}(110)$  is presented in chapter 6. Finally, chapter 7 concludes this thesis with a summary and an outlook on future projects.



## Chapter 2

# Theoretical aspects

The crystallographic growth of thin films and their magnetic properties constitute the major part of this work. Therefore the theoretical fundamentals of thin film growth and the magnetism of thin films will be the subjects of the following two sections. The first section is meant to give an overview of different growth modes according to energetic and kinetic considerations that determine the surface morphology starting from the nucleation and reaching up to higher layer thicknesses. Especially the theoretical background of the growth mode of Fe<sub>3</sub>Si/GaAs shall be discussed on the basis of XRD analyses and kinetic Monte Carlo simulations as shown in [Kag09]. The second section provides fundamentals on the magnetic behaviour of thin films relevant to this work.

### 2.1 Thin film growth

#### 2.1.1 Energetic considerations

The film growth considered here is assumed to be epitaxial meaning that the deposited layer exhibits a crystallographic ordering that is adapted to the crystalline structure of the substrate. This can be achieved by different deposition methods of which the most prominent ones are MBE, CVD and sputter deposition. The former was employed for the film growth in this work using Knudsen cell evaporators for the deposition of Fe, Ag and Au and an electron beam evaporator for the deposition of Si. In all cases the adhesion between the substrate and the adsorbate is dominated by chemisorption.

Moving close to thermodynamic equilibrium, i. e. if the deposition rate is not too high and if the adatoms possess sufficient mobility at the surface, there are three principle growth modes that were first summarized by Bauer [Bau58, Bau82]. Neglecting edge energies and chemical reactions between the adsorbate and the substrate, the growth mode is determined by the change of the surface energy

$$\Delta\sigma = \sigma_{\text{ad}} + \sigma_{\text{int}} - \sigma_{\text{sub}} \quad (2.1)$$

in the growth process where  $\sigma_{\text{ad}}$ ,  $\sigma_{\text{int}}$  and  $\sigma_{\text{sub}}$  denote the surface energies of the adsorbate, the interface and the substrate, respectively.  $\Delta\sigma < 0$  corresponds to the situation in which the binding between the adatoms and the substrate is more favourable than a partially exposed substrate. This leads to a wetting of the substrate surface and a layerwise growth also known as the Frank-van der Merwe growth mode which is illustrated on the left hand side of figure 2.1. The case  $\Delta\sigma > 0$  causes the adatoms to form islands so as to minimize the costly formation of adsorbate surfaces. This is referred to as the Volmer-Weber growth mode which is shown in the centre of figure 2.1. Another growth mode that can be seen on the right hand side of figure 2.1 and which is known as the Stranski-Krastanov growth mode describes an initially layerwise growth mode followed by an islandwise growth. This corresponds to a change of sign of  $\Delta\sigma$  which can be ascribed to an increase of  $\sigma_{\text{int}}$ . This is often a result of a mismatch between the lattice constants of the adsorbate and the substrate which results in increasing strain with increasing layer thickness. The formation of islands can then be seen as a relaxation process. The lattice mismatch is defined by

$$\eta = \frac{a_{\text{a}} - a_{\text{s}}}{a_{\text{s}}}. \quad (2.2)$$

Here,  $a_{\text{a}}$  is the lattice constant of the adsorbate and  $a_{\text{s}}$  is the lattice constant of the substrate. In the case of Fe<sub>3</sub>Si/GaAs  $\eta$  is as small as 0.2% for bulk Fe<sub>3</sub>Si at stoichiometry [Kru09] and is thereby negligible.

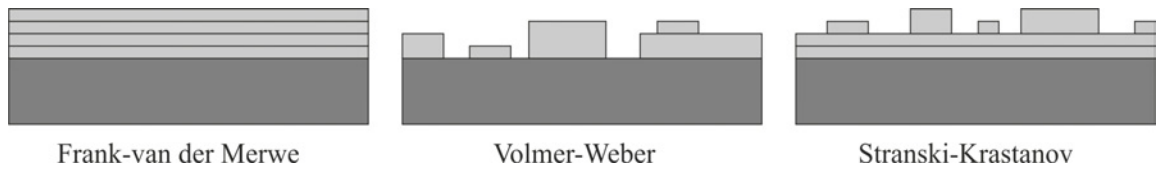


Figure 2.1: Illustrations of the different crystallographic growth modes based on surface energetic considerations. The Frank-van der Merwe growth mode describes a layerwise growth behaviour. The Volmer-Weber growth mode corresponds to an islandwise growth. In the case of the Stranski-Krastanov growth mode there is a transition from an initially layerwise growth to an islandwise growth behaviour at higher coverage.

### 2.1.2 Growth kinetics

Oftentimes, depending mainly on the deposition rate and on the growth temperature, the growth proceeds far from thermodynamic equilibrium. This can result in effects like a pseudo Frank-van der Merwe or pseudo Stranski-Krastanov growth mode where the underlying mechanism is actually the Volmer-Weber growth mode. In such a case the nucleation behaviour and the resulting layer morphology is best described by a kinetic approach.

The dynamics of clusters and monomers is determined by rate equations that were formulated by Venables [Ven73, Ven84, Ven94]. It is assumed that the monomers can diffuse

freely across the substrate surface and across clusters while clusters are fixed because the mobility decreases exponentially with the activation energy which is much higher for clusters than for monomers. It is furthermore assumed that the deposition rate  $R$  is constant and, like in the energetic consideration, that there are no chemical reactions between the adsorbate and the substrate. This yields the following set of coupled differential equations:

$$\frac{dn_1}{dt} = R - A - 2U_1 - \sum_{j=2}^{\infty} U_j \quad (2.3)$$

$$\frac{dn_j}{dt} = U_{j-1} - U_j \quad (j \geq 2). \quad (2.4)$$

In the above equations  $n_1$  and  $n_j$  denote the surface densities of monomers and clusters, respectively, where the latter consist of  $j$  atoms. The term  $A$  takes into account the loss of atoms due to re-evaporation also known as desorption.  $U_j$  are the rates for monomers and clusters for capturing an additional atom.

Further simplifications can be made considering that, depending on their size, certain clusters are stable while others are unstable. Due to the greater ratio between the area and the perimeter there is a higher chance for large clusters to capture new atoms than to lose them by edge desorption processes. For the same reason clusters below a critical size  $i$  tend to disperse again. This process can be understood as a form of Ostwald ripening that was first used to describe the growth of large colloids in a vapour at the expense of small colloids. The equations 2.3 and 2.4 can then be rewritten as follows:

$$\frac{dn_1}{dt} = R - A - \frac{d(n_x w_x)}{dt} \quad (2.5)$$

$$\frac{dn_j}{dt} = 0 \quad (2 \leq j \leq i) \quad (2.6)$$

$$\frac{dn_x}{dt} = U_i - U_g - U_m. \quad (2.7)$$

Equation 2.5 describes the growth of the density of monomers on the surface. It increases with the deposition rate  $R$  and is diminished by the desorption rate  $A$  as well as by another term which describes the capturing of monomers by stable clusters. Here,  $n_x$  is the surface density of all stable clusters while  $w_x$  is their average size. Note that in total no monomers are captured by unstable clusters as these disintegrate with the same rate as they are formed which is also expressed by equation 2.6. The growth of the density of stable clusters  $n_x$  is given by equation 2.7.  $U_i$  describes the rate by which clusters with the critical size  $i$  capture a monomer. It is given by

$$U_i = \sigma_i D n_i n_1 \quad (2.8)$$

where  $\sigma_i$  denotes the capture cross-section for critical clusters which is typically of the order of 2 to 4 [Res01] and  $D$  denotes the diffusion constant. The terms  $U_g$  and  $U_m$  describe the effects of coalescence due to the growth of stable clusters and due to their mobility. While

the coalescence caused by cluster mobility is negligible as mentioned earlier, the coalescence due to growth is given by

$$U_g = 2n_x \frac{dZ}{dt}. \quad (2.9)$$

Here,  $Z$  is the percentage of surface covered by clusters.

Further expressions can be found which establish connections between the critical cluster density and the density of monomers and for the growth of stable clusters which depends on the diffusion and on the deposition rate. The former is known as the Walton relation [Wal62]:

$$\frac{n_i}{N_0} = \left(\frac{n_1}{N_0}\right)^i \sum_m C_i(m) \exp\left(\frac{E_i(m)}{k_B T}\right). \quad (2.10)$$

The  $C_i(m)$  are statistical weights for the different possible shapes of critical clusters consisting of  $i$  atoms and the  $E_i(m)$  are the corresponding binding energies. The second expression is given by

$$\frac{d(n_x w_x)}{dt} = (i+1)U_i + \sigma_x D n_1 n_x + RZ \quad (2.11)$$

where  $\sigma_x$  is the capture cross-section for stable clusters.

From the above equations it becomes obvious that the initial growth behaviour strongly depends on diffusion rates, binding energies and the deposition rates. Figure 2.2 illustrates the elementary steps that can typically occur during epitaxial growth. Atoms that reach the sample can adsorb on the bare substrate (a) or on an already existing cluster (b). After a certain time called the adsorption time

$$\tau_a = \nu_a^{-1} \exp\left(\frac{E_a}{k_B T}\right) \quad (2.12)$$

where  $\nu_a$  is a characteristic frequency of surface vibrations and  $E_a$  is the binding energy of a monomer the adatom might desorb again (c). (d) and (e) mark basic diffusion steps across the substrate or on top of a cluster. The diffusion time is determined by

$$\tau_d = \nu_d^{-1} \exp\left(\frac{E_d}{k_B T}\right). \quad (2.13)$$

$\nu_d$  is the effective frequency of surface vibrations which is typically slightly larger than  $\nu_a$  and  $E_d$  is the diffusion barrier. Atoms may also attach to (f) and detach from (g) cluster edges or diffuse along edges (h) thus changing the shape of the clusters. The step (i) shows the merging of two monomers, the chance for which increases with increasing mobile species deposited on the substrate. Small clusters below the critical size  $i$  tend to decay again as shown in (j). However, according to equation 2.6 the overall amount of unstable clusters with  $2 \leq j \leq i$  remains constant because their formation rate corresponds to their decay rate. Other types of elementary steps that can substantially influence the growth behaviour are upward and downward jumps from one terrace to the next (k). These are, however, limited by additional diffusion barriers which in the case of downward jumps is known as

the Ehrlich-Schwoebel barrier [Sch66]. In this case the diffusion barrier  $E_d$  in equation 2.13 is increased by an additional term  $\Delta E_{ES}$ .

Examples of the growth modes and elementary growth steps as studied by in situ STM are reviewed in [Mue04].

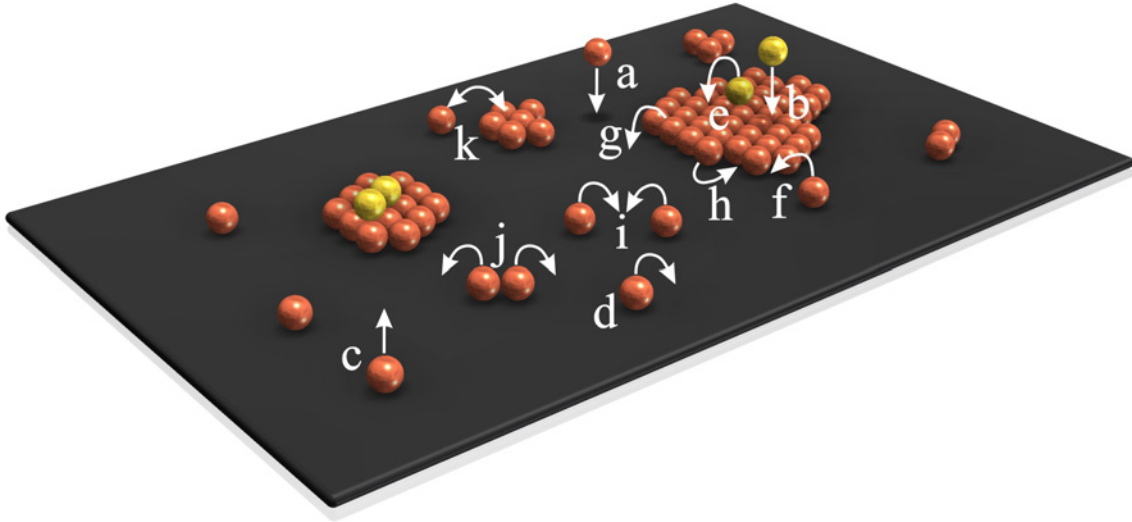


Figure 2.2: Cluster formation and elementary steps during epitaxial growth. Some of the clusters may already be stable while others may decompose again. The red- and yellow-coloured atoms depict atoms in the first and in the second layer, respectively. (a) adsorption on the bare substrate (b) adsorption on an already existing cluster (c) desorption (d) diffusion on the substrate (e) diffusion on a cluster (f) edge adsorption (g) edge desorption (h) edge diffusion (i) nucleation of two monomers (j) decay of an unstable dimer or cluster (k) upward jump over a step edge

The growth of  $\text{Fe}_3\text{Si}$  on GaAs is one of the key topics of this work. Although there is no real space data on the surface morphology apart from a large-scale AFM scan with low resolution [Jen07] some predictions regarding the growth behaviour can be deduced from XRD measurements, ab initio calculations and Monte Carlo simulations as shown in [Kag09]. As mentioned earlier on the lattice mismatch of  $\text{Fe}_3\text{Si}/\text{GaAs}$  is negligible so that the growth behaviour when moving close to thermodynamic equilibrium should be surface energy driven. From the knowledge of the interface atomic arrangement [Kag08] ab initio calculations yield a positive overall surface energy of  $\Delta\sigma \approx 10 \text{ eV nm}^{-2}$  with only a weak thickness dependence which corresponds to a Volmer-Weber growth mode. However, the analysis of the x-ray intensity oscillations shows that the appearance of 3D islands is only transitional. Starting at a thickness of about 7 ML the layer thickness amounts to the material deposited on the sample. The quality of the intensity oscillations that follow thereupon depend on the deposition rate which yields optimum results between 1 ML/120s and 1 ML/1200s. As the growth behaviour cannot be explained by surface energetic considerations, growth kinetics seem to play an important role. Indeed, the

Monte Carlo simulations performed in [Kag09] can emulate this growth behaviour in the simple bondcounting model if the diffusion barrier is modified. The diffusion barrier used in equation 2.13 has two contributions:

$$E_d = E_S + nE_b. \quad (2.14)$$

$E_S$  is the surface diffusion,  $E_b$  is the bond energy and  $n$  is the number of nearest neighbours. It is now assumed that  $E_S$  is reduced for the first deposited layer and effectively replaced by  $E_S - \Delta E_S$  which would result in a higher mobility of the adatoms leading to an increased nucleation and this island formation. Using  $E_S = 1.1$  eV and  $\Delta E_S = 0.11$  eV the Monte Carlo simulations yields results that are in agreement with the observed x-ray intensity oscillations. Concluding, the predicted growth of Fe<sub>3</sub>Si/GaAs can be regarded as a pseudo Frank-van der Merwe growth.

## 2.2 Magnetism of thin films

Apart from the structural properties of the thin layers considered in this work their magnetic properties are of paramount interest both from a fundamental point of view as well as regarding possible spintronic applications. The latter rely on asymmetrical band structures for different spin states as they are present in the case of ferromagnetic materials.

This section starts off with some basic theoretical considerations of magnetism and then describes the phenomena necessary in later discussions regarding the experimental findings.

### 2.2.1 Ferromagnetism

#### The origin of ferromagnetism

Ferromagnetism describes the phenomenon of the uniform orientation of the elementary magnets either entirely or in certain regions of a sample called domains as it is present in certain materials. In contrast to other forms of magnetism external fields do not induce the magnetic moment of the elementary magnets as these are permanent. Solely the orientation and the size of the magnetic domains is influenced in a more or less complicated fashion depending on the system. In particular the spontaneous magnetization even persists in the absence of external fields.

While the macroscopic effects of permanent magnets have already been known in ancient Greece and first applications as a compass needle date back to the eleventh century in China the exact physical origin of ferromagnetism could only be investigated and understood after the introduction of quantum mechanics, i. e. during approximately the last 100 years.

Neglecting quantum mechanical effects the collective ordering of spins is at first counter-intuitive considering only the interaction energy between two magnetic dipoles:

$$E_{\text{dipolar}} = \frac{\mu_0}{4\pi} \left( \frac{\vec{\mu}_1 \cdot \vec{\mu}_2}{r^3} - 3 \frac{(\vec{\mu}_1 \cdot \vec{r})(\vec{\mu}_2 \cdot \vec{r})}{r^5} \right). \quad (2.15)$$

If the two magnetic dipoles  $\vec{\mu}_1$  and  $\vec{\mu}_2$  are side by side the second term equals zero and the energy is minimized if the dipoles are oriented antiparallel. In other words, there must be a stronger driving force responsible for ferromagnetism. As mentioned beforehand the origin is quantum mechanical. To illustrate this, the total wave function  $\Psi(x_1, x_2)$  of two electrons<sup>1</sup> shall be considered where the coordinates  $x_i$  contain information about both space and spin state. Due to the fermionic nature of the electrons the total wave function needs to be antisymmetric. As a result the total wave function and hence the probability density  $\rho = \Psi\Psi^*$  amounts to zero if the coordinates including the spin are identical. It can furthermore be shown that the average distance between two electrons with parallel spin is larger than in the case of antiparallel spin which causes a decrease of the electrostatic energy. Hence, the origin of ferromagnetism can be described by the reduction of the Coulomb part of the potential energy triggered by quantum mechanical principles. However, apparently not every material is ferromagnetic. The exact conditions are determined by more elaborate theoretical calculations as they were first performed according to the Heitler-London model for the  $H_2$  molecule where the exchange integral appears for the first time as described in [Kös56] for example. This exchange interaction is due to the overlapping of wave functions of indistinguishable particles and in principle determines the strength of ferromagnetic coupling. It is given by

$$J = \int \psi_a^*(\vec{r}_1)\psi_b^*(\vec{r}_2)\hat{H}\psi_a(\vec{r}_2)\psi_b(\vec{r}_1)d\vec{r}_1d\vec{r}_2 \quad (2.16)$$

where  $\psi_a$  and  $\psi_b$  denote the different states,  $\vec{r}_1$  and  $\vec{r}_2$  denote the coordinates of the two electrons and  $\hat{H}$  denotes the effective Hamiltonian [Blu01]. From his calculations dating back to 1928 Heisenberg concluded that among the pure elements only Fe, Co and Ni could be ferromagnetic at room temperature [Hei28]. It was later discovered that also gadolinium ( $T_C = 240$  K), terbium ( $T_C = 221$  K) and dysprosium ( $T_C = 85$  K) are ferromagnetic even if only at low temperatures [Ber92].

A simplified model of ferromagnetism was already proposed in 1907 by Weiss [Wei07] which makes a mean field approximation but nevertheless yields some results that are characteristic for ferromagnets. Considering a ferromagnet in an applied field  $\vec{B}$  its Hamiltonian is

$$\hat{H} = - \sum_{i,j} J_{ij} \vec{S}_i \cdot \vec{S}_j + g\mu_B \sum_j \vec{S}_j \cdot \vec{B} \quad (2.17)$$

neglecting anisotropies and dipolar interactions. In the above equation  $g$  denotes the Landé factor which in good approximation equals to 2 for the spin angular momentum and  $\mu_B$  denotes the Bohr magneton which is defined by  $\mu_B = e\hbar/2m_e$ . The first term corresponds to the exchange energy while the second term considers the Zeeman energy. In the case

---

<sup>1</sup>This consideration is legitimate as it was already shown in the Einstein-de Haas effect that it is mostly the magnetic moments of the electrons associated with their spins that are responsible for the magnetic moment of ferromagnetic materials [Mes01].

of ferromagnetic alignment the  $J_{ij}$  are positive. Now in the model by Weiss the exchange interaction is being replaced by an effective molecular field

$$\vec{B}_{\text{mf}} = -\frac{2}{g\mu_{\text{B}}} \sum_j J_{ij} \vec{S}_j \quad (2.18)$$

which is proportional to the magnetization  $\vec{M}$  and can therefore also be written as

$$\vec{B}_{\text{mf}} = \lambda \vec{M} \quad (2.19)$$

where  $\lambda$  is positive in the case of a ferromagnet. The drawback of this model is that  $\vec{B}_{\text{mf}}$  is assumed to be homogeneous across all  $\vec{S}_i$ . Furthermore, the alignment of the magnetic moments is thought to be caused by the mean field which in its own right is a result of this alignment. Hence, the situation becomes comparable to the 'chicken-and-egg' scenario [Blu01].

Using equations 2.18 and 2.19 the Hamiltonian from equation 2.17 can be written as

$$\hat{H} = g\mu_{\text{B}} \sum_j \vec{S}_j \cdot (\vec{B} + \lambda \vec{M}). \quad (2.20)$$

In order to find a solution, the following equations need to be solved simultaneously:

$$\frac{M}{M_{\text{s}}} = B_J(y) \quad (2.21)$$

$$y = \frac{gJ\mu_{\text{B}}J(B + \lambda M)}{k_{\text{B}}T}. \quad (2.22)$$

Here,  $B_J$  denotes the Brillouin function while the index  $J$  is the total angular momentum given by  $\vec{J} = \vec{L} + \vec{S}$  which generalizes the solution. As shown in [Blu01] the equations 2.21 and 2.22 can be solved graphically for the case of  $B = 0$ . This yields the critical temperature  $T_{\text{C}}$ , also known as the Curie temperature, which separates the states of random orientations of the magnetic moments from the state of spontaneous magnetization even in the absence of an external field:

$$T_{\text{C}} = \frac{gJ\mu_{\text{B}}(J+1)\lambda M_{\text{s}}}{3k_{\text{B}}}. \quad (2.23)$$

The Weiss model furthermore yields the temperature dependence of the magnetization as shown in figure 2.3. The magnetization drops to zero for  $T > T_{\text{C}}$  but is continuous at  $T_{\text{C}}$  while its derivative is discontinuous. Using the relation

$$M = -\left(\frac{\partial F}{\partial B}\right)_T \quad (2.24)$$

and the definition that the order of a phase transition is the order of the lowest differential of the free energy which exhibits a discontinuity at the phase transition it becomes apparent that the transition from the non-magnetic to the ferromagnetic phase is of the second order. For completeness it should be mentioned that the origin of ferromagnetism in materials such

as iron, cobalt and nickel cannot in principle be described by the model of localized spins but is rather based on the spontaneous splitting of the spin-up and spin-down electron bands known as band ferromagnetism. Then the magnetic moment per atom can also take on real valued multiples of  $\mu_B$ . This spontaneous splitting of the spin-up and spin-down electron bands can be understood by considering that the change in potential energy of the electrons doing a spin flip near the Fermi energy can be greater than the increase in kinetic energy. This is summarized by the Stoner criterion:

$$U_{\text{eff}}N(E_F) > 1. \quad (2.25)$$

$U_{\text{eff}}$  is an effective exchange energy and  $N(E_F)$  is the density of states per spin subband at the Fermi energy. In the case of ferromagnetism, the above inequality is satisfied.

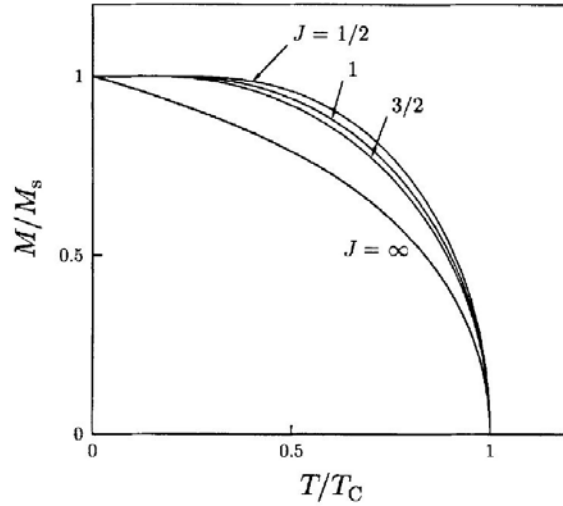


Figure 2.3: The magnetization as a function of the temperature for different values of the total angular momentum  $J$  [Blu01]. The discontinuity of the derivative of this function at  $T_C$  also indicates that the transition from the non-magnetic to the ferromagnetic phase is a second-order phase transition.

### The magnetization process

The magnetization of a ferromagnet in the presence of an external magnetic field  $\vec{B}_0$  can in general be described by

$$\vec{M} = \chi_m \frac{\vec{B}_0}{\mu_0}. \quad (2.26)$$

The magnetic susceptibility  $\chi_m$  is a both a function of the external field as well as the history of the ferromagnet. It can reach values of up to 14,000 for the initial magnetization curve and 280,000 as the overall maximum in the case of polycrystalline iron [Kne62].

Microscopically, the magnetization is defined by the magnetic moment as a vector quantity per volume:

$$\vec{M} = \sum_i \frac{\vec{\mu}_i}{V}. \quad (2.27)$$

One of the most significant methods to characterize the magnetization process of a ferromagnetic sample is to record hysteresis loops where an external magnetic field is applied in a certain direction and swept in a way that the magnetization reaches its saturation value  $|\vec{M}_s|$  in both directions. This can be done on different time scales which yields quasi-static hysteresis loops if the external field is swept slowly with respect to the remagnetization processes and dynamic hysteresis loops in the case of fast sweeps. While the latter can be used to determine the dynamics of domain wall motions with methods such as femtosecond lasers [Eim09] the measurements performed on samples in this work are restricted to quasi-static hysteresis loops. These, however, already yield a wealth of information such as magnetic anisotropies, the saturation magnetization and the coercive field. Their interpretation can even shed light on the mechanisms of the remagnetization process. One important quantity that can be derived from the hysteresis loops, given that the method from which they were obtained allows the determination of the absolute magnetization value, is the energy needed for the remagnetization process:

$$E_{\text{remag}} = \mu_0 \oint H dM \quad (2.28)$$

The magnetization state and hence the remagnetization process on the microscopic scale depends not only on the applied external field but also on the exchange and dipolar interactions and on the various forms of anisotropy that will be discussed in the following section. The main difference between a ferromagnet and a paramagnet is the existence of magnetic domains according to the theory of Weiss. Within each of these domains the spins are aligned parallel to each other causing the local magnetization to reach the saturation value. In contrast to paramagnets small external fields can already be sufficient to align the domains parallel to the direction of the applied field and to each other. Without dipolar interactions and dipolar stray fields and with exchange and magnetocrystalline anisotropy energies alone in the absence of an external field the magnetization would be homogeneously oriented along one of the easy axes across the entire sample. This is in reality not the case as the long range dipolar stray fields can be reduced with the formation of domains. The actual domain structure is then determined by the minimization of the domain wall energies in addition to the energies mentioned beforehand. The domain walls constitute the transition of spin orientation between differently oriented magnetic domains. If the spins rotate parallel to the plane of the wall it is called a Bloch wall. If they rotate perpendicular to the plane of the wall it is referred to as a Néel wall. The energy associated with the formation of a domain wall is determined by the exchange interaction and the magnetocrystalline anisotropy. In the case of a Bloch wall between two domains that

are aligned antiparallel to each other it can easily be shown [Blu01] that the domain wall energy per area is given by

$$\sigma = JS^2 \frac{\pi^2}{Na^2} + \frac{NKa}{2}. \quad (2.29)$$

In the above equation  $N$  denotes the number of spins in one line across the domain wall,  $S$  is the absolute value of the spin,  $a$  is the lattice constant and  $K$  represents the magnetocrystalline anisotropy. The minimization of this energy yields the domain wall width

$$\delta = \pi S \sqrt{\frac{2J}{Ka}}. \quad (2.30)$$

It becomes evident that the exchange interaction favours a wide domain wall while magnetocrystalline anisotropy constrains the domain wall.

For completeness it should be mentioned that the interplay between the interactions mentioned above also determines the magnetization reversal process in terms of the domain structure. Upon variation of the applied external field the magnetization can change by the rotation of the domains which is the preferred case for soft ferromagnets or by domain wall motion in the case of hard ferromagnets.

### Magnetic anisotropies

While anisotropy contributions were still neglected up to here they can have significant impact on the magnetization behaviour. The energy associated with the anisotropies can be determined quantitatively by considering the direction for which the remagnetization energies given by equation 2.28 become maximal and minimal and subtracting them one from the other. The corresponding directions are called the easy and the hard axis, respectively.

The exact state of the magnetization

$$\vec{M}(\vec{r}, t, \vec{H}) = |\vec{M}_s| \begin{pmatrix} \gamma_1(\vec{r}, t, \vec{H}) \\ \gamma_2(\vec{r}, t, \vec{H}) \\ \gamma_3(\vec{r}, t, \vec{H}) \end{pmatrix} \quad (2.31)$$

which is generally a function of space, time and the external field is determined by the minimization of the Helmholtz free energy

$$F = F_{\text{anisotropy}} - \mu_0 \int \vec{M}_s \cdot \vec{H} d^3r. \quad (2.32)$$

In equation 2.31 the  $\gamma_i$  denote the directional cosines. The first term on the right hand side of equation 2.32 can have various contributions due to different types of anisotropies that shall be discussed in the following while the second term accounts for the Zeeman energy.

**Magnetocrystalline anisotropy** One of the most important anisotropy contributions and especially for magnetic layers with higher thicknesses the dominant one is the magnetocrystalline anisotropy which finds its origin in the spin-orbit coupling of the electrons. Due to the fact that the lattice structure of a crystal is a highly anisotropic object and that electrons contributing to ferromagnetism are typically in the  $3d$  or  $4f$  state different spin alignments result in a change of the electrostatic energy. The energy associated with this form of anisotropy can be derived by geometrical and symmetrical considerations. In the case of cubic systems as they are considered in this work the magnetocrystalline anisotropy takes on the form

$$F_{mc} = K_0 + K_1 (\gamma_1^2 \gamma_2^2 + \gamma_2^2 \gamma_3^2 + \gamma_1^2 \gamma_3^2) + K_2 \gamma_1^2 \gamma_2^2 \gamma_3^2 + \dots \quad (2.33)$$

The directional cosines occur only in even powers as crystallographically equivalent directions must also be equivalent in terms of energy. Due to the relation  $\gamma_1^2 + \gamma_2^2 + \gamma_3^2 = 1$  which is subsumed as  $K_0$  the first angular dependency appears for  $\gamma_i^2 \gamma_j^2$ .  $K_i$  denote the magnetocrystalline anisotropy constants for different orders where it is oftentimes sufficient to consider only up to the fourth order. It should be noted that in different publications the fourth order is sometimes denoted as  $K_1$  and sometimes as  $K_4$ .

The energy associated with the magnetocrystalline anisotropy typically lies in the range of  $10^2 \text{ J m}^{-3}$  to  $10^7 \text{ J m}^{-3}$  which corresponds to an energy of  $10^{-8} \text{ eV}$  to  $10^{-3} \text{ eV}$  per atom [Blu01]. The signs of the  $K_i$  indicate the preferred direction of the magnetization. In the case of Fe both  $K_1$  and  $K_2$  are positive which is equivalent to the fact that the  $\{100\}$  are the easy axes. Moreover, the anisotropy constants can have a strong temperature dependence.

The angular dependent contributions to the Helmholtz free energy caused by the magnetocrystalline anisotropy for the case of positive  $K_0$  and  $K_1$  can be seen in figure 2.4. The cross sectional views illustrate the in plane anisotropies for the  $(001)$  and the  $(\bar{1}10)$  surfaces which are relevant to the systems that were analyzed in the scope of this work.

**Magnetoelastic anisotropy** Another form of anisotropy that can be assigned to the lattice structure of a crystal and the effect of spin-orbit coupling is the magnetoelastic anisotropy. It describes how the preferred direction of magnetization can be altered due to mechanical stress. This can be understood by considering that tensile or compressive stress can change the charge density distribution of the electrons. The electron spins will then also be realigned by spin-orbit coupling.

The magnetoelastic anisotropy can phenomenologically be described by

$$F_\sigma = -\frac{3}{2} \lambda_{100} \sum_i \sigma_{ii} \gamma_i^2 - \frac{3}{2} \lambda_{111} \sum_{i \neq j} \sigma_{ij} \gamma_i \gamma_j \quad (2.34)$$

where  $\lambda_{100}$  and  $\lambda_{111}$  are relative changes in length with respect to the  $[100]$  and  $[111]$  directions which are typically in the order of  $10^{-8}$  to  $10^{-4}$ .  $\sigma_{ij}$  are elements of the stress

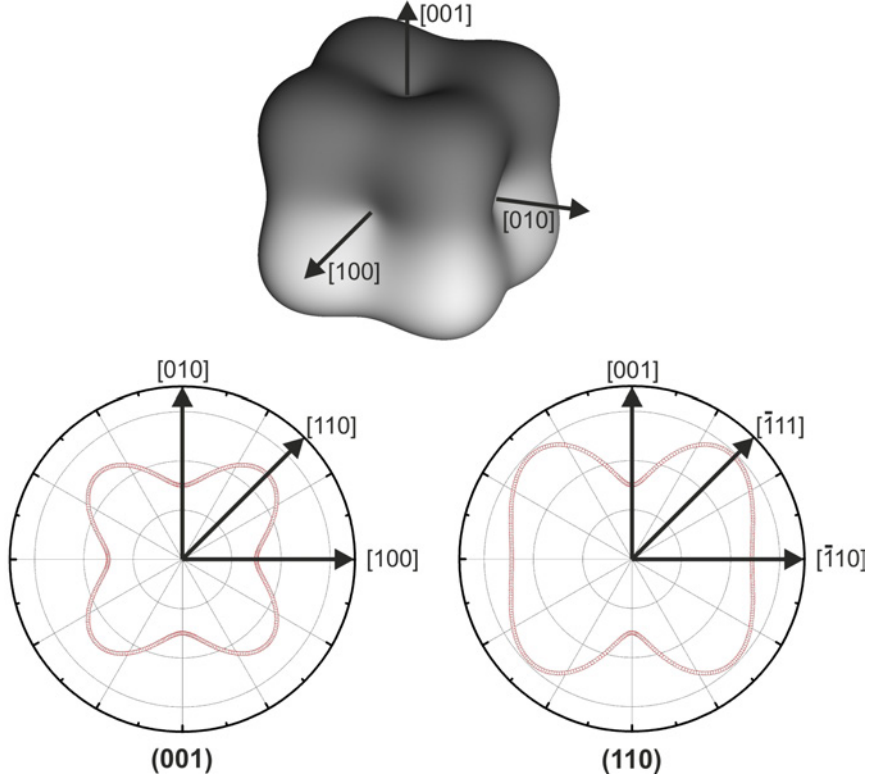


Figure 2.4: Illustration of the magnetocrystalline anisotropy energy for the case of cubic symmetry. The constants chosen for this plot are  $K_0 = 0.3$ ,  $K_1 = 0.75$  and  $K_2 = 1$  in arbitrary units. The polar plots are cross-sectional views of the (001) and the (110) planes respectively.

tensor and  $\gamma_i$  are again the directional cosines of the main crystallographic axes [Ber92, Kne62].

The inverse effect also exists and is known as magnetostriction and comes about when cause and effect are reversed. In other words an applied field can cause a deformation of the crystal when this deformation will save more anisotropic energy than it will cost elastic energy [Blu01].

**Shape anisotropy** This anisotropy is governed by the interplay of the demagnetization field or the stray field of a ferromagnet and the magnetization therein and depends strongly on the shape. Due to  $\nabla \cdot \vec{B} = 0$  and  $\vec{B} = \mu_0(\vec{H} + \vec{M})$  the stray field and the demagnetization field are connected by  $\nabla \cdot \vec{H} = -\nabla \cdot \vec{M}$  where the right part of the equation can be understood as the density of magnetic charges at the sample surface. In general, the demagnetization energy is given by

$$E_d = \frac{\mu_0}{2} M_s^2 \int_V \vec{m}(\vec{r}) N \vec{m}(\vec{r}) d^3r \quad (2.35)$$

where  $\vec{m}(\vec{r})$  are the unit vectors parallel to the magnetization and  $N$  is the so-called demagnetization tensor which depends on the sample geometry and takes on the form

$$N = \begin{pmatrix} 0 & 0 & 0 \\ 0 & 0 & 0 \\ 0 & 0 & 1 \end{pmatrix} \quad (2.36)$$

for thin films [Fra05]. In this case the expression for the shape anisotropy can be simplified to

$$F_{Shape} = \frac{\mu_0}{2} M_S^2 \cos^2 \theta. \quad (2.37)$$

$\theta$  is the angle between the film normal and the magnetization  $\vec{M}$ . From this above equation it becomes obvious that the energy is reduced if the magnetization lies within the film plane. As a rule of thumb this anisotropy becomes dominant if the thickness of the ferromagnetic layer is smaller than about ten times the Bloch wall thickness which typically corresponds to a thickness of 5 nm to 100 nm [Kne62]. In this range the magnetocrystalline anisotropy becomes negligible compared to the stray field energy needed to rotate the magnetic moments out of plane.

**Surface and interface anisotropy** Apart from the shape anisotropy also the surface and the interface anisotropy contribute a substantial amount to the overall anisotropy at small layer thicknesses. This effect can be ascribed to either missing binding partners at the surface or other types of atoms in the case of interfaces. As a result both the magnitude and the direction of the magnetization can be affected. The magnetization tends to become increased because a possible relaxation leads to an increased lattice constant which brings about an increased density of states. This in turn increases the chance of the Stoner criterion (see equation 2.25) to be satisfied. It is predicted that for example Palladium and Vanadium which are normally non-ferromagnetic metals can become ferromagnetic at a thickness of one monolayer [Blu01]. The contribution of the surface and the interface anisotropy to the free energy can be described by

$$F_{s,i} = \frac{2K_s}{t} \sin^2 \theta \quad (2.38)$$

where  $K_s$  is the surface or interface anisotropy constant,  $t$  is the layer thickness and  $\theta$  denotes the angle between the magnetization and the surface normal [Blu01]. The factor 2 arises from the fact that a layer has two faces. Contrary to the shape anisotropy which is associated with the demagnetization energy the surface and interface anisotropy acts so as to turn the magnetization out of the film plane.

### 2.2.2 Superparamagnetism

Nanoparticles consisting of a ferromagnetic material, which can for example be formed either lithographically or in a self-organized growth process, can exhibit single-domain

states in the case that they are smaller than defined by the critical radius

$$R_c = \frac{36\sqrt{AK}}{\mu_0 M_s^2}. \quad (2.39)$$

In the above equation  $M_s$  denotes the saturation magnetization while  $\sqrt{AK}$  is the surface energy density for the formation of domain walls [Pet10]. The exact value of  $R_c$  depends on the material but in general typical magnetic moments of such a particle are of the order of  $1000 \mu_B$ . If the particles are furthermore separated far enough in a non-magnetic matrix their behaviour can be similar to that of a paramagnet depending on the temperature, a state which is defined as superparamagnetism (SPM).

Theoretically, a superparamagnetic system can best be described by the Stoner-Wohlfarth model [Pet10]:

$$E = KV \sin^2 \phi - \mu_0 H M_s V \cos(\theta - \phi). \quad (2.40)$$

In the case of single-domain particles which do not have interactions among each other the exchange energy  $E_J$  and the dipolar coupling energy  $E_d$  become negligible.  $K$  is an effective anisotropy constant which results from magnetocrystalline and shape anisotropy.  $\phi$  is the angle between the anisotropy axis and the magnetic moment of the particle whose volume is  $V$  and  $\theta$  is the angle between the anisotropy axis and the applied field.

Figure 2.5 shows the energy as a function of the magnetization vector of a SPM particle for  $H = 0$  (blue curve) and  $H \neq 0$  (red curve). In the first case the function is symmetrical and takes on minima for  $\phi = 0^\circ$  and  $\phi = 180^\circ$  which are separated by an energy barrier of  $\Delta E = KV$  which is given by the anisotropy energy. In the second case, this degeneracy is lifted in the presence of an applied field where the energy takes on an absolute minimum for one direction.

The magnetization dynamics of a SPM particle is strongly governed by the temperature. The relaxation time which determines how fast the magnetization fluctuates between the two energy minima is given by

$$\tau = \tau_0 \exp\left(\frac{KV}{k_B T}\right) \quad (2.41)$$

or as described in [Pet10] in the more general case of a field-dependent energy barrier

$$\tau = \tau_0 \exp\left(\frac{\Delta E(H, \theta)}{k_B T}\right). \quad (2.42)$$

However, equation 2.41 shall be sufficient for the following considerations.  $\tau_0$  typically lies in the range of  $10^{-9}$  s [Blu01]. One can divide the magnetic behaviour of such a SPM system into two regimes. If  $KV \gg k_B T$ , the magnetization is trapped in one of the two minima and cannot switch spontaneously. As a result the system behaves like a permanent ferromagnet. If  $KV \approx k_B T$  or less, spontaneous switching can occur and the system behaves superparamagnetically. The temperature that separates these two regimes is called the blocking temperature  $T_B$ . By rewriting equation 2.41 and introducing a term

$\alpha$  which is of the order of 100 and which takes into account that the relaxation time must be somewhat larger than the measuring time the blocking temperature is defined by

$$T_B = \frac{KV}{k_B} \ln^{-1} \left( \frac{\alpha t}{\tau_0} \right). \quad (2.43)$$

It becomes obvious that the blocking temperature actually depends on the measuring time  $t$ . Typical timescales for SQUID magnetometry measurements as they were performed in the scope of this work are 10 s.

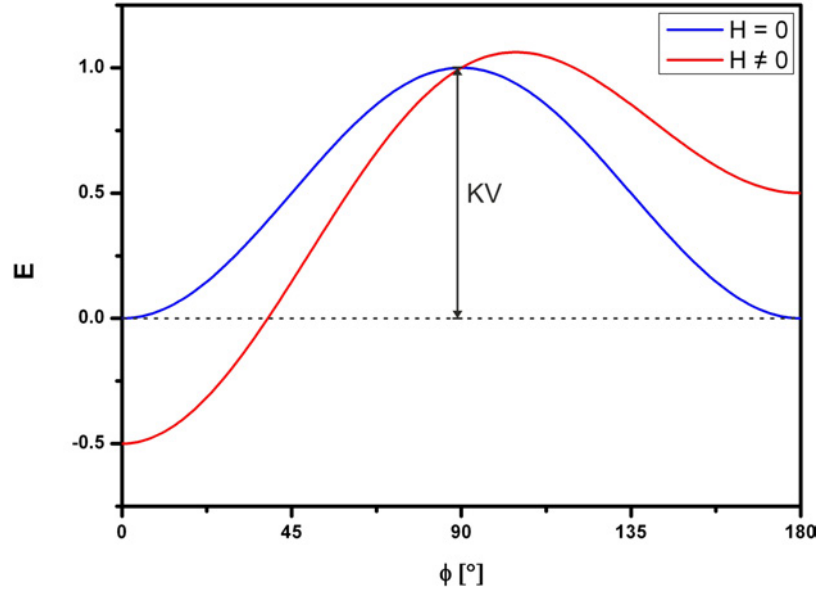


Figure 2.5: Angular dependent energy associated with the magnetization of a SPM particle. The blue curve corresponds to the symmetrical case of zero applied field where the energy barrier is given by the anisotropy energy  $KV$ . The case of an applied field for  $\theta = 0^\circ$  with a preferred direction is illustrated by the red curve.

There are two ways in order to determine whether a system is superparamagnetic by standard magnetometry measurements. One is to record hysteresis loops on different time scales where in the case of  $\tau_{M-H} \gg \tau(T)$  with the recording time  $\tau_{M-H}$  the hysteresis loop should exhibit a closed s-shape because the system does not get sufficient time for switching. If however  $\tau_{M-H} \lesssim \tau(T)$  the hysteresis loop should be open. Another way is to record so-called zero-field-cooled (ZFC) and field-cooled (FC) curves. Despite the terminology the ZFC curve is recorded in an applied external field while heating the sample up after cooling the sample down from above  $T_B$  without an external field. In the case of superparamagnetism the magnetization will increase once the temperature is high enough to enable switching but will decrease again upon exceeding  $T_B$  due to thermal fluctuations. The FC curve which is recorded thereupon will follow the ZFC curve down to  $T_B$  but will then stay above the magnetization value of  $T_B$  even at lower temperatures as the magnetization gets frozen.

## Chapter 3

# Experimental methods

This chapter deals with the experimental techniques employed in this work and covers their theoretical fundamentals. The samples were analyzed regarding their structural and their magnetic behaviour. For the former scanning tunnelling microscopy (STM), low energy electron diffraction (LEED) and scanning electron microscopy (SEM) were being used. The magnetic characterization was done by in situ MOKE, SQUID magnetometry and ferromagnetic resonance (FMR). The main experimental setup and especially its technical details will be described in the next chapter.

### 3.1 STM

The main method for structural analysis employed in this work is scanning tunnelling microscopy (STM). It was invented in 1982 by Gerd Binnig and Heinrich Rohrer for which they were awarded the Nobel Prize in Physics in 1986. The basic concept of an STM is that an atomically sharp tip usually consisting of tungsten is brought into the closest proximity of a sample surface. Upon applying a bias voltage between the tip and the sample a very small current called the tunnelling current, typically in the nA range, can be measured. By scanning the sample and measuring the tunnelling current at each point of a defined grid the topography of the sample surface can be imaged. First, the elementary theory of STM is described which will yield the dependencies of the tunnelling current. Subsequently, the technical aspects and the operational modes of STM shall be discussed.

#### 3.1.1 Theory of STM

To illustrate quantum tunnelling we consider the most simple case. Here, a particle with the mass  $m$  and the energy  $E$  propagates in the positive  $x$  direction onto a rectangular potential barrier with the height  $U_0$  and the width  $2a$  as depicted in figure 3.1. The width of the potential barrier corresponds to the gap between the tip and the sample

in an STM. According to classical mechanics the momentum of the particle is given by  $p = \sqrt{2m(E - U)}$ . Hence, the particle cannot pass region II in figure 3.1 but will be reflected at the wall of the potential. On the atomic scale, however, particles are described by wave functions. The effect of tunnelling can easily be understood by considering two particles so close to each other that their wave functions overlap. Mathematically, the problem can be solved using the Schrödinger equation

$$\hat{H}\psi(x) = E\psi(x) \quad (3.1)$$

with the Hamiltonian  $\hat{H} = -\frac{\hbar^2}{2m}\nabla^2 + U(x)$ ,  $U(x) = U_0\Theta(a - |x|)$ . The solution is described in detail in various textbooks such as [Sch07] and shall be outlined briefly here.

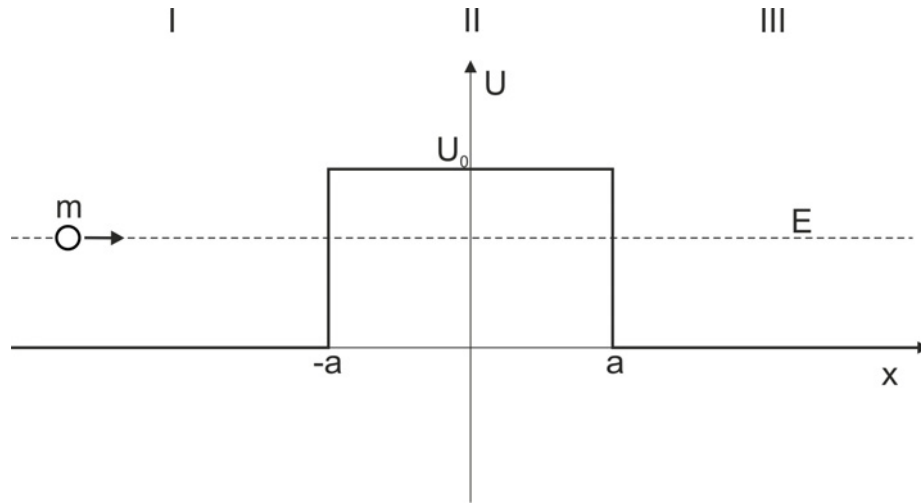


Figure 3.1: A particle with the mass  $m$  and an energy  $E < U_0$  moves toward a rectangular potential barrier.

The most general solution can be written as

$$\psi(x) = \begin{cases} Ae^{ikx} + Be^{-ikx}; & x < -a \\ Ce^{-\kappa x} + De^{\kappa x}; & -a < x < a \\ Fe^{ikx} + Ge^{-ikx}; & x > a. \end{cases} \quad (3.2)$$

with the wave numbers  $k = \sqrt{2mE}/\hbar$  and  $\kappa = \sqrt{2m(U_0 - E)}/\hbar$ . Considering that the particle propagates in the positive  $x$  direction the constant  $G$  can be set as 0. The other constants can be determined by a set of linear equations which results from the continuity conditions of the wave function and its derivative at  $x = -a$  and  $x = a$  as well as the condition of normalization. From this, the transmission amplitude  $S \equiv \frac{F}{A}$  can be obtained as

$$S(E) = \frac{e^{-2ika}}{\cosh 2\kappa a + (i\varepsilon/2) \sinh 2\kappa a}, \quad (3.3)$$

where  $\varepsilon$  is defined by  $\varepsilon = \frac{\kappa}{k} - \frac{k}{\kappa}$ . The transmission coefficient which describes the probability of a particle tunnelling the barrier can then be written as

$$|S(E)|^2 = \frac{1}{1 + (1 + (\varepsilon^2/4)) \sinh^2 2\kappa a}. \quad (3.4)$$

Considering the limiting case of a high and wide potential barrier and making additional analytic approximations the transmission coefficient simplifies to

$$|S(E)|^2 \approx \exp\left(-4\sqrt{2m(U_0 - E)}\frac{a}{\hbar}\right). \quad (3.5)$$

For real systems, the potential barrier will generally not be exactly rectangular but distorted due to the different work functions of the tip and the sample and also because of the electric field between them. Figure 3.2 illustrates this and how the potential can be approximated by  $N$  rectangular potential barriers with the widths  $dx$ . Hence, equation 3.5 must be modified by considering that the probability for a particle tunnelling the entire barrier corresponds to the multiplication of the transmission coefficients for every single rectangular potential barrier. This results in

$$|S(E)|^2 = \prod_{i=1}^N \exp\left(-\frac{\sqrt{2m(U(x_i) - E)}}{\hbar} 2dx\right) \quad (3.6)$$

$$= \exp\left(-2 \sum_{i=1}^N \frac{\sqrt{2m(U(x_i) - E)}}{\hbar} dx\right). \quad (3.7)$$

In the limiting case of  $N \rightarrow \infty$  the sum becomes an integral:

$$|S(E)|^2 = \exp\left(-2 \int_{x=a}^b \frac{\sqrt{2m(U(x) - E)}}{\hbar} dx\right). \quad (3.8)$$

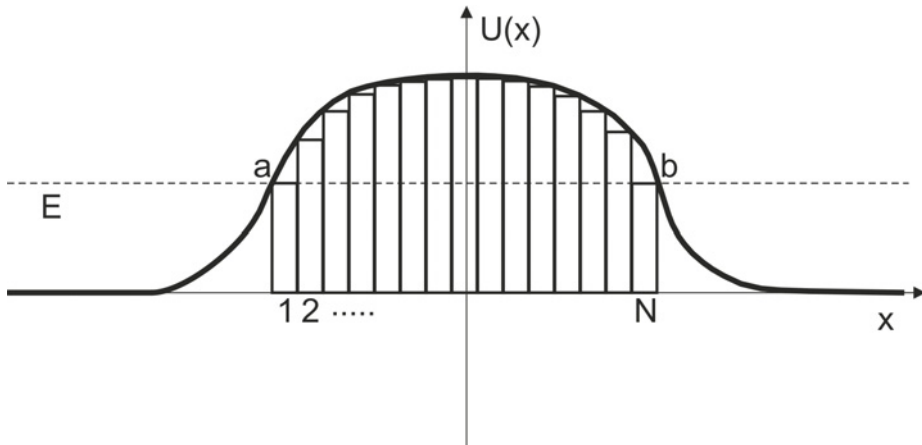


Figure 3.2: One dimensional potential barrier for a real system and its decomposition into  $N$  narrow rectangular potential barriers.

Apart from a prefactor this result corresponds to the WKB approximation<sup>1</sup> for quantum penetrability [Fli00].

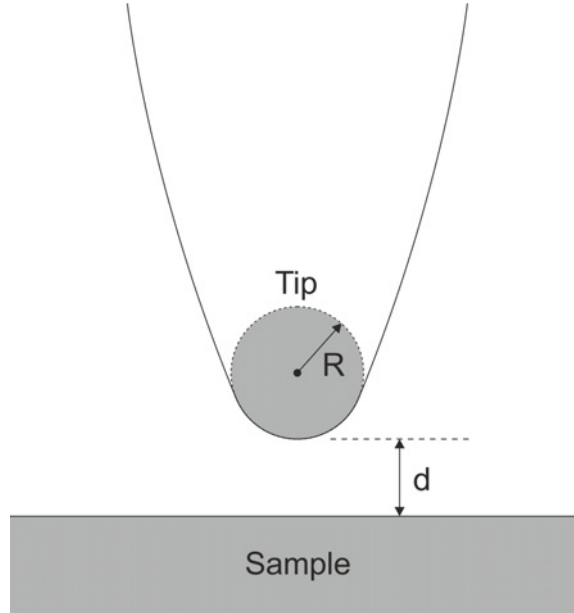


Figure 3.3: Schematic drawing of the tunnelling geometry according to Tersoff. The end of the tip is approximated as a sphere with a radius  $R$ .

For simplicity the one dimensional potential barrier was considered up to now. A three dimensional calculation was first done by Tersoff using the tunnelling matrix element of Bardeen [Ter83, Ter85]. Here, the end of the tip is assumed to be spherical with a radius  $R$  while  $d$  denotes the closest distance between the tip and the sample as shown in figure 3.3. In the limiting cases of small voltages and small temperatures, the tunnelling current can be calculated as

$$I = \frac{2\pi}{\hbar} e^2 U \sum_{\mu\nu} |M_{\mu\nu}|^2 \delta(E_\nu - E_F) \delta(E_\mu - E_F), \quad (3.9)$$

where the indices  $\mu$  and  $\nu$  denote attributes of the tip and the sample respectively. As shown in [Bar61] the matrix elements  $M_{\mu\nu}$  are given by

$$M_{\mu\nu} = -\frac{\hbar^2}{2m} \int d\vec{S} \cdot (\psi_\mu^* \nabla \psi_\nu - \psi_\nu \nabla \psi_\mu^*). \quad (3.10)$$

The integral is taken over an arbitrary surface between the tip and the sample surface. Using wave functions for the tip and the surface as described in [Ter83] the resulting tunnelling

<sup>1</sup>The abbreviation WKB refers to the originators of this approximation, namely Wentzel, Kramers and Brillouin. It consists of making a generalized ansatz  $\psi(x) = \exp\left(\frac{iS(x)}{\hbar}\right)$  for the wave function. Upon insertion into the Schrödinger equation approximations can be made by expanding  $S(x)$  into a series of  $\hbar$ . The WKB approximation usually refers to the wave function obtained by truncating  $S(x)$  after the first order.

current is given by

$$I = 32 \frac{\pi^3}{\hbar} e^2 U \phi^2 D_t(E_F) R^2 k^{-4} e^{2kR} \sum_{\nu} |\psi_{\nu}(\vec{r}_0)|^2 \delta(E_{\nu} - E_F), \quad (3.11)$$

where  $U$  is the applied voltage,  $\phi$  is the work function which for simplicity is assumed to be equal for the tip and the sample,  $D_t$  is the density of states per unit volume of the tip and  $k$  is the inverse decay length for the work functions in vacuum. Using that  $|\psi_{\nu}(\vec{r}_0)|^2 \propto \exp(2k(R+d))$  the tunnelling current is again found to be proportional to  $e^{-2kd}$  as in the one dimensional case.

Another consideration for real systems is that the potential on both sides of the barrier need not be identical due to different work functions of the tip and the sample and also that the local densities of states usually deviate one from another. Upon bringing the tip and the sample with the work functions  $\Phi_{\mu}$  and  $\Phi_{\nu}$  into contact their Fermi energies are aligned resulting in the different vacuum energy levels  $E_{\text{vac},\mu}$  and  $E_{\text{vac},\nu}$  [Hen94]. Figure 3.4 illustrates the case in which a positive bias voltage is applied to the sample allowing electrons in a region between  $E_{F,\mu} - eU$  and  $E_{F,\mu}$  to tunnel from the tip into the sample resulting in

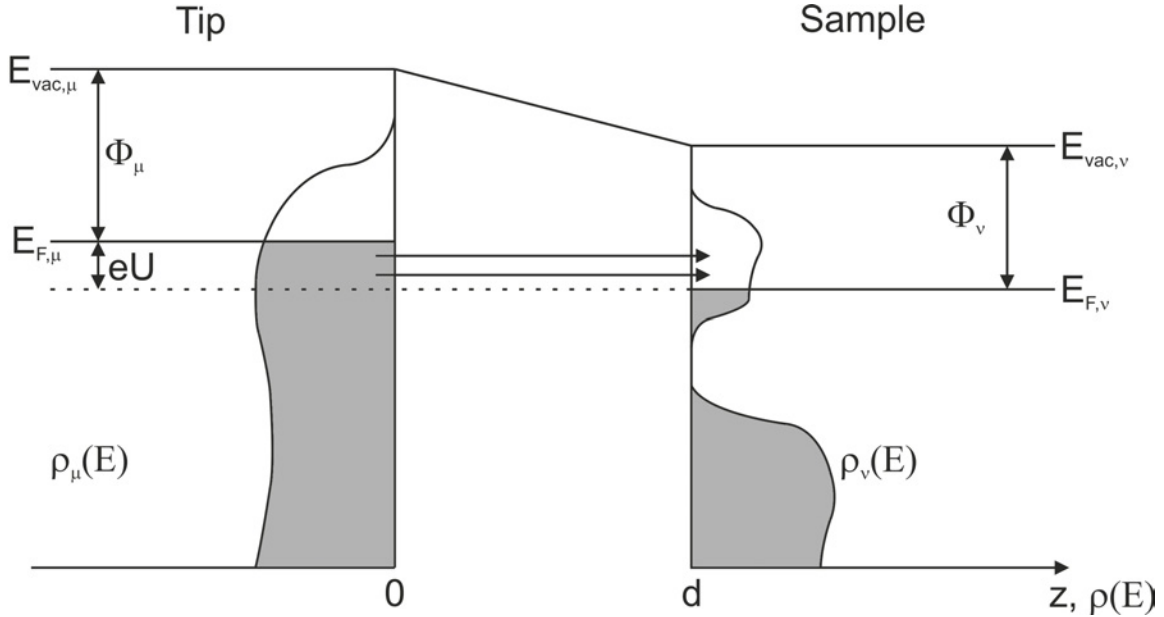


Figure 3.4: Energetic considerations for the tip and the sample in an STM. The grey coloured regions in the densities of states indicate occupied states which according to the Fermi-Dirac distribution means that the case of  $T = 0$  K is considered here. This is, however, still a good approximation even at room temperature. Effective tunnelling takes place in a region between  $E_{F,\mu} - eU$  and  $E_{F,\mu}$ . The shape of  $\rho_{\mu}(E)$  in this schematic drawing implies that it is desirable for the tip to have a relatively constant density of states. This way, bias voltage dependent changes in the tunnelling current can be attributed to the energy dependent densities of states in the sample.

empty state images. The tunnelling current is then given by

$$I \propto \sum_{E_n=E_{F,\mu}-eU}^{E_{F,\mu}} |\psi_n(0)|^2 e^{-2kd}. \quad (3.12)$$

Using the definition of the local density of states (LDOS) [Che93]

$$\rho(z, E) = \frac{1}{\epsilon} \sum_{E_n=E-\epsilon}^E |\psi_n(z)|^2 \quad (3.13)$$

with  $\epsilon = eU$ , and by furthermore assuming that equation 3.12 can be written as

$$I \propto eU \rho(0, E_F) e^{-2kd}. \quad (3.14)$$

### 3.1.2 Experimental aspects of STM

The previous section points out that the measured tunnelling current depends exponentially on the distance between the tip and sample as well as on the local densities of states. Typically, the tip-sample-distance is  $\lesssim 1$  nm for a tunnelling current of 1 nA. Deviations of only about 0.1 nm can already alter the tunnelling current by one order of magnitude [Hen94]. The LDOS can often be neglected if for example the surface consists out of only one sort of atoms which all have equal bonds but it can sometimes have significant impact on the mapping of the surface topography as is the case for Graphite(0001) [Bat87] but also Fe<sub>3</sub>Si which is the main subject of this work.

Regardless of the origin of the tunnelling current the surface topography can be obtained by two fundamental modes of operation. The first is called the *constant height mode* where the measuring signal, i. e. the tunnelling current, is directly being used as the height of  $z$ . In this case the feedback circuit is inactive. Scans can be done on a small time scale but this technique requires very smooth surfaces. The second mode of operation is called the *constant current mode* where the feedback circuit is active which causes a tracking of the tip along the sample surface in order keep the actual tunnelling current at the set tunnelling current. The height of  $z$  is determined by the voltage which is applied to the piezoelectric element for the  $z$ -direction. Apart from the fact that this mode enables the scanning of rough surfaces it also causes the tip to remain close to the surface which yields a higher tunnelling current and thus a better signal-to-noise ratio. The essential components of an STM and their connections are illustrated in figure 3.5. All topography scans shown here were acquired using the constant current mode.

## 3.2 LEED

Besides STM low energy electron diffraction (LEED) was frequently employed in order to obtain information about the surface structure. Unlike STM however, which yields micro-

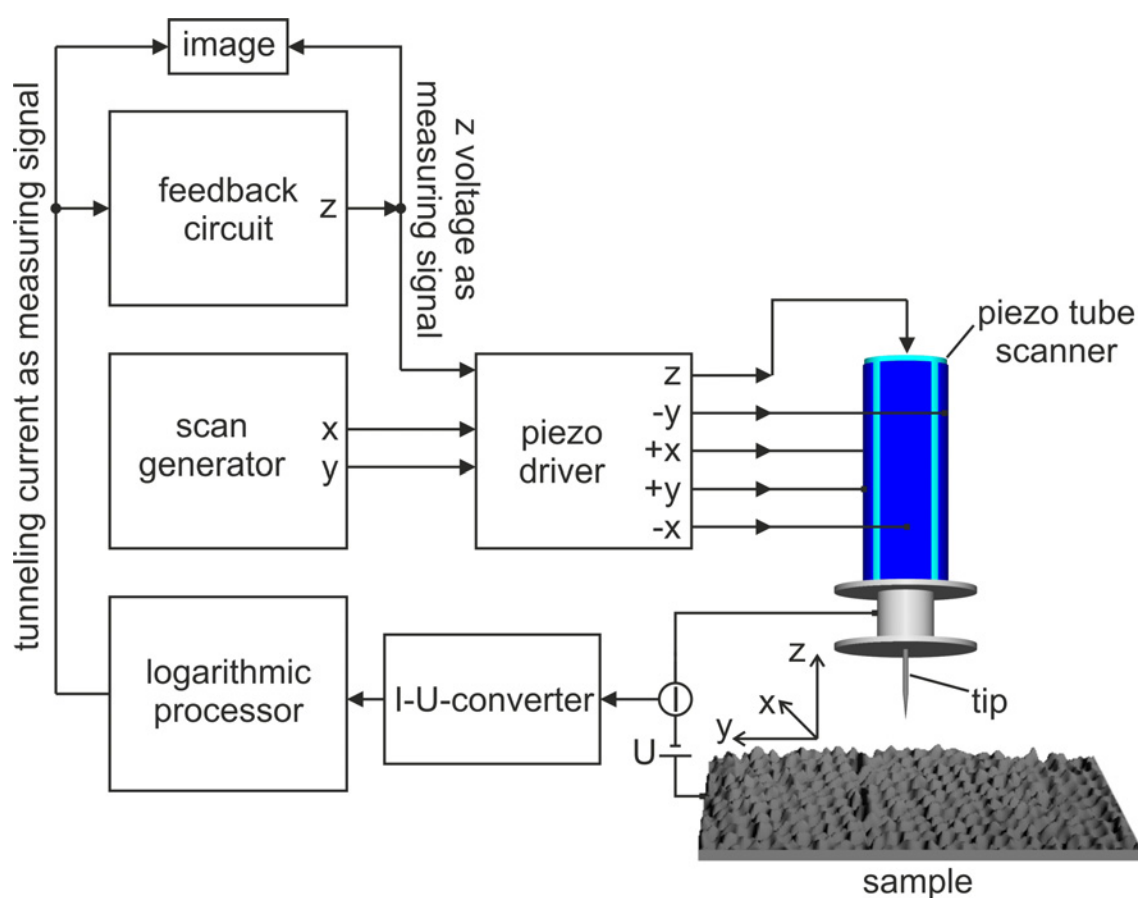


Figure 3.5: Diagram with the essential components of an STM. The tip can be positioned laterally ( $x$ - and  $y$ -directions) and vertically ( $z$ -direction) with respect to the sample by the piezoelectric elements. A bias voltage  $U$  is applied between the sample and the tip. The flow chart points out that the tunnelling current can be taken directly as the measuring signal in the case of the *constant height mode*. Alternatively the tunnelling current can serve as the input for the regulator circuit which causes a tracking of the tip over the sample in the  $z$ -direction in the case of the *constant current mode*.

scopic data in real space, LEED images are in reciprocal space and need to be interpreted as such. While the strength of STM lies in the direct imaging of for example island morphologies and atomic structures LEED averages over larger areas (typically  $1 \text{ mm}^2$  [Sch99]). Thus, the information acquired by LEED is more representative for the entire sample surface.

The most basic information that can be drawn from standard LEED patterns consists in the sharpness of the reflexes and how they are arrayed. The sharpness and the background correlate with the surface quality. Randomly ordered defects increase the background while cluster formation with different domains are the cause for the reflexes to appear blurred. The arrangement of the diffraction spots can be as simple as to represent a  $(1 \times 1)$  structure

where the periodic structure of the surface corresponds to the bulk structure<sup>2</sup>. In many cases, the surface features reconstructions which are the cause for additional diffraction spots in the LEED images.

Similar to other diffraction methods that probe the crystalline structure typical LEED wavelengths range from 0.05 nm to 0.2 nm [Ber92] and are thus in the order of atomic spacings. According to the de Broglie relation  $\lambda = \frac{h}{\sqrt{2mE}}$  the corresponding electron energies range from 30 eV to 500 eV. However, unlike other diffraction methods such as XRD where the radiation penetrates the entire sample LEED is only sensitive to the surface. For the electron energies commonly used in LEED experiments the mean free path of the electrons is approximately 1 nm [Hen94] for all metallic samples (universal curve) and comparable even for other inorganic materials [Sea79].

Using LEED, the conditions for constructive interference can be simplified for two reasons. First, because the influence of the basis of the crystal structure can be neglected as it only causes an intensity modulation over larger diffraction angles. The other reason is that because LEED is surface sensitive the periodicity in the direction perpendicular to the sample surface becomes infinite. As a consequence  $\vec{a}_3^*$ , the corresponding reciprocal lattice vector, becomes infinitesimal and the Laue condition  $\vec{K}_\perp \cdot \vec{a}_3 = h_3 2\pi$  is met for any value of  $\vec{K}_\perp = h_3 \vec{a}_3^*$ . Hence, the points in reciprocal space along the direction of  $\vec{a}_3^*$  lie so close one to another that the point lattice degenerates into an array of rods as shown in figure 3.6 alongside the schematic drawing of a LEED system. As a result the Laue conditions for the diffraction on surfaces simplify to

$$\Delta \vec{k}_\parallel \cdot \vec{a}_1 = 2\pi h_1 \quad (3.15)$$

$$\Delta \vec{k}_\parallel \cdot \vec{a}_2 = 2\pi h_2. \quad (3.16)$$

As long as the electron energy is high enough there will always be an intersection of the rods with the Ewald sphere.

The left hand side of figure 3.6 illustrates the essential components of a LEED setup. The electrons emitted from the cathode are bunched by a Wehnelt cylinder, accelerated by the anode and directed towards the sample by passing a field-free drift tube. After diffraction the electrons need to pass an array of grids before reaching the fluorescent screen. The inner grid is on the same potential as the sample allowing the electrons to travel nearly undeflected up to the screen. A counter-potential is used on the second grid in order to filter out the inelastically scattered electrons. The remaining electrons are again accelerated by the outermost grid. The right hand side of figure 3.6 shows the cross section of the Ewald sphere for  $h_2 = 0$ . It becomes apparent that if the sample is positioned in the centre of the spherical fluorescent screen the curvature of the screen and the Ewald sphere compensate each other. Hence, the observed diffraction spots represent the rods in reciprocal space without distortion.

<sup>2</sup>Throughout this work, Wood's notation is being used where the periodicity of the surface is expressed in terms of the diperiodic net of the bulk substrate structure which lies parallel to the surface [Woo64].

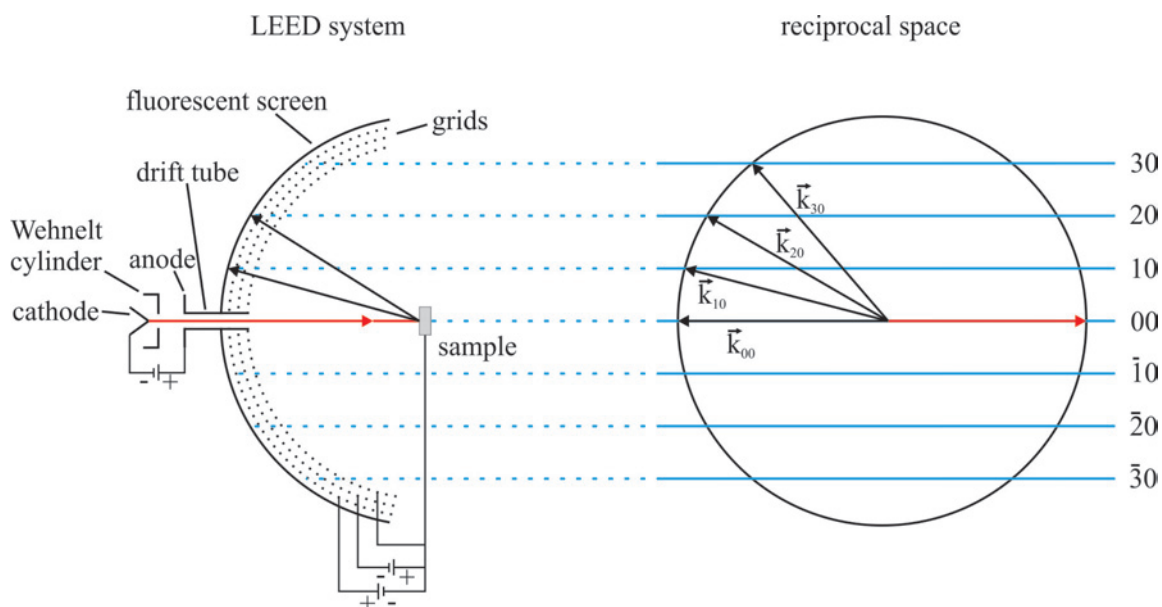


Figure 3.6: The left hand side shows a schematic drawing of a LEED setup with perpendicular incidence of the electron beam onto the sample. The right hand side shows a cross section of the Ewald sphere for  $h_2 = 0$ .

### 3.3 MOKE

The magneto-optical Kerr effect (MOKE) which was already discovered in 1876 by John Kerr has developed into a standard method for the magnetic characterization of thin films over the last one or two decades. The high sensitivity down to the regime of a few monolayers [Urb05] and the simple and non-destructive way of probing using a polarized light beam contributed to its popularity allowing even in situ measurements as they were performed in this work. The technical details of the MOKE setup are described in section 4.2.2. This section will supply fundamentals of MOKE in general and provide the physical background for the setup used here, i.e. the use of a photoelastic modulator (PEM) in the reflected beam prior to passing the analyzer.

In principal there are three magneto-optical effects where light interacts with material either in an external magnetic field or the spontaneous magnetization of the material in a way that the polarization state of the light wave is altered. These are the Faraday effect [Far46], the Voigt effect [Voi99] and MOKE [Ker99]. The former two can be observed if light passes through a material in the presence of a magnetic field. In the case of the Faraday effect the magnetic field is oriented parallel to the propagation direction of the light while in the case of the Voigt effect the magnetic field is perpendicular to that direction. Furthermore, the Faraday effect exhibits a linear dependency on the field strength while the Voigt effect is quadratic. In contrast to that MOKE is observed in reflection and is solely based upon the magnetization of the reflective material. While MOKE is the topic of this section the other

effects are being mentioned here nevertheless because they may also have an influence on the polarization state during measurements caused by impurities on the samples or by the light passing through viewports in the presence of magnetic fields.

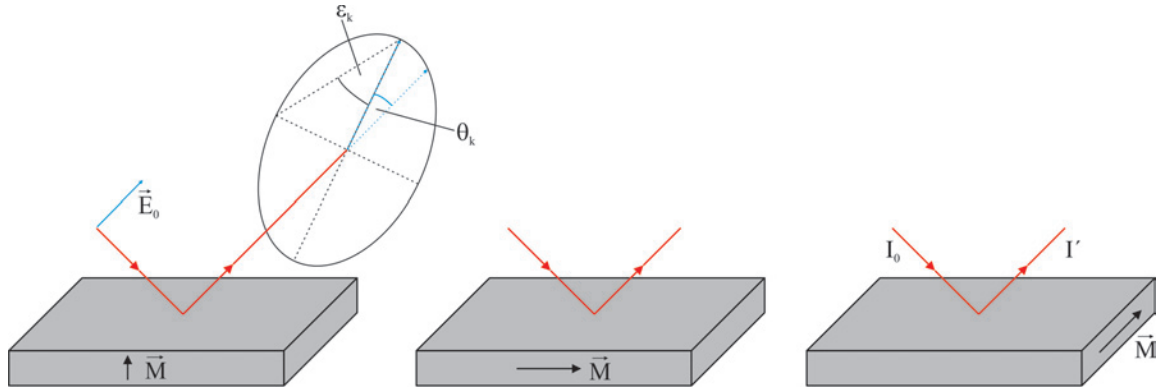


Figure 3.7: The fundamental geometries of MOKE which are the polar, the longitudinal and the transverse geometry from left to right. In the case of a linearly polarized incident beam for the polar and longitudinal geometries the reflected beam is generally elliptically polarized as illustrated on the left hand side for the polar geometry. The modulation of the polarization is described by the Kerr angle  $\theta_k$  and the Kerr ellipticity  $\epsilon_k$ . The transverse MOKE does not cause the polarization to change but results in an intensity modulation.

There are three fundamental MOKE geometries as shown in figure 3.7. In the case of the polar geometry the magnetization is oriented perpendicular to the sample surface. The magnetization direction lies in the plane of incidence and parallel to the surface for the longitudinal geometry. For both the polar and the longitudinal MOKE (LMOKE) the reflected beam is generally elliptically polarized as illustrated on the left hand side of figure 3.7. The ellipse is characterized by the Kerr rotation  $\theta_k$  and the Kerr ellipticity  $\epsilon_k$ . The third case is the transverse geometry for which the magnetization is parallel to the sample surface but perpendicular to the plane of incidence. Unlike the two other geometries it does not influence the polarization state but modulates the intensity of the reflected beam. Further terminology is used for the polarization direction of the incident beam which is called *s*-polarized if the polarization direction is oriented perpendicular to the plane of incidence and *p*-polarized if the polarization direction is oriented parallel to the plane of incidence. Another constraining condition that was assumed for these three fundamental geometries is that the magnetization truly only has components in the directions shown in figure 3.7. Considering for instance the longitudinal geometry the magnetization might at some points during the remagnetization process have components in the polar or transverse direction. Depending on the exact MOKE setup these components can also have an effect on the measuring signal. In fact the only situation where only one component can be detected is that for the polar geometry using normal incidence. In this work, however, where an

LMOKE setup was used, out of plane components of the magnetization can be neglected due to the shape anisotropy of the thin layers.

There are different approaches to finding a mathematical description of the magneto-optical Kerr effect. A simple but vivid description considers the relation between the Kerr angle<sup>3</sup> and the polarization obtained from the Drude-Lorentz model as described in works like [Noo07], [Urb05] and [Wes07]. Here, it is conceived that the electrons in the sample are excited in a way that they begin to oscillate parallel to the polarization direction of the incident beam. In an applied field a Lorentz force acts on them which causes the overall oscillation direction to be tilted with respect to original direction. Hence, the radiation of these electrons, i. e. the reflected beam, exhibits an altered polarization. Due to the fact that the calculations are still somewhat elaborate if presented on a comprehensible level but especially because the result of these calculations yields dependencies not on the magnetization but on the applied field they shall not be presented here. As mentioned above MOKE is not sensitive to the applied field but to the magnetization of the sample. A less illustrative approach but one that is based on quantum mechanical calculations can be found in [Arg55]. Here, the author determines the off-diagonal elements of the dielectric tensor (which generally describe magneto-optical effects) by considering the different probabilities for left- and right-circularly polarized light to excite spin up and spin down electrons whose populations are asymmetrical for ferromagnetic materials. From this it becomes evident that the Kerr angle depends on the magnetization.

Hence, the starting point for the dependence of the magneto-optical Kerr effect is a series expansion of the dielectric tensor:

$$\epsilon_{ij} = \epsilon_{ij}^{(0)} + \left[ \frac{\partial \epsilon_{ij}}{\partial m_k} \right]_{\vec{m}=0} m_k + \frac{1}{2} \left[ \frac{\partial^2 \epsilon_{ij}}{\partial m_l \partial m_s} \right]_{\vec{m}=0} m_l m_s + \dots \quad (3.17)$$

Typically, this series expansion is aborted after the first order. The exact determination of the components can be found in [Bar09].

Finally, there is an approach based solely upon symmetry considerations. For cubic crystals as they were studied in this work the dielectric tensor obtained thusly has the following form [Hub98]:

$$\boldsymbol{\epsilon} = \boldsymbol{\epsilon} \begin{bmatrix} 1 & -iQm_3 & iQm_2 \\ iQm_3 & 1 & -iQm_1 \\ -iQm_2 & iQm_1 & 1 \end{bmatrix} + \begin{bmatrix} B_1m_1^2 & B_2m_1m_2 & B_2m_1m_3 \\ B_2m_1m_2 & B_1m_2^2 & B_2m_2m_3 \\ B_2m_1m_3 & B_2m_2m_3 & B_1m_3^2 \end{bmatrix}. \quad (3.18)$$

The first term on the right hand side describes a magneto-optical rotation due to the Faraday effect for the case of transmission or due to MOKE in the reflective case.  $Q$  is a material constant which is of the order of 0.03 for light in the visible range. It can be seen that the off-diagonal elements in the first order depend linearly on the direction cosines of

<sup>3</sup>Oftentimes the Kerr angle is considered complex-valued and already includes the Kerr ellipticity. Thus, the complex Kerr angle is given by  $\phi_k = \theta_k + i\epsilon_k$

the magnetization  $m_i$ . The second term describes the Voigt effect for which the off-diagonal elements are in the second order of  $m_i$  and  $B_1$  and  $B_2$  are Voigt constants.

As shown in [Yan93] the so-called magneto-optical Fresnel reflection matrix

$$\mathfrak{R} = \begin{pmatrix} r_{pp} & r_{ps} \\ r_{sp} & r_{ss} \end{pmatrix} \quad (3.19)$$

can be derived by solving the Maxwell equations considering the first term of the dielectric tensor in equation 3.18. The matrix components  $r_{ij}$  denote the ratio of the reflected  $i$ -polarized light and the incident  $j$ -polarized light and are given as follows:

$$r_{pp} = \frac{n_1 \cos \theta_0 - n_0 \cos \theta_1}{n_1 \cos \theta_0 + n_0 \cos \theta_1} - i \frac{2n_0 n_1 \cos \theta_0 \sin \theta_1 m_x Q}{n_1 \cos \theta_0 + n_0 \cos \theta_1} \quad (3.20)$$

$$r_{sp} = \frac{i n_0 n_1 \cos \theta_0 (m_y \sin \theta_1 + m_z \cos \theta_1) Q}{(n_1 \cos \theta_0 + n_0 \cos \theta_1)(n_0 \cos \theta_0 + n_1 \cos \theta_1) \cos \theta_1} \quad (3.21)$$

$$r_{ss} = \frac{n_0 \cos \theta_0 - n_1 \cos \theta_1}{n_0 \cos \theta_0 + n_1 \cos \theta_1} \quad (3.22)$$

$$r_{ps} = -\frac{i n_0 n_1 \cos \theta_0 (m_y \sin \theta_1 - m_z \cos \theta_1) Q}{(n_1 \cos \theta_0 + n_0 \cos \theta_1)(n_0 \cos \theta_0 + n_1 \cos \theta_1) \cos \theta_1}. \quad (3.23)$$

In the above equations  $\theta_0$  and  $\theta_1$  are the angle of incidence (usually in air or vacuum) and the refractive angle in the magnetic medium while  $n_0$  and  $n_1$  are the corresponding refractive indices. We can now define the magneto-optical Kerr effect for the longitudinal case, as this is the geometry used throughout this work, for both a  $p$ - and an  $s$ -polarized incident beam:

$$\theta_{\text{long}}^p \equiv r_{sp}/r_{pp} \quad (3.24)$$

$$\theta_{\text{long}}^s \equiv r_{ps}/r_{ss}. \quad (3.25)$$

Using equations 3.20 to 3.23, Snell's law, basic trigonometric relations,  $m_x = m_z = 0$  and  $m_y = 1$  [You96] one can arrive at the following expressions:

$$\theta_{\text{long}}^p = \frac{\cos \theta_0 \tan \theta_1}{\cos(\theta_0 + \theta_1)} \cdot \frac{i n_0 n_1 Q}{(n_1^2 - n_0^2)} \quad (3.26)$$

$$\theta_{\text{long}}^s = -\frac{\cos \theta_0 \tan \theta_1}{\cos(\theta_0 - \theta_1)} \cdot \frac{i n_0 n_1 Q}{(n_1^2 - n_0^2)}. \quad (3.27)$$

In the above formulae it can be seen that the dependencies for  $s$ - and  $p$ -polarized light are almost the same except for the sign and the argument in the cosines of the denominators of the first factors. The dependence on the angle of incidence is plotted in figure 3.8 for both cases. The solid and dashed lines represent theoretical values while the points represent experimental values. For the case of  $s$ -polarized light as it was used here (see section 4.2.2) the maximum is assumed at an angle of incidence between  $65^\circ$  and  $70^\circ$  reaching a Kerr rotation of approximately  $0.033^\circ$ . Up to the modifications of the experimental setup which are described in section 4.2.2 an angle of incidence of  $45^\circ$  was used due to geometrical

constraints in the design of the UHV setup. This corresponds to a decrease of the Kerr rotation down to  $0.023^\circ$  for the sample considered by [You96] or to a relative decrease down to 70%. MOKE measurements after the modifications of the experimental setup were performed under an angle of  $48^\circ$  where the Kerr rotation would assume a value of approximately  $0.027^\circ$ .

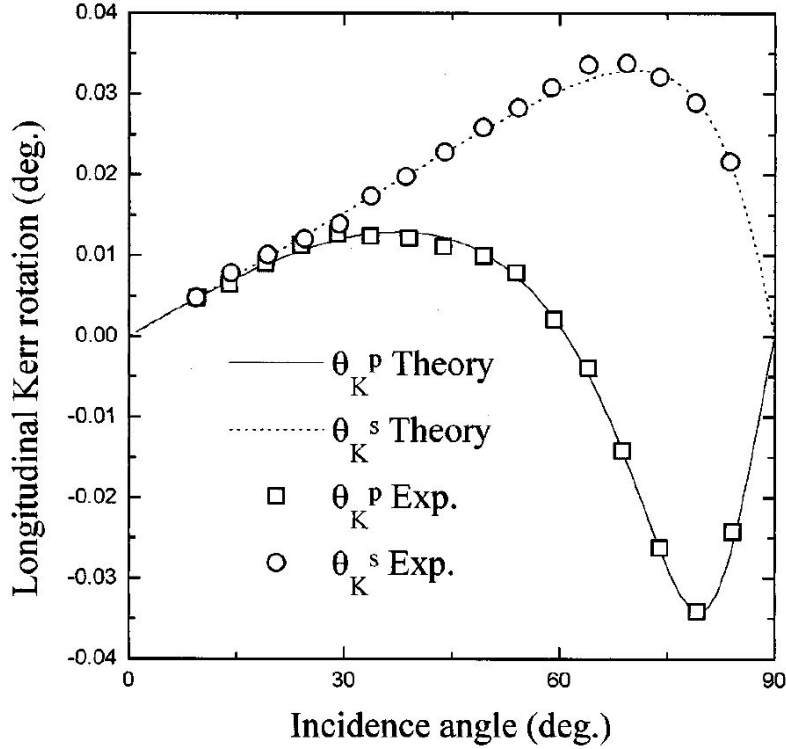


Figure 3.8: Longitudinal MOKE as a function of the angle of incidence [You96]. The experimental data were obtained from measuring a  $(5 \text{ nm Cu}/5.58 \text{ nm Co})_{10}$  multilayer with a refractive index of  $n_1 = 1.58 + 3.58i$  at a wavelength of 632.8 nm.

Up to here, merely the change of polarization of the incident  $s$ - or  $p$ -polarized light due to the magnetization of the sample was considered. In order to increase the signal-to-noise ratio and to transform modulations of the polarization state into intensity modulations, the experimental setup employed in this work also comprises a photoelastic modulator (PEM) and an analyzer. The influence on the polarization state by each of these components is described by a matrix acting on the electric field vector of the light according to the Jones calculus [Jon41]. Detailed calculations for this case can be found in [Pol08] and [Brü13] of which only the main results relevant to this work shall be quoted here. The effective matrix describing the influence of all optical components affecting the polarization state can be written as

$$O_{\text{setup}} = P(\theta_a) \cdot M \cdot \mathfrak{R} \cdot P(\theta_p) \quad (3.28)$$

where  $P(\theta_p)$  and  $P(\theta_a)$  denote the Jones matrices for the polarizer and the analyzer,  $M$  represents the Jones matrix for the PEM and  $\mathfrak{R}$  is the above-mentioned magneto-optical reflection matrix.  $\theta_p$  and  $\theta_a$  are the angles between the transmission axes of the polarizer and the analyzer and the  $x$ -axis of the electric field vector of the light.

As a result, the relation between the polarization state of the incident field vector  $\vec{E}$  and the reflected electric field vector before entering the photo detector  $\vec{E}'$  is given by

$$\vec{E}' = O_{\text{setup}}\vec{E} \quad (3.29)$$

while the corresponding intensity is determined by

$$I \propto |E'|^2. \quad (3.30)$$

Considering the MOKE configuration used in this work, i. e.  $s$ -polarized light or, in other words,  $\theta_p = 90^\circ$ , axes of the PEM at  $0^\circ$  and  $90^\circ$  and a transmission axis of the analyzer at  $45^\circ$ , the total intensity is governed by

$$\begin{aligned} I \propto & \frac{1}{2}r_{\text{ss}}^2 + \frac{1}{2}r_{\text{ps}}^2 + J_0(\varphi_0)r_{\text{ss}}r_{\text{ps}}\cos(\delta_{\text{ss}} - \delta_{\text{ps}}) \\ & + 2J_1(\varphi_0)\sin(\omega t)r_{\text{ss}}r_{\text{ps}}\sin(\delta_{\text{ss}} - \delta_{\text{ps}}) \\ & + 2J_2(\varphi_0)\cos(2\omega t)r_{\text{ss}}r_{\text{ps}}\cos(\delta_{\text{ss}} - \delta_{\text{ps}}). \end{aligned} \quad (3.31)$$

Here,  $J_i(\varphi_0)$  denote the Bessel functions where  $\varphi_0$  is the amplitude of the periodic retardation caused by the PEM according to  $\varphi = \varphi_0 \sin(\omega t)$  and the  $\delta_{ij}$  denote the phase angles of the complex Fresnel reflection coefficients. The first line on the right hand side of equation 3.31 corresponds to an intensity that does not yield a signal after passing the lock-in amplifier because it has no dependence of  $\omega$ . The intensities in the second and the third line in equation 3.31 are modulated with the first and the second harmonic of the PEM frequency  $\omega$ . [Pol08] experimentally verified signal-to-noise ratios of 21.7 for the first harmonic and 45.9 for the second harmonic.

For the interpretation of experimental results it is important to know that part of the Kerr signal is caused by the quadratic magneto-optical Kerr effect (QMOKE) as is already implied by equation 3.17. Bearing this in mind the Kerr angle takes on the form

$$\theta_{\text{long}}^{\text{s/p}} = \pm\alpha_{\text{p}}m_x \pm \beta_{\text{s/p}}m_xm_y \mp \gamma_{\text{s/p}}(m_x^2 - m_y^2) \quad (3.32)$$

under the assumption that  $m_z = 0$  as is the case for in plane magnetization. Here,  $\beta_{\text{s/p}}$  and  $\gamma_{\text{s/p}}$  also depend on the angle between the measuring direction and the main crystallographic axis which is however not essential at this point. It becomes evident that the Kerr rotation no longer linearly depends on the magnetization. In fact the Kerr rotation can even take on larger values during the remagnetization process than for saturation magnetization.

By symmetry considerations as they are shown in figure 3.9 it is possible to separate the linear and the quadratic contributions. For opposite points of the hysteresis loop, i. e. with

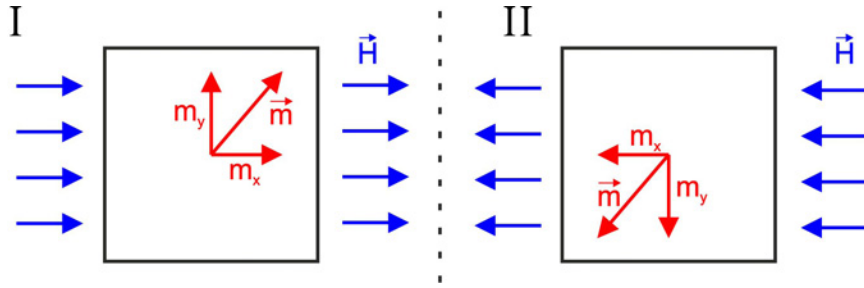


Figure 3.9: Symmetry consideration for the magnetization components at opposite points of the hysteresis loop denoted by I and II [Bar09].

the same applied field and the same history only with different signs, the following relations for the magnetization components can be obtained:

$$m_{x,a} = -m_{x,b} \quad (3.33)$$

$$m_{x,a}m_{y,a} = m_{x,b}m_{y,b} \quad (3.34)$$

$$m_{x,a}^2 = m_{x,b}^2 \quad (3.35)$$

$$m_{y,a}^2 = m_{y,b}^2. \quad (3.36)$$

As a result the first and second order contributions of the LMOKE are given as follows:

$$2 \left( \theta_{\text{long}}^{\text{s/p}} \right)_{\text{lin}} (H) = \theta_{\text{long}}^{\text{s/p}} (H) - \theta_{\text{long}}^{\text{s/p}} (-H) \quad (3.37)$$

$$2 \left( \theta_{\text{long}}^{\text{s/p}} \right)_{\text{quad}} (H) = \theta_{\text{long}}^{\text{s/p}} (H) + \theta_{\text{long}}^{\text{s/p}} (-H). \quad (3.38)$$

Figure 3.10 illustrates how a mixed MOKE signal is split into its first and second order contributions using the relations 3.37 and 3.38. Relation 3.37 was used to obtain the MOKE hysteresis loops presented in this work.

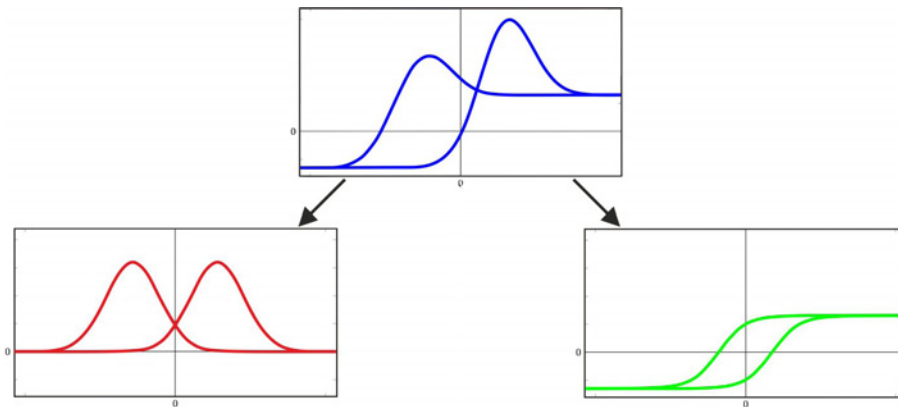


Figure 3.10: Separation of the mixed signal into the first and second order contributions of MOKE.

### 3.4 SQUID

In order to determine the magnetic moment and hence the magnetization of the considered samples quantitatively SQUID magnetometry was used. The quantum interference of Ginzburg-Landau wavefunctions in a superconducting loop separated by one or two Josephson junctions for the cases of rf and dc SQUIDs, respectively, allows the sensitivity of even a fraction of the magnetic flux quantum  $\Phi_0 = h/2e$ . The detailed theories of superconductivity, the Josephson effect and SQUID magnetometry can be found in works like [Buc04] and [Sil67]. This section is meant to give a brief description of the mode of operation of an rf SQUID as it was used in this work.

The magnetization of a sample is not directly measured by the actual SQUID. Instead, the sample is moved parallel to the axis of a pick-up coil which inductively transforms the magnetic flux into a voltage. This is governed by

$$U_{\text{ind}} = -\dot{\Phi} \quad (3.39)$$

with

$$\Phi(t) = \int d\vec{A} \cdot \left( \frac{3\vec{r}(\vec{r} \cdot \vec{\mu}) - \vec{\mu}r^2}{r^5} \right) \quad (3.40)$$

where  $\int d\vec{A}$  is an arbitrary surface enclosed by the pick-up coils. The term in brackets corresponds to the field of a magnetic dipole. This voltage is applied to an oscillating circuit which is close to the superconducting loop thus inducing a current. The total flux through the loop is then given by

$$\Phi = \Phi_{\text{ext}} - LI_C \sin\left(2\pi \frac{\Phi}{\Phi_0}\right). \quad (3.41)$$

Using  $\beta = \frac{2LI_C}{\Phi_0}$  as the so-called screening parameter the relation between the external magnetic flux  $\Phi_{\text{ext}}$  and the total magnetic flux  $\Phi$  is illustrated in figure 3.11. It is biunique for  $\beta < 1$  (blue curve) and exhibits a hysteresis for  $\beta > 1$  (red curve). While in principle both cases can be used for SQUID magnetometry  $\beta < 1$  applies for the SQUID setup employed in this work. Here, the SQUID sensor which can be regarded as a parallel LC circuit due to the inductance of the loop and the capacitance of the Josephson junction acts like a non-linear inductance with its own resonance frequency of

$$f_{\text{res}} = \sqrt{\frac{1}{LC}}. \quad (3.42)$$

It is embedded next to an rf oscillating circuit which induces an alternating current in the loop with a frequency close to the resonance frequency given by equation 3.42 and another feedback controlled loop used as a flux compensator (see figure 3.12). The induced magnetic flux from the sample reduces the resonance frequency of the superconducting loop causing it to cross the frequency of the rf circuit used for excitation. In that case there is a peak in the amplitude of that excitation circuit that is reached every time the flux

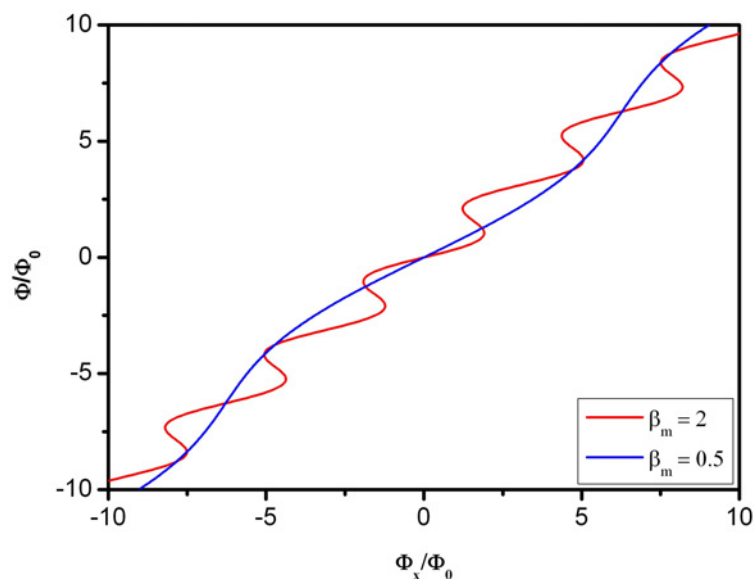


Figure 3.11: Relation between the external magnetic flux  $\Phi_{\text{ext}}$  and the total magnetic flux  $\Phi$  for two exemplary screening parameters.

induced by the sample changes by a value of  $\Phi_0$ . However, the magnetic moment is not directly determined that way but by the voltage applied to the feedback controlled flux compensating loop which causes the resonance frequency of the superconducting loop to remain at a constant level.

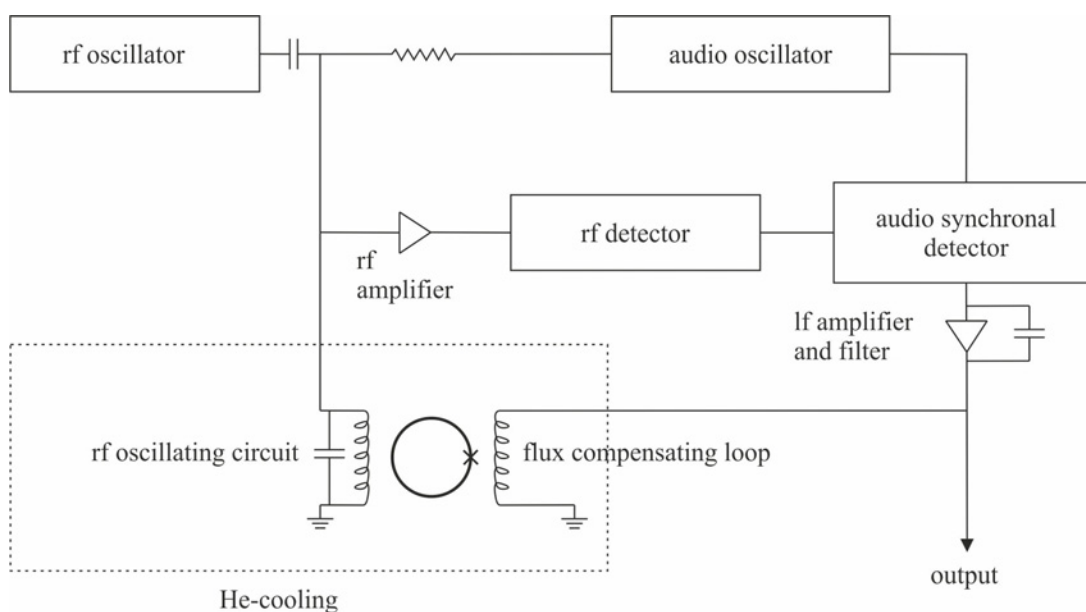


Figure 3.12: Circuit diagram of an rf SQUID.

### 3.5 FMR

Ferromagnetic resonance (FMR) describes the absorption of electromagnetic waves by a ferromagnetic material in the presence of an external magnetic field. The condition for resonance is met when the energy of the radiation corresponds to the Zeeman-splitting of the electronic states caused by the effective field acting on those electrons and can be described by

$$\hbar\omega = g\mu_B B_{\text{eff}} \quad (3.43)$$

where  $g$  is the Landé factor and  $\mu_B$  denotes the Bohr magneton. The effective magnetic field is a function of the external and the generally anisotropic internal fields:

$$\vec{B}_{\text{eff}} = f(\vec{B}_{\text{ext}}, \vec{B}_{\text{int}}). \quad (3.44)$$

In a classical consideration the magnetization of the sample precesses around the direction of  $\vec{B}_{\text{eff}}$  with a frequency  $\omega$ . If  $\omega$  corresponds to the frequency of the radiation resonant absorption takes place. Typical electromagnetic radiation for external fields up to 4 T lies in the microwave regime between 1 GHz and 100 GHz [Spo04]. According to equation 3.43 it is obviously possible to tune either the magnetic field or the microwave frequency to obtain resonance. However, typical microwave sources only operate in a narrow bandwidth of only 1 - 2 GHz which is why it is common to tune the magnetic field as was the case for the FMR measurements done in the scope of this work.

The magnetization dynamics is described by the Landau-Lifshitz-Gilbert equation:

$$\frac{d\vec{M}}{dt} = -\gamma(\vec{M} \times \vec{B}_{\text{eff}}) + \frac{\alpha}{M} \left( \vec{M} \times \frac{d\vec{M}}{dt} \right). \quad (3.45)$$

$\gamma$  is the gyromagnetic ratio defined by  $\gamma = (g\mu_B)/\hbar$  and  $\alpha$  denotes the damping parameter. The first term on the right hand side of equation 3.45 describes the precessional motion caused by the torque acting on the magnetization by the effective field. The second term takes into account the relaxation of the magnetization towards the direction of the effective field and is called the Gilbert damping term. Figure 3.13 illustrates these effects.

The main purpose of the FMR measurements done in this work is the quantitative determination of the magnetic anisotropy constants. According to [Far98] the solution of equation 3.45 and hence the angular dependent condition for resonance is given by the Smit-Beljers formalism:

$$\left( \frac{\omega}{\mu_B g / \hbar} \right)^2 = \frac{1}{M^2 \sin^2(\theta)} \left[ \frac{\partial^2 F}{\partial \theta^2} \frac{\partial^2 F}{\partial \phi^2} - \left( \frac{\partial^2 F}{\partial \theta \partial \phi} \right)^2 \right]. \quad (3.46)$$

Here,  $\phi$  and  $\theta$  are the azimuthal and polar angles of the magnetization vector  $\vec{M}$ . The free-energy density functional  $F$  for cubic systems in reference to [Bar11] is defined by

$$\begin{aligned} F = & -\vec{M} \cdot \vec{B}_{\text{ext}} - MB_{\perp} \cos^2 \theta + K_u \sin^2 \theta \sin^2(\phi - \phi_{K_u}) \\ & + K_1 \sin^2 \theta - \frac{K_1}{8} (7 + \cos(4\phi)) \sin^4 \theta. \end{aligned} \quad (3.47)$$

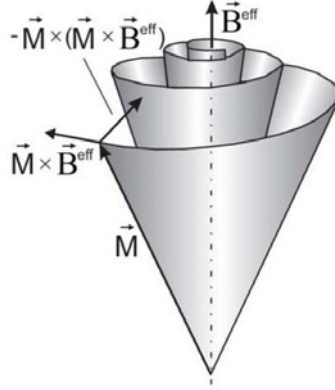


Figure 3.13: Illustration of the magnetization dynamics according to the Landau-Lifshitz-Gilbert equation [Lin02].

The terms on the right hand side of equation 3.47 take into account the Zeeman energy, the perpendicular anisotropy represented by  $B_{\perp}$ , the in plane uniaxial anisotropy  $K_u$  with its easy axis  $\phi_{K_u}$  and the cubic magnetocrystalline anisotropy  $K_1$  respectively. Using  $K_i = B_i M$  and combining the FMR results with the magnetization obtained from SQUID magnetometry (see section 3.4) it is possible to obtain the anisotropy constants  $K_i$ .

FMR measurements were furthermore used to estimate sample homogeneities from FMR linewidths.

### 3.6 RBS

The determination of the thicknesses and the absolute composition of the layers fabricated was done by Rutherford backscattering spectrometry (RBS). Alternative methods such as small angle XRD and the determination of the Bragg peak and then applying Vegard's law<sup>4</sup> only yield either the layer thickness or the composition.

In principal RBS makes use of the elastic scattering of typically protons or He ions by the nuclei in the sample due to the Coulomb interaction. This is described by the well-known formula by Rutherford for the differential cross section:

$$\frac{d\sigma}{d\Omega} = \left( \frac{1}{4\pi\epsilon_0} \frac{Z_1 Z_2 e^2}{4E_0} \frac{1}{\sin^4\left(\frac{\theta}{2}\right)} \right). \quad (3.48)$$

As shown in [May03] the integral cross section is given by

$$\sigma \propto \left( \frac{Z_1 Z_2}{E_0} \right)^2 \frac{[(M_2^2 - M_1^2 \sin^2 \theta)^{1/2} + M_2 \cos \theta]}{M_2 \sin^4 \theta (M_2^2 - M_1^2 \sin^2 \theta)^{1/2}}. \quad (3.49)$$

<sup>4</sup>Vegard's law describes the linear relation between the lattice constant of an alloy and its composition at a constant temperature [Veg21]. For the case of iron silicides it would take on the form  $a_{\text{Fe}_{3-x}\text{Si}_{1+x}} = (1 - bx)a_{\text{Fe}_3\text{Si}}$  where b is a constant.

In the above formulae  $Z_i$  and  $M_i$  are the charges and the masses of the projectile and the target atoms and  $\theta$  is the scattering angle.  $E_0$  is the initial energy of the projectile.

In order to perform the above-mentioned analyses the energy of the backscattered projectiles is determined by a detector (usually a solid state detector) under a fixed angle. Using the relation

$$E_1 = KE_0 \quad (3.50)$$

with

$$K = \frac{M_1^2}{(M_1^2 + M_2^2)^2} \left[ \cos \theta + \left( \left( \frac{M_2^2}{M_1^2} \right)^2 - \sin^2 \theta \right)^{1/2} \right]^2 \quad (3.51)$$

the mass of the scattering particle can be deduced. The energy resolution

$$\Delta E_1 = E_0 \frac{dK}{dM_2} \Delta M_2 \quad (3.52)$$

depends on the slope of the kinetic factor  $K$  which is greater at lower masses and on the energy of the incident projectiles.

# Chapter 4

## Experimental setups

The results presented in this work were obtained from different experimental setups in different work groups. The main setup, however, is a UHV setup in the 'AG Oberflächenphysik' which will be described in the first section of this chapter. Following that is a section about the modifications of the same setup as they were done within the framework of this thesis. This includes the build-up of a Si MBE source as well as the construction of an enhanced version of the in situ MOKE chamber. The concluding section gives an overview of supplementary external setups that were used for measurements.

### 4.1 The existing UHV setup

The experimental setup used for in situ measurements is a UHV chamber containing facilities for sample preparation and their structural and magnetic analysis by STM, LEED and MOKE. A schematic drawing of the apparatus prior to modifications can be seen in figure 4.1. The necessity for UHV is mainly based on the fact that epitaxial growth and also LEED and STM analyses after MBE growth require clean substrate and film surfaces. At a base pressure of  $10^{-6}$  mbar every surface atom is in average hit once per second by a residual gas particle [Hen94] which would quickly lead to contaminations that make surface analysis impossible. The base pressure of the above-mentioned UHV chamber is approximately  $2 \cdot 10^{-10}$  mbar which can be established by a series of pumps. The main chamber is connected to a pump stand (2) (Pfeiffer HiCUBE, pumping speed:  $67 \ell/s$ ) consisting of a turbo molecular pump with a membrane pump as a backing pump and a combination of an ion getter pump (4) (Perkin Elmer, pumping speed:  $200 \ell/s$ ) and a titanium sublimation pump (5) which can be separated from the chamber by an angle valve and a gate valve, respectively. An additional pump stand (3) (Pfeiffer TMH 071 P, pumping speed:  $60 \ell/s$ ) ensures the independent pumping of the load lock and gas inlets.

To reach the base pressure starting from atmospheric pressure a bake-out process is required. This is due to the fact that upon venting the surfaces of the UHV chamber will be covered with particles, especially  $H_2O$ , which would take too long a time to completely

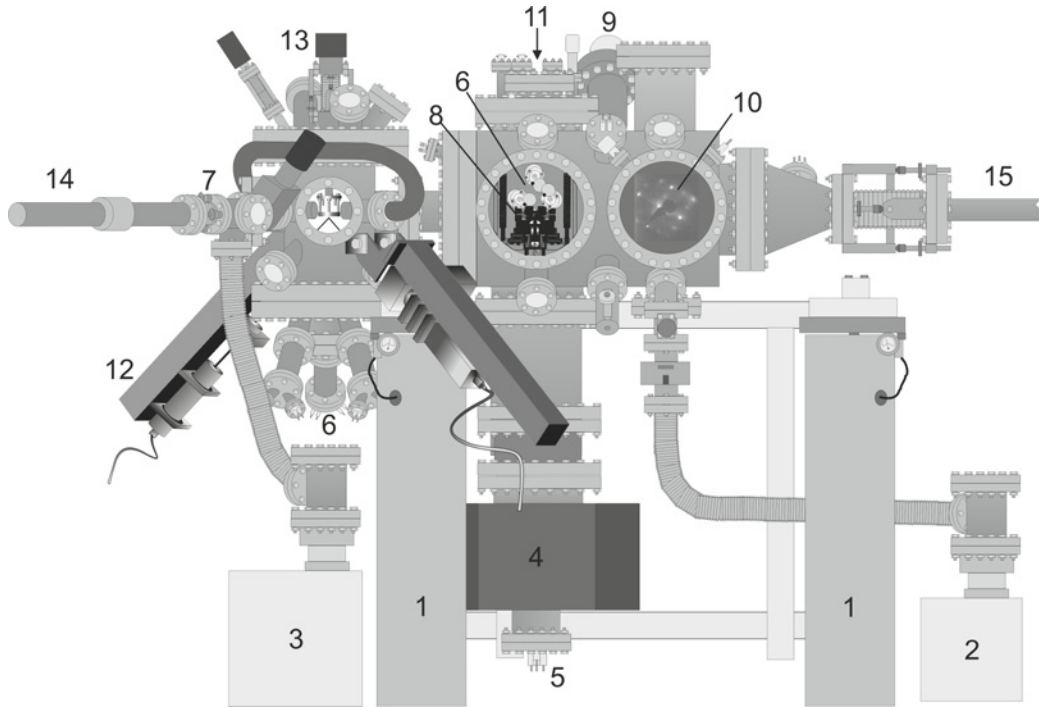


Figure 4.1: Schematic drawing of the experimental setup used for in situ analyses. 1: vibration isolators, 2: main chamber pump stand, 3: load lock and gas inlet pump stand, 4: IGP, 5: TSP, 6: MBE sources, 7: load lock, 8: STM, 9: QMA, 10: LEED, 11: sputter gun, 12: MOKE optics, 13: sample alignment for MOKE, 14: feedthrough for sample transfer, 15: sample manipulator

desorb at room temperature. On the other hand, the desorption rate is high enough to prevent pressures in the  $10^{-10}$  mbar regime. The desorption rate is given by

$$\nu = \nu_0 \cdot \exp\left(-\frac{E}{k_B T}\right) \quad (4.1)$$

where typical values for the characteristic frequency of surface vibrations amount to  $10^{13} \text{ s}^{-1}$  and the typical value for the binding energy of water on steel and glass surfaces amounts to  $80 \text{ kJ mol}^{-1}$  [Hen94]. Hence, by increasing the temperature the desorption rate can easily be increased by several orders of magnitude. Before bake-out the chamber is pumped only by the pump stands for about 12 hours which typically results in a pressure of  $10^{-6}$  mbar which also corresponds to the limit where the ion getter pump can operate. Subsequently, the bake-out process can be started which, at a temperature of  $150^\circ\text{C}$ , takes about 48 hours. After cooling down the pressure amounts to approximately  $10^{-9}$  mbar. At this point the valves connecting the main chamber to the pump stands are closed as the TMPs are no longer effective in this pressure range. The pressure can furthermore be reduced by the use of a titanium sublimation pump and over time. It is also necessary to degas MBE sources, the LEED and the sputter gun until they are operational in the  $10^{-10}$  mbar regime. These procedures usually take about one week. Possible leaks can be localized by performing He

leak tests with the quadrupole mass analyzer before and after the bake-out.

As can be seen in figure 4.1 the main chamber consists of two sections the left of which accommodates MBE sources (Fe and Si throughout this work) and an in situ longitudinal MOKE setup which will be described in detail in the sections 4.1.1, 4.2.1 and 4.2.2. The right section provides an STM (8) (see section 4.1.2) and a LEED setup (10) (Omicron SPECTALEED) for structural analysis, a sputter gun (11) (Specs IQE10-35) for sample preparation and a quadrupole mass analyzer (9) (Balzers QMS 421) that can be used for leak tests and to determine the residual gas composition. Gases can be inserted into the chamber in a controlled fashion via a leak valve. This section also includes a designated MBE flange which can house up to four MBE sources that point to the STM position of the sample. Two of these slots were used for Ag and Au evaporators to provide capping material for the samples. Heating of the samples can be done electrically while attached to the manipulator (15) as described in section 4.1.3 but also on the STM and on one of the sample storage spaces. In total, three samples can be stored inside the UHV system. Another two storage places can hold up to four STM tips each.

The load lock (3) allows for sample and STM tips transfer without having to vent the entire system each time which would result in the above-mentioned bake-out process. Typically, the load lock is pumped for approximately one hour before transfer.

#### 4.1.1 MBE sources

The thin films considered were grown by molecular beam epitaxy and in all cases but for silicon (see section 4.2.1) Knudsen cell evaporators were used for effusion. The purities of the evaporation materials amount to 99.99% for Fe and Au and 99.999% for Ag. The design of such an evaporator is illustrated in figure 4.2. The basic principle is that the deposition material is placed in a crucible that can be heated by a coil-shaped tungsten filament. The material of choice for the crucibles is typically  $\text{Al}_2\text{O}_3$  which features thermal stability, electrical isolation and a low vapour pressure. Furthermore, it does not alloy with most deposition materials. To have as little heat exchange with the environment by conduction the bottom of the crucible is spherical resulting in only one contact point there. Alignment is still possible as the crucible is placed between three ceramic rods also consisting of  $\text{Al}_2\text{O}_3$ . Thermal radiation is, however, not negligible. Therefore, the crucible is enclosed in a water-cooled copper casing. An additional copper heat shield (not shown in the illustration) surrounds the evaporator from just below the copper casing up to the aperture. Both the copper shield and the aperture confine the molecular beam to a conical geometry to prevent that apart from the sample also the chamber is being covered by the evaporate. At a minimal distance of about 0.1 m the deposition on the sample can be regarded as homogeneous. Apart from the aperture there are two additional openings at the top of the evaporator behind which quartz micro balances (Euroquartz HC49) are

positioned. These have a resonance frequency (6 MHz before deposition) that in good approximation changes linearly with the amount of deposited material. Typical changes in the frequency are in the order of  $200 \text{ Hz nm}^{-1}$  while the measurement accuracy of the resonant frequency amounts to approximately 1 Hz. The calibration of the evaporator is done by comparing the change of frequencies of these quartz micro balances with either the layer thickness on the sample by small angle XRD measurements or with the areal density of the deposited material on the sample by RBS measurements. For subsequent experiments it is crucial to maintain the same distance and the same angle between the evaporator and the sample surface as during calibration.

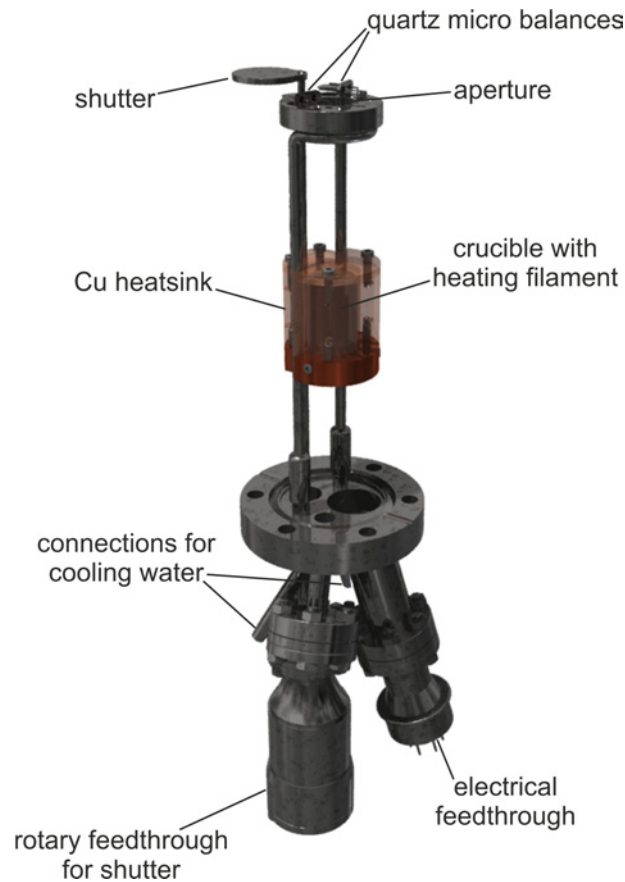


Figure 4.2: Knudsen cell evaporator design as it is being used for the Fe, Ag and Au MBE sources (electrical wirings are not shown).

In order to minimize the contamination of the evaporation material and to degas the evaporator the MBE sources are usually constantly heated just below the point of effusion. Although the molecular beam can be stopped by a shutter which is positioned above the aperture the continuous operation under effusion is not possible due to the limited amount of evaporation material and the life time of the quartz micro balances.

Compared to CVD the deposition rates of the MBE sources employed here are quite low and

are typically in the order of  $0.05 \text{ nm min}^{-1}$ . These low deposition rates are, however, desirable for the epitaxial growth of  $\text{Fe}_3\text{Si}$  and, also, there was no interest in layer thicknesses exceeding 25 nm.

#### 4.1.2 The STM setup

The employed STM is a home-built setup that was originally designed for high temperature and in situ STM measurements. The design of the cartridge including the scanning and the slider unit as well as the heat shieldings date back to K. Reshöft [Res01] while enhancements of the tip exchange and damping mechanisms were done by F. Schäfer [Sch99].

An illustration of the STM design can be seen in figure 4.3. The other ends of the threaded bars shown in the illustration are attached to a DN150CF flange which is mounted to the top of the chamber and which also provides the electrical feedthroughs for the STM.

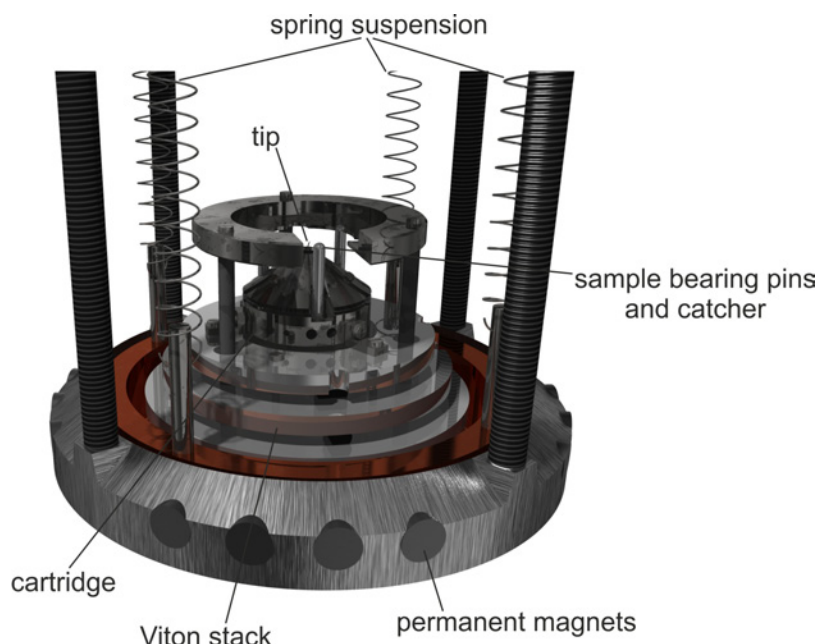


Figure 4.3: Illustrative drawing of the STM design. The scanning unit is located inside a cartridge that is isolated from the environment by spring suspensions, an eddy current brake and an array of steel sheets which are isolated one from another by Viton cylinders.

The setup contains a number of damping mechanisms to isolate the actual scanning unit and the sample from environmental vibrations. For one, the entire UHV chamber can be pneumatically elevated by the vibration isolators shown in figure 4.1. To furthermore reduce vibrations that can be transmitted by bellows connected to pump stands these can be turned off after closing the corresponding valves. The STM unit itself can be isolated by three further mechanisms as depicted in figure 4.3. The first consists of spring suspensions which are damped by strips of Viton. This also serves to align the STM base plate. This

copper base plate is centred in a stainless steel ring that contains a symmetric array of bar magnets which act like an eddy current brake on the base plate. Finally, the base plate and the topmost stainless steel sheet to which the scanning unit and the sample bearing pins are attached are separated by another two stainless steel sheets. The sheets as well as the base plate are isolated by cylindrical pieces of Viton which results in a construction referred to as the Viton stack.

Both the casing of the scanning unit as well as the sample bearing pins are made of Invar<sup>1</sup> which features very low thermal expansion. Although no high temperature STM scans were done in the scope of this work this was still useful to counteract thermal drifts when the sample had some residual heat after annealing.

The circuit diagram of the STM setup is similar to the diagram shown in figure 3.5. The measurement computer is connected to the STM electronics (Createc) via USB. From here, the  $x$ ,  $y$  and  $z$  control signals pass through a piezo drive before reaching the piezo elements. The maximum voltage amounts to  $\pm 150$  V and, depending on the amplification, the maximum scan range amounts to approximately  $(25 \mu\text{m})^2$ . A coarse approach in  $z$  direction is done by a linear motor (Omicron micro slide) which is actuated either manually or ramp-controlled by the STM software (SPS - Createc STMAFM) and the STM electronics. The tunnelling current is amplified by an I-U converter (DL Instruments, Model 564) which is usually set to an amplification factor of  $10^8$ , meaning that a current of 1 nA results in a signal of 0.1 V.

STM tips are fabricated from pieces of tungsten wire with a diameter of 0.25 mm which are electrochemically etched in an NaOH solution with a concentration of  $2 \text{ mol } \ell^{-1}$ . Details of the etching procedure are described in [Kle97] where, however, not the remaining part of the wire attached to the clamping electrode but the drop-off part of the wire is used as an STM tip. Following that, they are transferred to a HV chamber where they are flash-annealed in three steps with increasing temperature. Before inserting them into designated tip holders they are visually inspected using an optical microscope. The tip holders have a conical bottom side which fits exactly onto an inlet attached to the top of the tube scanner. As mentioned in section 4.1 STM tips can be transferred into the UHV system via the load lock which extends maintenance intervals of the setup. The tips can be transferred from their storage places onto the STM by use of a fork-shaped tool that can be attached to the manipulator with a bayonet connector.

### 4.1.3 Sample holders

Different requirements regarding sample manipulation resulted in the sample holder design as it is shown in figure 4.4. Sample holders basically consist of two segments which are

---

<sup>1</sup>Invar is an alloy containing 64 % Fe and 36 % Ni. In the range of  $20^\circ\text{C}$  and  $90^\circ\text{C}$  its thermal expansion coefficient lies between  $1.7 \cdot 10^{-6} \text{ K}^{-1}$  and  $2.0 \cdot 10^{-6} \text{ K}^{-1}$  and is thus nine times smaller than that of stainless steel [Res01].

electrically isolated from each other. The segments are made of molybdenum or titanium which both have high melting points and low vapour pressures even at high temperatures. A further requirement for all parts of the sample holder is to be non-magnetic which is necessary for in situ MOKE measurements. Figure 4.4 shows the bayonet connectors by which the sample holder can be connected to and disconnected from the manipulator head. A spring mechanism inside the manipulator ensures that the connection stays in place.

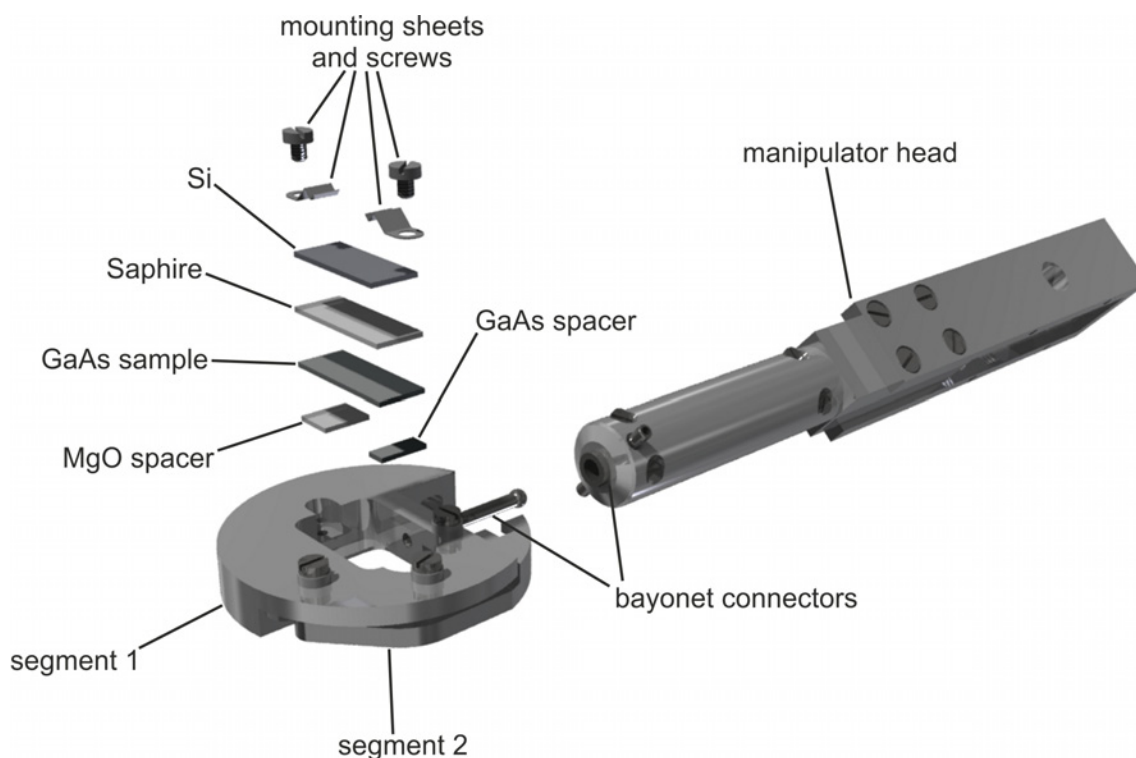


Figure 4.4: Sample and sample holder assembly. Locking onto manipulator heads is done with bayonet connectors. GaAs samples are heated indirectly by a silicon strip where the heat is transferred through a strip of sapphire. Spacers avoid the direct contact between the sample and the sample holder where one spacer consists of MgO which can be used for RBS analysis.

In order to prevent the contamination of the sample with the sample holder material due to diffusion which especially takes place at higher temperatures direct contact is avoided by the use of spacers. While one of the spacers consists of the sample material GaAs the material chosen for the other spacer is MgO for two reasons. First, because MgO is used as a reference substrate for RBS analysis as is described in section 3.6 as the spacer also protrudes over the edge of the contact surface of the sample holder and is therefore visible for the molecular beams. The other reason is that there should not be an electrical contacting between the GaAs sample and both segments of the sample holder. The reason for that is that annealing of the sample at elevated temperatures which reach up to 600 °C by direct current flow turned out to be unstable. The possibility to adjust the heating

current by a temperature-controlled feedback loop was circumvented by using a silicon strip cut from an antimony-doped Si wafer for heating. A sapphire strip is placed between the silicon strip and the sample which is electrically isolating but provides sufficient heat conductivity. As shown in figure 4.4 this stack of spacers, the sample, the sapphire and the silicon strip is then clamped onto the sample holder by tantalum spring sheets.

Since the emissivity  $\varepsilon$  of the of the sample depends on the temperature and also because at different temperatures the sample is more or less transparent in the infrared measuring range of the pyrometer,  $\varepsilon(T)$  was initially determined by measuring the temperature at the sample position with a NiCr-Ni thermocouple as shown in figure 4.5.

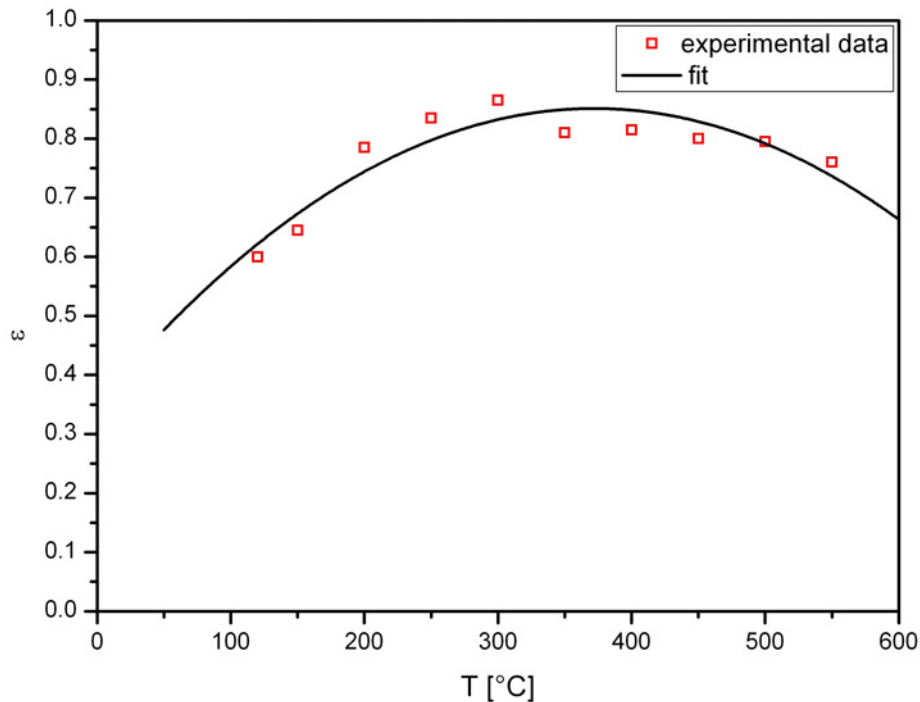


Figure 4.5: The emissivity as a function of the temperature for indirectly heated GaAs samples.

## 4.2 Modifications of the experimental setup

In the course of this work, parts of the original setup as it was described in the previous section were modified for different reasons. This concerns mainly the part of the UHV chamber shown on the left hand side of figure 4.1 which is used for MBE growth and in situ MOKE and which is henceforth referred to as the MOKE chamber (the build-up of this chamber is described in [Urb05]).

One reason arose from the fact that it was still in a prototypical stage. Early experiments showed that despite a design that was flawless regarding the integration into the UHV system and that basically allowed collision-free sample manipulations certain operations were

rather tedious. This applies, for one, for the transfer from the MOKE sample mount into the chamber containing the STM as the axis of the MOKE magnet was not perpendicular to the direction of the sample transfer but drew an angle of  $45^\circ$  with it. Also, the sample constantly needed to be re-aligned during angular dependent MOKE measurements due to small-sized viewports (DN38CF) for the incident and reflected laser beam.

The paramount motivation for modifications of the setup was, however, the integration of a cryostat which would finally require a new design for a MOKE chamber that should also resolve the above-mentioned handling problems. The use of a cryostat should open the path to a whole new set of experiments such as the MBE growth at lower temperatures. For systems like Fe/GaAs which at room temperature basically exhibits Volmer-Weber growth [God08] this could create a layerwise growth and prevent the formation of magnetically inactive layers. Furthermore, the integration of a cryostat would create the possibility to obtain temperature-dependent magnetic quantities by MOKE such as the coercive field or the saturation magnetization which could be used to determine Curie temperatures or the temperature dependence of magnetic anisotropy constants.

The following two subsections summarize the main modifications that were carried out on the experimental setup. While the first section describes the build-up of a silicon MBE source which was essential for the growth of  $\text{Fe}_3\text{Si}$  the second section describes the construction of a new MOKE chamber including the integration of a cryostat and other new components.

#### 4.2.1 Electron beam Si evaporator

An electron beam evaporator (Omicron EFM 3) the design of which is illustrated in figure 4.6 served as the basis for the silicon MBE source that needed to be build up for the growth of  $\text{Fe}_3\text{Si}$  layers. In contrast to the Knudsen cell evaporators where the material is evaporated from a crucible which is surrounded by a heating coil using an electron beam evaporator the material is heated by the bombardment with electrons which are provided by thermionic emission from a filament which surrounds the source material. In this setup, the filament is made from a thoriated tungsten wire which is spot-welded to the filament holder in a way that it surrounds the source material as a spiral with one turn and a diameter of approximately 10 mm.

In the course of establishing a stable source different forms for Si evaporation were experimented with. In one version, Si was placed inside a pyrolytic graphite crucible. This proved to be problematic as the crucible disintegrated increasingly over time and EDX analyses on test samples showed that besides silicon also carbon and tantalum (presumably from the mounting sheets) were deposited. In another version, Si was deposited from a rod with a diameter of 2 mm. Although this solved the problem with the co-deposition of other elements a new problem arose as the Si rod was geometrically unstable during deposition. The general difficulty concerning the evaporation of silicon is that for acceptable deposition

rates one must go close to the melting point of  $1410\text{ }^{\circ}\text{C}$ . For comparison, to reach a vapour pressure of  $10^{-4}$  mbar Si has to be heated up to  $1260\text{ }^{\circ}\text{C}$  while Fe exhibits the same vapour pressure at  $1150\text{ }^{\circ}\text{C}$  although the melting point of Fe is at  $1538\text{ }^{\circ}\text{C}$  [Hon57]. In fact, from other experimenters who are using the Si cell temperature to control the composition of iron silicide layers (after calibration with XRD) as in [Her04] it is known that temperatures as high as  $1400\text{ }^{\circ}\text{C}$  are required. For the deposition from the relatively thin rod this means that small heating fluctuations can already cause the tip to melt which then takes on the shape of a sphere which over time increases in size requiring more and more power for evaporation.

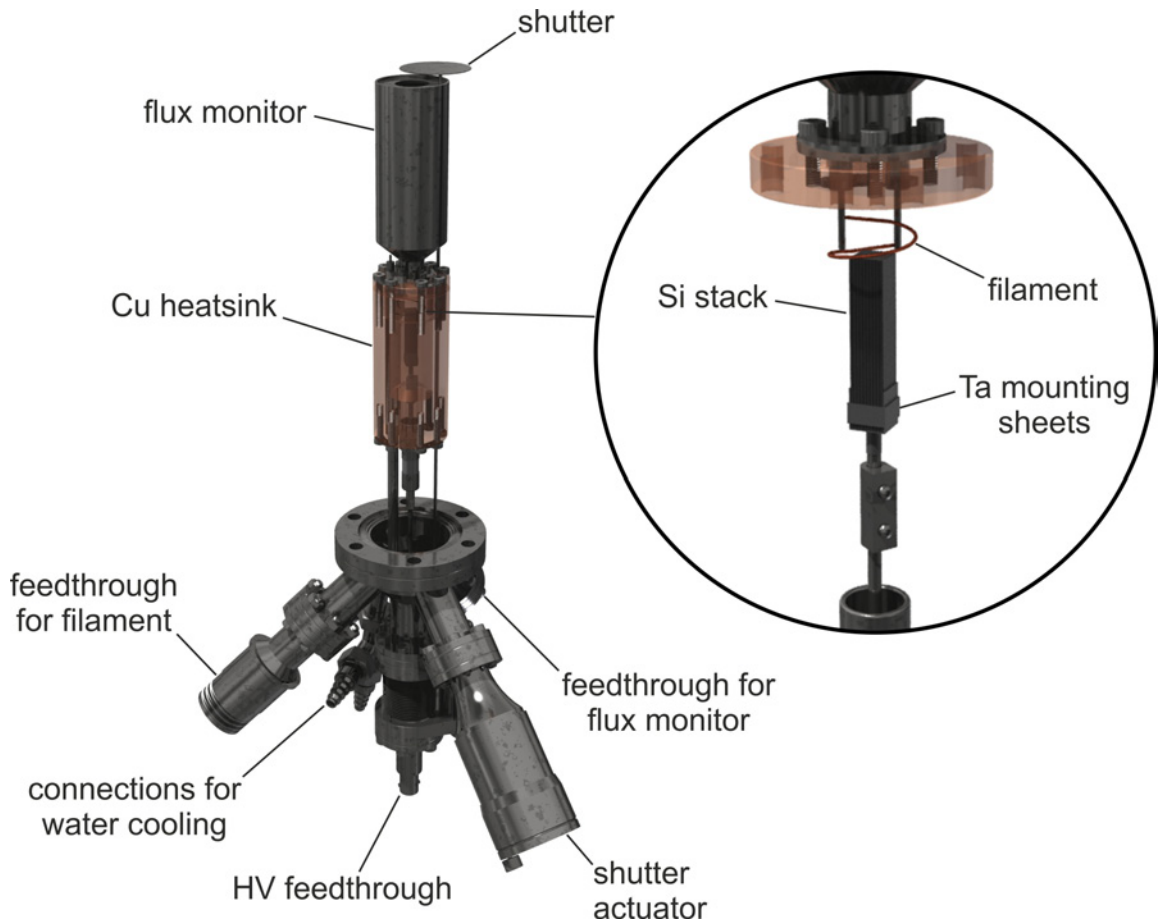


Figure 4.6: Setup of an electron beam evaporator as it was used for the MBE growth of silicon (electrical wirings are not shown). The zoomed in part shows that the source material consists of Si strips which were cut from a wafer and which are held together by sheets of tantalum. The deposition rate can be observed with a flux monitor.

In order to cope with the temperature susceptibility of the source material two measures were taken. One was to employ a larger block of deposition material. Since rods with larger diameters were not available strips cut from a silicon wafer were used to form a block with

a base area of  $(5\text{ mm})^2$  that was tied together on one end by tantalum sheets as shown in the zoom-in in figure 4.6. The other measure was to control the deposition rate with a feedback loop which regulates the filament current. This also required a more accurate determination of the deposition rate. The usual method of employing quartz microbalances turned out to be unreliable which is due to the fact that these had to be placed next to the sample mount because they could not be integrated into the electron beam evaporator. The distance from the source to the quartz microbalances was then three times larger than in the case of the Knudsen cell evaporators and also the deposition rate of Si is about three times less compared to the deposition rate of iron which resulted in frequency changes of about  $20\text{ Hz nm}^{-1}$  or  $0.3\text{ Hz min}^{-1}$ . These are rates which are too small compared to the measurement accuracies of the quartz microbalances (see section 4.1.1). A more precise determination of the deposition rate could be realized by using the flux monitor of the electron beam evaporator which collects a part of the evaporated material which is ionized. Typical currents at the output of the flux monitor at the employed deposition rates amount to 1 to 10 nA which is comparable or slightly larger than typical tunnelling currents of an STM. Hence, the same  $I$ - $U$  converter described in section 4.1.2 was used for amplification. The circuit diagram of the electron beam evaporator can be seen in figure 4.7. For the measurement of the flux monitor current and the control voltage of the filament power supply the D/A converter (National Instruments PCI-6014) of the measurement computer was used in combination with a user-written software programmed in C++. While this allowed the surveillance of the flux monitor current and thus the deposition rate along

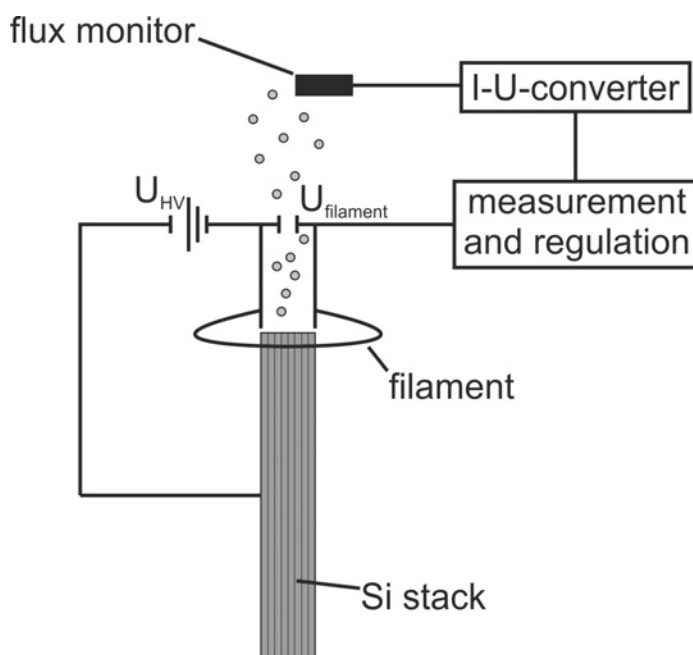


Figure 4.7: Circuit diagram of the Si electron beam evaporator.

with its integration over time the regulation of the filament current could be done using a proportionally controlled feedback loop where the P gain is user-defined. The software furthermore provides the possibility to power up the electron beam evaporator in a controlled way which conserves the lifetime of the Si stack.

#### 4.2.2 MOKE/MBE chamber with cryostat

As mentioned before the main reason for the design and the construction of a new MOKE chamber was the integration of a cryostat. During the alteration works also other aspects about this part of the setup could be ameliorated. The following is a list of the experimental enhancements which could be achieved:

- MOKE measurements at low temperatures
- low temperature deposition
- easier alignment for MOKE
- Kerr rotation increased due to greater angle of incidence
- easier sample transfer due to new geometry
- possible magnetic field increased from 50 mT to 90 mT

Figure 4.8 illustrates the redesigned UHV MOKE chamber including all modifications. The base flange which provides access for the Fe and Si MBE sources as well as the viewports could be retained from the original setup while the top flange had to be redesigned in order to be able to accommodate the cryostat and the differentially pumped rotary feedthrough. The axis of the feedthrough used for transferring the samples from the load lock into the MOKE chamber now coincides with the axis of the manipulator of the STM chamber (see figure 4.1). Both are oriented perpendicular to the axis of the MOKE electromagnet which facilitates sample transfer. Flanges for connecting the MOKE electromagnet and the MOKE viewports have increased in size from DN38CF to DN63CF. This allows the use of larger core diameters for the magnet on the one hand and it provides more tolerance for MOKE alignment on the other hand. Furthermore, special DN63CF viewports were used in order to minimize additional magneto-optical effects like the Faraday effect. By increasing the angle of incidence for the MOKE laser beam from 45° to 48° the Kerr rotation could be increased by approximately 17% (see section 3.3) while maintaining the same gap of 42 mm between the pole shoes. A UHV screwdriver with an M5 Allen key bit is used for lowering and elevating the sample within the new sample mount. This can be done in combination with a torque wrench in order to obtain a defined contact pressure for cooling with the cryostat. The new components and the MOKE setup will be described in more detail in the following.

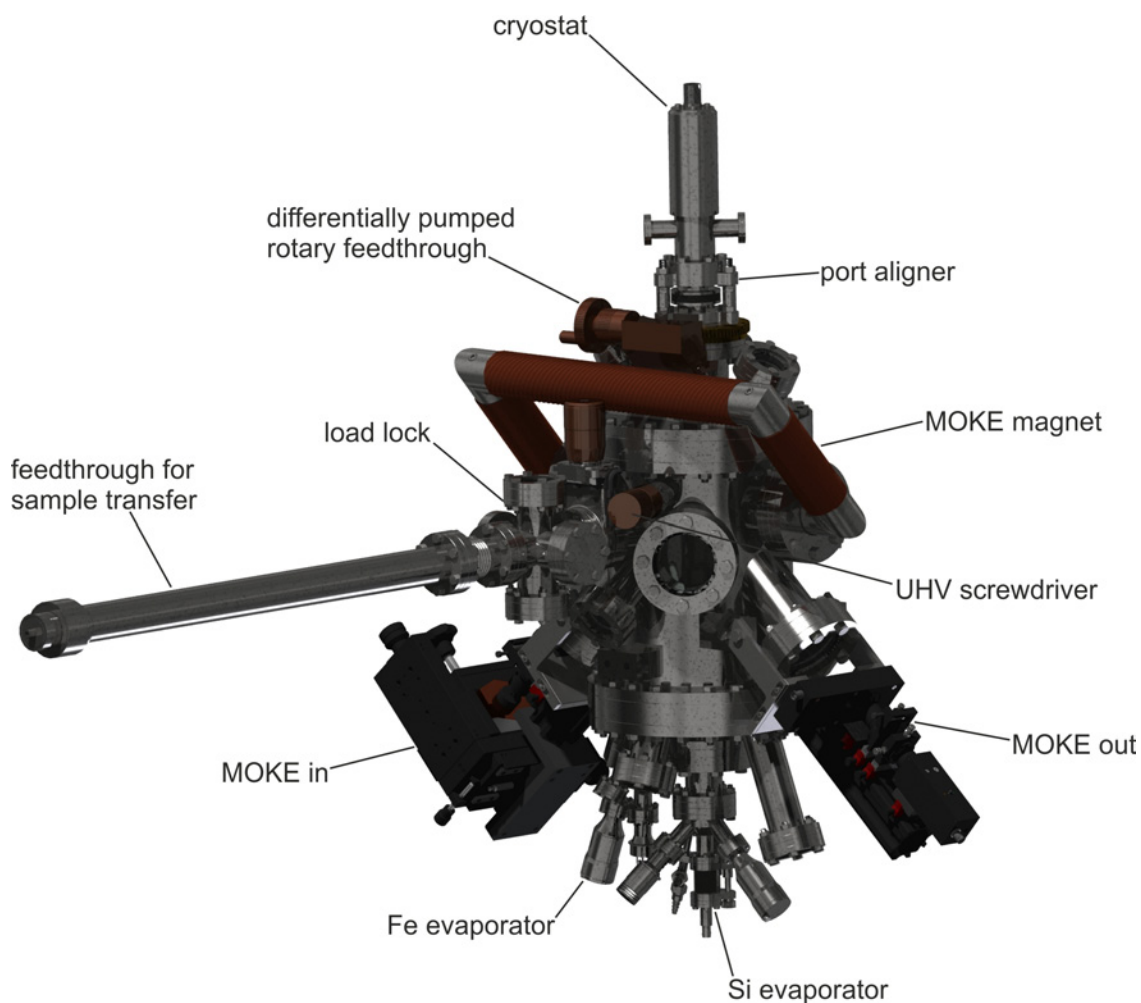


Figure 4.8: Schematic drawing of the redesigned UHV MOKE chamber after the completion of all modifications.

### The MOKE magnet

In order to increase the magnetic field disposable for MOKE measurements a new electromagnet with an increased core diameter of 50 mm was built. ARMCO iron was used as the core material which provides a high saturation field of 2.15 T while exhibiting low remanence and low coercive fields. To increase the magnetic flux density while still providing a homogeneous field at the sample position the pole shoes have the shape of a truncated cone with an aperture of  $110^\circ$  [Red07]. The total turns density resulting from two winding layers amounts to  $1000\text{ m}^{-1}$  using a copper wire gauge of 2 mm. The gauge of the copper wire was chosen in order to obtain two winding layers to provide sufficient cooling from both the core-side and the air-side while having a total resistance of about  $1\ \Omega$  which results in the highest possible wattage for the employed power supply (HH-CM EA-PS 3032-20B). The Hall sensors (Honeywell SS491 using a supply voltage of 9 V) used

for measuring the magnetic field were attached close to the pole shoes of the electromagnet using UHV-compatible two-component adhesive. Calibration was done using a gaussmeter (LakeShore Model 421) the probe of which was placed at the designated sample position. The left hand side of figure 4.9 shows the calibration for both Hall sensors. Using a coil current of 20 A magnetic fields of approximately 90 mT could be established as can be seen on the right hand side of figure 4.9. It also becomes evident that the magnetic field starts to saturate at coil currents of about 15 A.

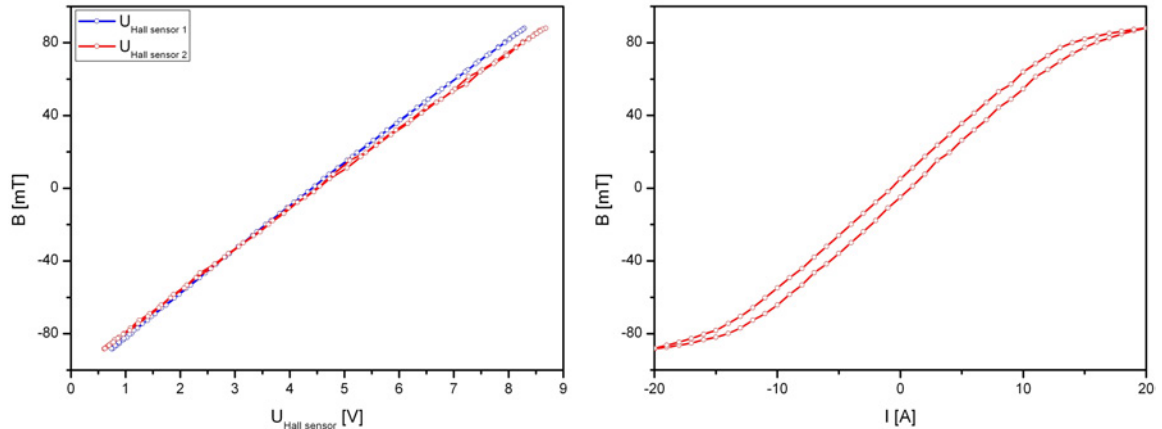


Figure 4.9: Left: Calibration of the Hall sensors. Right: Magnetic field as a function of the coil current.

### Cryostat and sample mount

Cooling of the samples was provided by a bakeable flow cryostat (ARS LT-3B) guaranteeing low levels of vibrations and UHV compatibility down to  $1.33 \cdot 10^{-11}$  mbar. The cryostat is specified to reach 1.7 K using liquid helium and 77 K in liquid nitrogen operation where experiments up to now were restricted to the latter. Low heat loss is provided by using a transfer line with co-axial shield flow. For temperature monitoring and control the cryostat unit includes two thermodiodes of which one is attached to the cryostat head and one to the sample mount. These elements are connected to a temperature control unit (ARS CC-32B) which together with a flow control unit and a needle valve at the cryostat end of the transfer line serve for temperature adjustment.

The requirements for the sample mount were sufficient thermal connection with the cryostat head, sufficient contact pressure for the sample, accessibility for the manipulators, adequate spacing for alignment between the magnetic pole shoes and finally visibility for the MOKE laser beam. This eventually led to the design which is illustrated in figure 4.10. The thermal conductivity of this sample mount is ensured by its copper heat sink. By placing an indium foil between the contact surfaces of the topmost copper element and the cryostat head the thermal connection is further increased. The heat capacity is kept as

low as possible by minimizing the volume of the casing. The outermost diameter of this contraction amounts to 37 mm leaving enough space for alignment. As can be seen in the illustration the rotational motion of the adjustment screw is transferred to the threaded bar via two bevel gears. While the threaded bar stays in place a platform which is connected to the lower part containing the pocket for the sample holders by four beams moving in guiding rails at the sides of the copper heat sink can be elevated or lowered, thus moving the sample up or down. To reduce friction, the bevel gears and also the guiding rails were covered with MoS<sub>2</sub> powder suspended in isopropanol. The area of support of the sample in the pocket is bevelled towards the centre to enable the MOKE laser beam to access the sample surface. The temperature can be monitored by the remaining thermodiode of the cryostat which is clamped to the lower copper plate by a spot-welded strip of tantalum (not shown in the illustration).

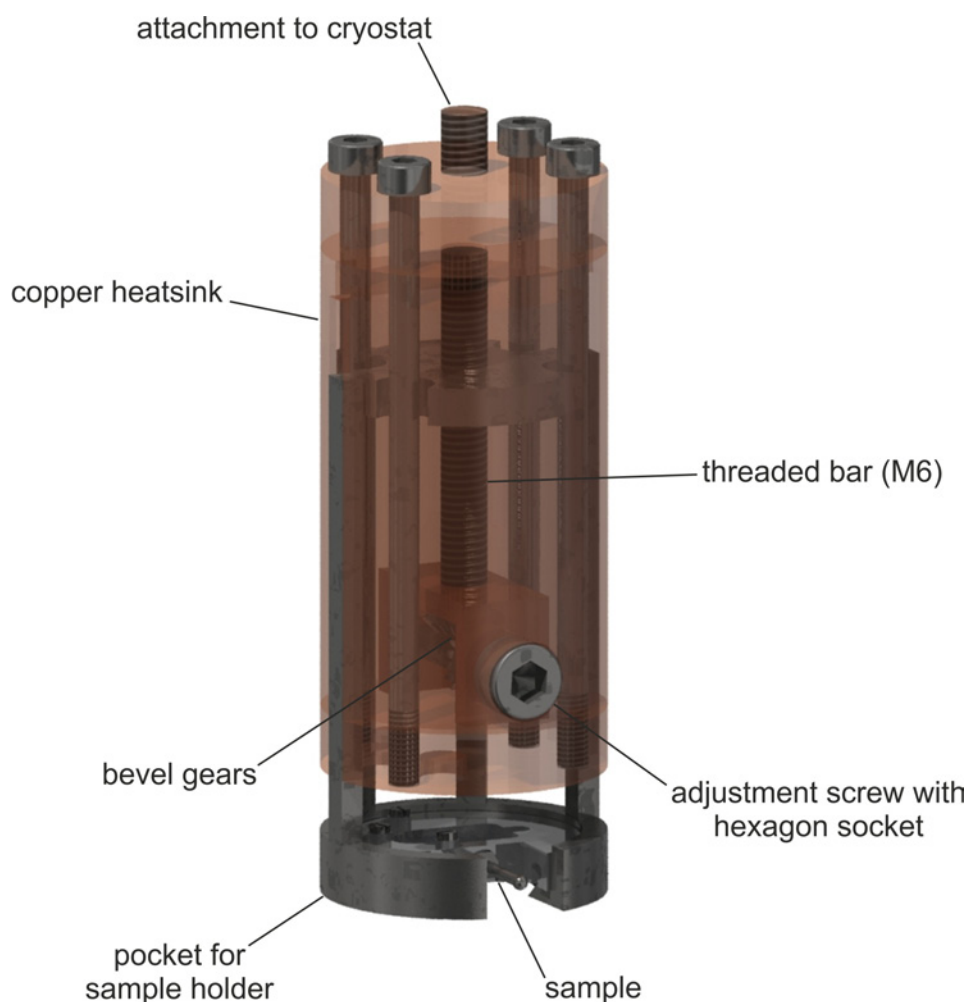


Figure 4.10: Contraction for mounting the sample to the cryostat. The sample can be lowered and elevated, thus establishing contact pressure with the copper heat sink, by using a UHV Allen key to turn the adjustment screw.

Another consideration regarding this construction was the heat transfer due to thermal radiation as this would be the dominating mechanism at large temperature differences with the environment according to the Stefan-Boltzmann law. Heat transfer due to conduction and convection are negligible which can be ascribed to the weak thermal coupling provided by the cryostat and UHV. Thermal radiation linearly depends on the emissivities of the sample mount surfaces which largely consist of slightly oxidized copper ( $\varepsilon \approx 0.76$ ). The surface area amounts to  $1.2 \cdot 10^{-4} \text{ m}^2$ . The radiation powers are plotted on the left hand side of figure 4.11 according to the Stefan-Boltzmann law as a function of temperature where the environmental temperature was assumed to be constant at 300 K. The blue curve applies for the slightly oxidized surface of the sample mount while the red curve would apply for polished gold surfaces ( $\varepsilon \approx 0.035$ ) which could be realized by coating or by using a thermoshield. The straight black line is a linear approximation of the specified refrigeration values represented by triangles. The intersection points correspond to the temperatures which can be achieved in the respective cases which is 30 K for oxidized copper and 1.8 K for polished gold. This shows that while the cryostat is being restricted to liquid nitrogen operation there is no limitation due thermal radiation even without the use of a thermoshield.

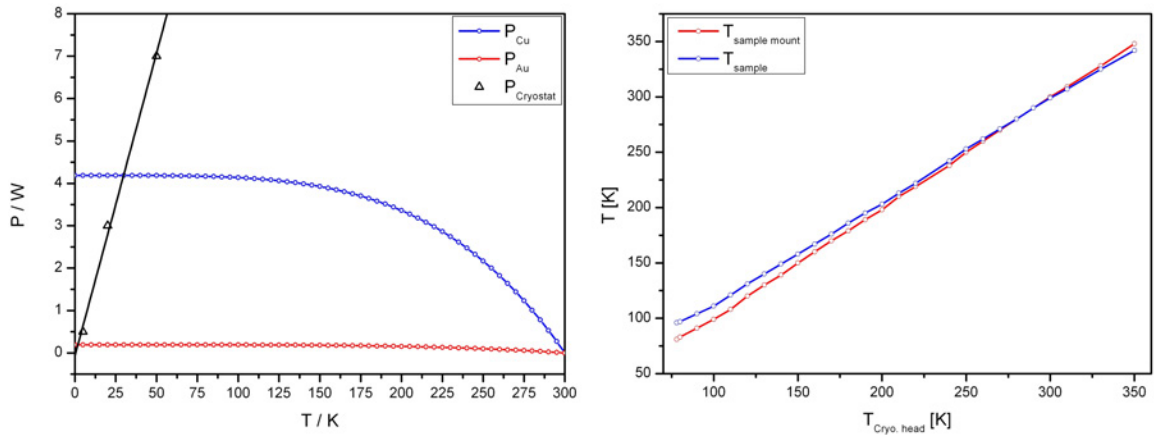


Figure 4.11: Left: Radiated powers from the sample mount for the cases of copper and gold surfaces as functions of the temperature. The black line linearly approximates the refrigeration values specified for the cryostat. The intersections indicate the temperatures that can be achieved with the respective surface materials. Right: Sample and sample mount temperatures as a function of the cryostat head temperature.

The right hand side of figure 4.11 shows the temperatures of the sample mount and the sample plotted versus the temperature of the cryostat head. A reproducible contact pressure could be realized by using a defined torque of 1 Nm on the adjustment screw. The values were recorded while heating up after cooling the cryostat head down to liquid nitrogen temperature. Thermal equilibrium at each point was established after a waiting

period of approximately 15 minutes. While the temperature of the sample mount basically corresponds to the temperature of the cryostat head the temperature of the sample deviates below 200 K reaching a minimum of 96 K.

### Sample alignment

The sample alignment, i. e. the orientation of the sample in a way that the reflected laser beam exits the MOKE chamber at the same spot regardless of the azimuthal orientation of the sample and the azimuthal orientation itself, is implemented by a port aligner (VACOM PA-35-H) and a bakeable differentially pumped rotary feedthrough (VAb DDF40p) (see figure 4.8). The port aligner basically consists of two DN38CF flanges linked by edge welded bellows with three interconnecting screws that act as a tripod. This permits an axial displacement of  $\pm 5$  mm and a polar angle adjustment of  $\pm 3^\circ$ . The use of a differentially pumped rotary feedthrough was inevitable because the cryostat itself needed to rotate according to the concept in which the sample mount is directly attached to the cryostat head. The rotary feedthrough which features a positioning accuracy of  $1^\circ$  has two pumping stages which have DN16CF connection flanges for access. The pumping stages, the UHV side and the side with atmospheric pressure are separated by two graphite impregnated Viton gaskets rotating on top of each other, respectively. The influx  $Q_{\text{in}}$  from atmospheric pressure is specified with  $10^{-5} \frac{\text{mbar}\ell}{\text{s}}$ . The attainable pressure is given by  $p_{\text{final}} = Q_{\text{in}}/S_{\text{eff}}$  where  $S_{\text{eff}}$  denotes the effective throughput of the pump given by  $S_{\text{eff}} = S/(1 + S/L)$  which is limited by the conductance  $L$  [Ber10]. An empirical formula for the determination of the conductance of a flange with a cross-sectional area  $q$  with laminar gas throughput is  $L = 1.16 \cdot 10^{-5} \frac{\ell}{\text{s}} \frac{q}{\text{m}^2}$ . Using the throughput of the main pump stand of  $67 \frac{\ell}{\text{s}}$  and the cross-sectional area of the DN16CF flanges of  $1.77 \cdot 10^{-4} \text{ m}^2$  the effective throughput amounts to  $15.4 \frac{\ell}{\text{s}}$  resulting in an attainable pressure of  $6.5 \cdot 10^{-7} \text{ mbar}$ . The same pressure would prevail in the second pump stage if both pump stages were connected. Assuming that the influx linearly scales with the pressure the influx from the pumping stages to the UHV side would amount to  $6.5 \cdot 10^{-14} \frac{\text{mbar}\ell}{\text{s}}$ . The analogous consideration for the ion getter pump results in an attainable pressure of  $3.6 \cdot 10^{-15} \text{ mbar}$  which is negligible compared to the base pressure of  $2 \cdot 10^{-10} \text{ mbar}$ .

### The MOKE setup

The basic MOKE setup was inherited from an foregoing work [Urb05] which in principle adopts the photoelastic modulation technique in combination with lock-in amplification described in [Vav00]. Figure 4.12 illustrates the optical part of the setup. A DPSS laser with a wavelength of 532 nm is used as a light source. Before being focussed onto the sample by a plano-convex lens ( $f = 300 \text{ mm}$ ) the light passes the polarizer which is oriented in a way to produce  $s$ -polarized light. Both the polarizer and the analyzer are Glan Thomson calcite polarizers (Thorlabs GTH10M) with an extinction ratio of  $10^5$ . The reflected light

first passes through a photo-elastic modulator (Hinds Instruments PEM-90) operating at a frequency of 50 kHz. The analyzer is rotated by approximately  $45^\circ$  with respect to the polarizer to maximize the amplitude of the modulated signal which is measured by the photo detector (Owis DT111).

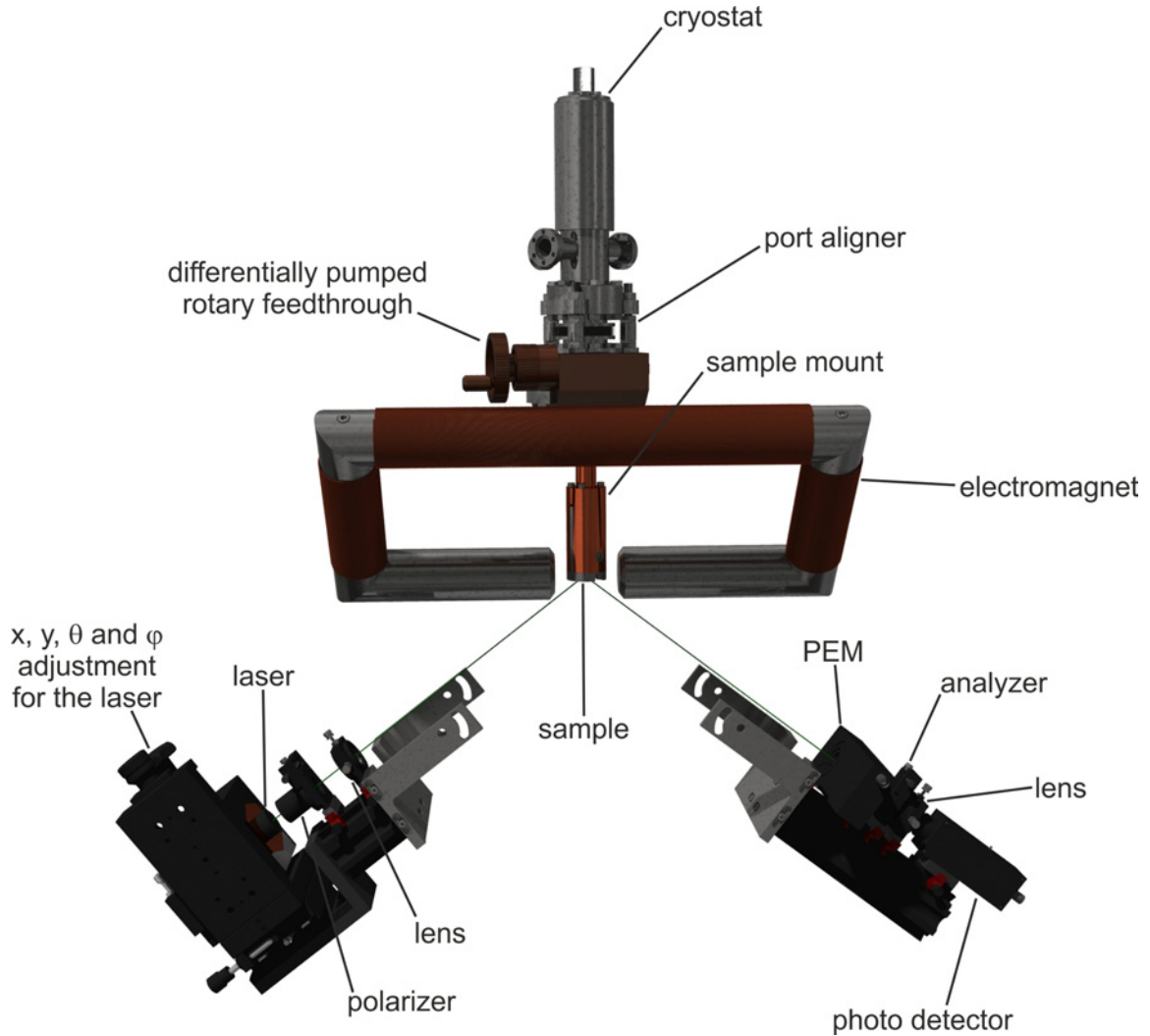


Figure 4.12: Schematic drawing of the UHV MOKE setup.

A diagram of connections among the MOKE components is depicted in figure 4.13. Signal input and output is done via a D/A converter (National Instruments PCI-6014) which is connected to the measurement computer running the MOKE software programmed in LabVIEW. One analogue output is used to control the unipolar power supply (HH-CM EA-PS 3032-20B) which provides the coil current for the electromagnet. The current then passes through a unit containing a relay which can switch the polarity. The magnetic field values against which the recorded hysteresis loops are plotted are acquired by the calibrated Hall sensors. As described above, the reflected light, the polarization of which

depends on the sample magnetization, first passes through the optical head of a photoelastic modulator. This is connected to the electronic head of the control unit which also provides a dual phase lock-in amplifier (Femto LIA-MVD-200-H) with the reference signal. The light, after passing the analyzer, is collected by the photo detector which is connected to the input of the lock-in amplifier. The time constant for lock-in amplification is usually set to 10 ms using a band pass with an edge steepness of 6 dB/Octave. The processed signal is then transferred to an analogue input of the D/A converter. To further increase the signal-to-noise ratio hysteresis curves are averaged over 20 to 100 loops depending on the signal strength.

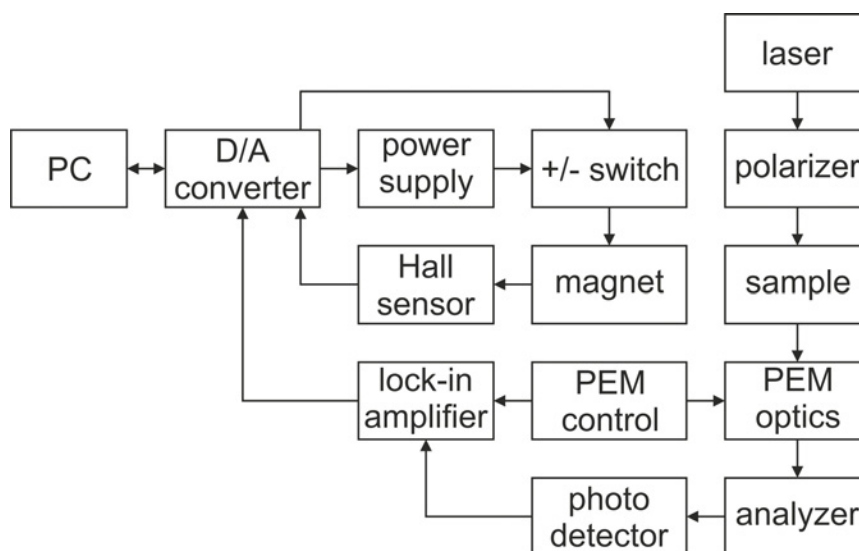


Figure 4.13: Diagram of the MOKE components and their connections.

### 4.3 Supplementary external setups

While the preceding sections described the main setup that was used for the in situ characterization of the samples additional data was obtained from measurements using external setups which shall be mentioned in this section.

In order to calibrate the MBE sources, corresponding layers were grown of which the thicknesses could be determined by small angle XRD measurements. For this, the 'Röntgen III' setup at the 'Institut für Experimentalphysik IV' was used which utilizes the  $\text{Cu K}_\alpha$  line ( $\lambda_{\text{CuK}_\alpha} = 0.1542 \text{ nm}$ ). Its primary filter is a Ni  $\beta$ -filter while a carbon single crystal is being employed as the secondary filter. The detector unit is a radiation-counter tube which can register up to  $5 \cdot 10^5$  counts/s. A detailed description of the setup can be found in [Bri97]. The composition of the deposited films including their capping layers was determined using Rutherford backscattering spectrometry (RBS). It was performed at the RUBION Dynamitron-Tandem-Laboratory of the University of Bochum using a singly charged  $^4\text{He}$

beam at an energy of 2 MeV with an intensity of about 20 nA. A silicon surface barrier detector was placed under a scattering angle of  $160^\circ$ . The spectra thus obtained were analyzed with the program RBX [Kot94]. The relevant layer constituents for the RBS analysis comprise Fe, Si, Ag and Au. The fact that both Fe and Si are lighter than the substrate elements Ga and As would cause the Fe and Si peaks to almost drop out when they coincide with the Ga and As continua. Hence, secondary MgO substrates on which the layers were deposited simultaneously to the primary substrates were used for the RBS analyses (see section 4.1.3). An example for a Rutherford backscattering spectrum obtained for a Au/Ag/Fe<sub>3</sub>Si/MgO sample is shown in figure 4.14.

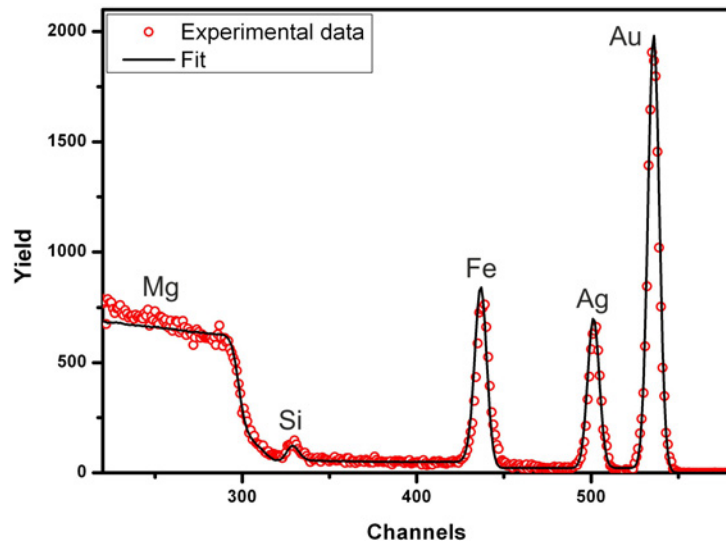


Figure 4.14: Spectrum of an Fe<sub>3</sub>Si/MgO sample capped with silver and gold as measured by RBS.

Where features of the surface morphology exceeded the scan range, scanning tunnelling microscopy was replaced by scanning electron microscopy (SEM). The apparatus used for these measurements, a FEI 'Quanta 200 FEG' employing an Everhart-Thornley detector, was provided by the 'Institut für Experimentalphysik IV' (University of Bochum). For more information about the SEM the reader is referred to [Bre11].

Also provided by the 'Lehrstuhl für Experimentalphysik IV' was the SQUID magnetometer (Quantum Design MPMS-XL) which was used for ex situ magnetic characterizations. It is an rf type SQUID magnetometer with magnetic fields up to 5 T, a resolution of  $10^{-11}$  Am<sup>2</sup> and a temperature range from 1.7 K to 400 K. Details about this setup can be found in [Now10].

The FMR data presented in this work were measured at a setup installed at the 'Center for Nanointegration (CeNIDE)' (University of Duisburg-Essen). It employs a cylindrical microwave cavity with a TE<sub>110</sub> eigenmode at a fixed frequency of 9.8 GHz. For the magnetic characterizations shown in this thesis, the external magnetic field was swept from 0 to 360 mT using a field modulation technique to increase the signal-to-noise ratio.

# Chapter 5

## Fe<sub>3</sub>Si/GaAs(001)

The first section of this chapter provides information about GaAs which constitutes the substrate material used in this work. Emphasis is laid on the various reconstructions of the (001) surface which occur as a result of different preparation methods. Following that is a section which is dedicated to the optimization of the Fe<sub>3</sub>Si layer morphology considering different growth parameters and post annealing. This will serve as the basis for all Fe<sub>3</sub>Si/GaAs(001) samples. The following two sections present an atomic scale structural analysis as well as a magnetic characterization of closed Fe<sub>3</sub>Si films. The structural and magnetic properties at low coverage which exhibit a fundamentally different behaviour will be described in section 5.5. The chapter concludes with a summary of structural and magnetic correlations that can be found for the system Fe<sub>3</sub>Si/GaAs(001).

### 5.1 GaAs and its (001) surface

The crystalline structure of bulk gallium arsenide (GaAs) is a zincblende lattice which can be considered as two fcc lattices that are shifted by  $\frac{\sqrt{3}}{4}a$  ( $a = 0.5653$  nm [Nag74]) along the [111] direction with respect to each other (see figure 5.1). The atomic bonds exhibit a tetrahedral arrangement due to the  $sp^3$  hybridization of the atomic orbitals. These bonds are mainly covalent but also have some ionic character which can be ascribed to the different electronegativities of Ga and As [Was05].

The (001) surface should ideally consist only of Ga or As atoms, thus being polar with two remaining dangling bonds per atom. Since this is energetically unfavourable and also because the stoichiometric ratios deviate from their ideal values caused by different binding energies of Ga and As, the GaAs(001) surface is always reconstructed. Predominantly depending on the temperature and the Ga/As flux ratios during MBE growth these reconstructions are numerous and can be reviewed in works like [Bie90], [Xue97] and [Ich01].

The specified reconstructions have the form  $(|\vec{a}^s|/|\vec{a}| \times |\vec{b}^s|/|\vec{b}|)$  according to Wood's notation, thus referring to the ratios of the base vectors of the surface and the bulk where  $\vec{a}$  and  $\vec{a}^s$  are parallel to  $[1\bar{1}0]$  and  $\vec{b}$  and  $\vec{b}^s$  are parallel to  $[110]$ . Table 5.1 lists the reconstructions

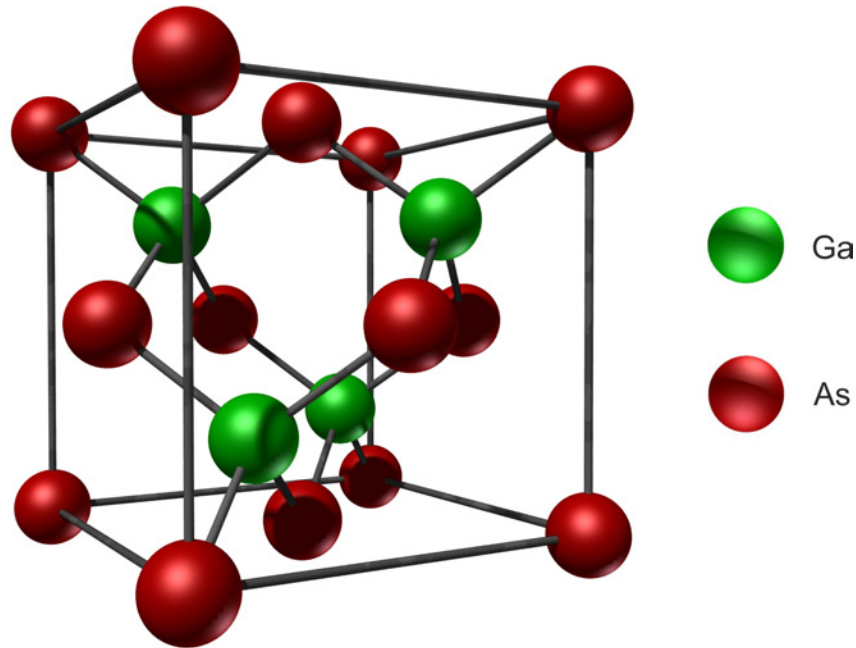


Figure 5.1: Zincblende structure of bulk GaAs.

and their corresponding models that are relevant to this work as they were encountered by LEED and STM analyses after the preparation of the substrates.

The GaAs(001) substrates used in this work were cut out from commercially available highly silicon-doped GaAs(001) wafers (Wafer Technology Ltd.) which have a thickness of  $(350 \pm 25) \mu\text{m}$ , a carrier concentration of approximately  $10^{18} \text{cm}^{-3}$  and a specific resistance of approximately  $2 \cdot 10^{-3} \Omega \text{cm}$ . High doping was essential to provide sufficient conductivity for STM and LEED measurements.

In order to obtain clean GaAs(001) surfaces on which the Fe<sub>3</sub>Si layers could be epitaxially grown, two types of substrate preparations were used which will be described in the following.

The first consists of cycles of ion-bombardment and annealing (IBA) where the ion bombardment was done by sputtering Ar<sup>+</sup> ions at an angle of 45° onto the sample using optimized parameters as they were determined in [Kne03]. During sputtering, Ar is let into the main chamber up to a pressure of  $10^{-4}$  mbar. Using a sputtering energy of 500 eV then yields ion currents in the range of  $2 \mu\text{A}$  to  $3 \mu\text{A}$  which, taking into account the ratio of the sample surface area and the area sputtered overall as well as the sputtering efficiency, corresponds to a removal rate of approximately  $0.3 \text{ML min}^{-1}$ . The ion bombardment procedure is done for 45 minutes which removes the native oxide layer and most impurities from the substrate surface but also leaves behind a rugged, partially disordered surface. The annealing procedure, which is also conducted for 45 minutes at temperatures between 500°C and 550°C using indirect heating as described in section 4.1.3, serves to flatten the

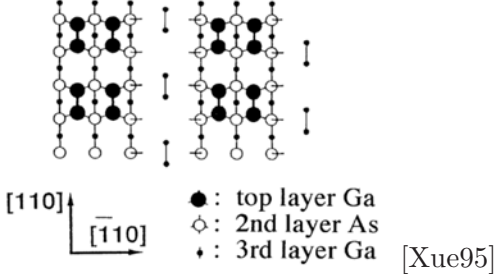
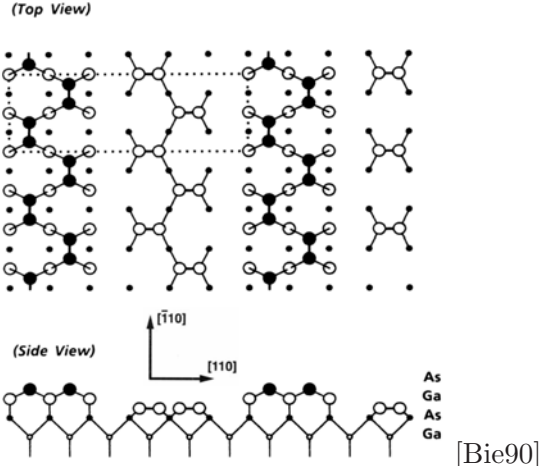
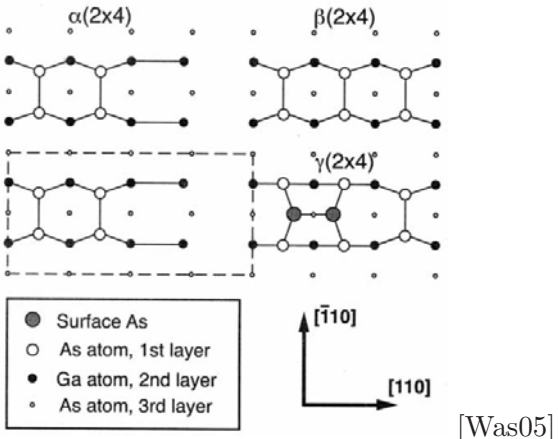
Reconstruction	Model
<p>(4 × 2) (Ga-rich)</p>	 <p>● : top layer Ga ○ : 2nd layer As ◐ : 3rd layer Ga [Xue95]</p>
<p>(2 × 6) (Ga-rich)</p>	<p>(Top View)</p>  <p>(Side View)</p> <p>As Ga As Ga [Bie90]</p>
<p>(2 × 4) (As-rich)</p>	 <p>● Surface As ○ As atom, 1st layer ● Ga atom, 2nd layer ○ As atom, 3rd layer [Was05]</p>

Table 5.1: Reconstructions of the GaAs(001) as they were observed by LEED and STM analyses and the corresponding models.

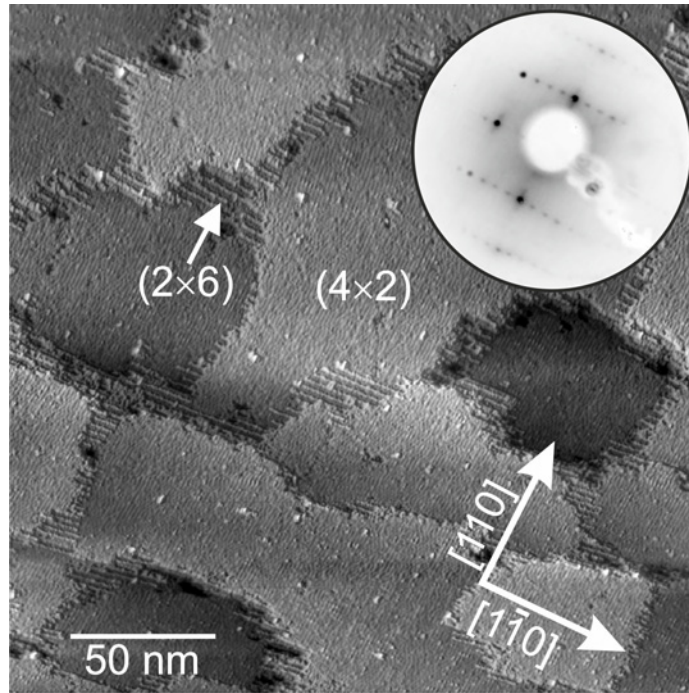


Figure 5.2: STM image of the GaAs(001) surface after several IBA cycles revealing the coexistence of  $(4 \times 2)$  and  $(2 \times 6)$  reconstructions ( $I = 1 \text{ nA}$ ,  $U = 2.3 \text{ V}$ ). The inset shows the corresponding LEED pattern ( $E = 125 \text{ eV}$ ).

substrate surface while restoring the crystalline structure at the same time. Typically, four to six IBA cycles are necessary to obtain an atomically flat substrate surface with small concentrations of impurities as shown in the STM image of figure 5.2. As already pointed out in [Ich01] and [Bie90], this type of preparation which requires high annealing temperatures leads to  $(4 \times 2)$  and  $(2 \times 6)$  reconstructions. This was confirmed by STM images and the corresponding linescans. Figure 5.2 shows that the  $(4 \times 2)$  and  $(2 \times 6)$  reconstructions are coexistent although, as measured for different substrates, the  $(2 \times 6)$  reconstruction only makes up  $(12 \pm 5) \%$  of the substrate surface. Accordingly, the LEED image shown in the inset of figure 5.2 shows a pseudo  $(4 \times 6)$  reconstruction, even if the spots which can be attributed to the  $(2 \times 6)$  reconstruction are barely visible.

The second type of substrate preparation makes use of GaAs(001) wafers that were provided with a GaAs buffer layer under As-rich conditions and capped with a 3 nm protective As layer in a III-V growth chamber at the 'Lehrstuhl für angewandte Festkörperphysik' (University of Bochum) before their transportation through air. The As capping layer is removed by a stepwise heating of the substrates up to a temperature of  $350 \text{ }^\circ\text{C}$  under the observation of the As partial pressure with the quadrupole mass analyzer. The duration of this procedure amounts to approximately 30 minutes. Figure 5.3 shows an STM image of the substrate surface obtained in that manner. The periodicities determined from STM

scans indicate a  $(2 \times 4)$  reconstruction which is corroborated by LEED patterns as shown in the inset of figure 5.3. This implies an As-rich surface according to table 5.1 where also the atomic model of this reconstruction is illustrated. The degree of purity can be estimated to be comparable to that of the substrate surfaces prepared by IBA cycles. Initially, the idea for the use of As-capped substrates was to save the time needed when using the method of IBA cycles which is effectively one or two days longer. However, it turned out that the As capping layer gradually degraded, thus requiring an increasing number of additional IBA cycles to provide useful substrates.

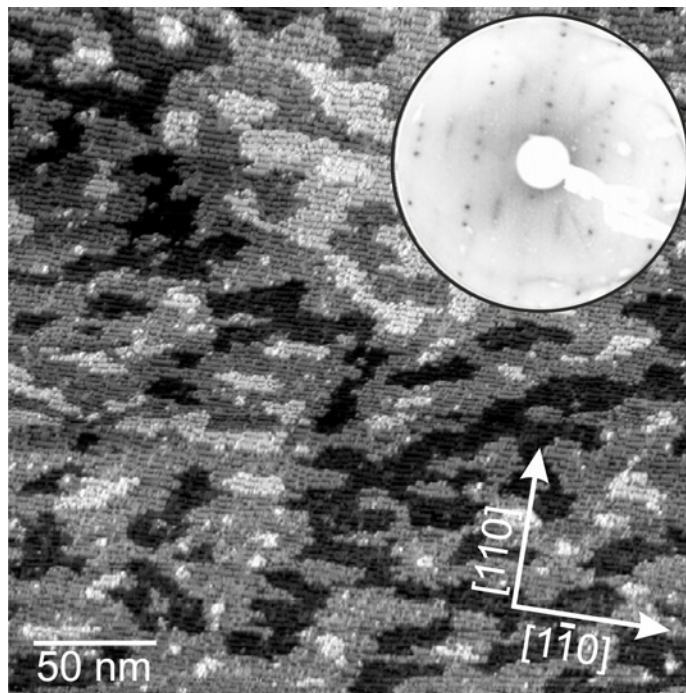


Figure 5.3: STM image of the  $(2 \times 4)$ -reconstructed As-rich GaAs(001) surface obtained after heating an As-capped substrate up to  $350^\circ\text{C}$  ( $I = 1\text{ nA}$ ,  $U = -3\text{ V}$ ). The corresponding LEED pattern ( $E = 95\text{ eV}$ ) is shown in the inset.

The experiments involving the structural and magnetic behaviour of  $\text{Fe}_3\text{Si}$  on GaAs(001) carried out in this work do not indicate any influence of the substrate reconstructions as in the case of  $\text{Fe}/\text{GaAs}(001)$  which is reviewed in [Was05]. However, especially in the range below 5 ML film thickness not enough data could be gathered to exclude such an effect which should intuitively exist especially upon nucleation due to the variations in number and arrangements of Ga and As atoms at the surface for different reconstructions.

## 5.2 Optimizing the layer morphology

As is already described in the framework of section 2.1, the underlying growth mode for Fe<sub>3</sub>Si on GaAs or, in other terms, the growth mode at thermal equilibrium due to surface energetic considerations is of the Volmer-Weber type. When moving away from thermal equilibrium by increasing the deposition rate a transition to a pseudo Frank-van der Merwe growth mode can be established above a certain thickness which has, however, not been observed by real space analyses up to now. Nevertheless, kinetic Monte Carlo simulations and the corresponding intensity oscillations shown in [Kag09] indicate that the optimal growth rates to achieve such a quasi layerwise growth lie in the range of  $0.014 \text{ nm min}^{-1}$  to  $0.14 \text{ nm min}^{-1}$  using a growth temperature of  $200^\circ\text{C}$ . At lower growth rates, in the case of which the system is closer to thermal equilibrium, the intensity oscillations calculated from the kinetic Monte Carlo data imply the formation of larger surface features and that trenches within the layer persist up to higher thicknesses. On the other hand, the growth rate needs to be kept low enough to avoid the effect of kinetic roughening.

Both this and the growth parameters found in other literature as reviewed in section 1.1 serve as the starting point for the growth of Fe<sub>3</sub>Si layers on GaAs(001). As such, a growth temperature of  $200^\circ\text{C}$  and a total deposition rate of  $0.1 \text{ nm min}^{-1}$  were chosen. As depicted in figure 4.8, the Si MBE source was oriented parallel to the surface normal of the substrate. The reason for this was not only the mechanical stability of the Si stack within the

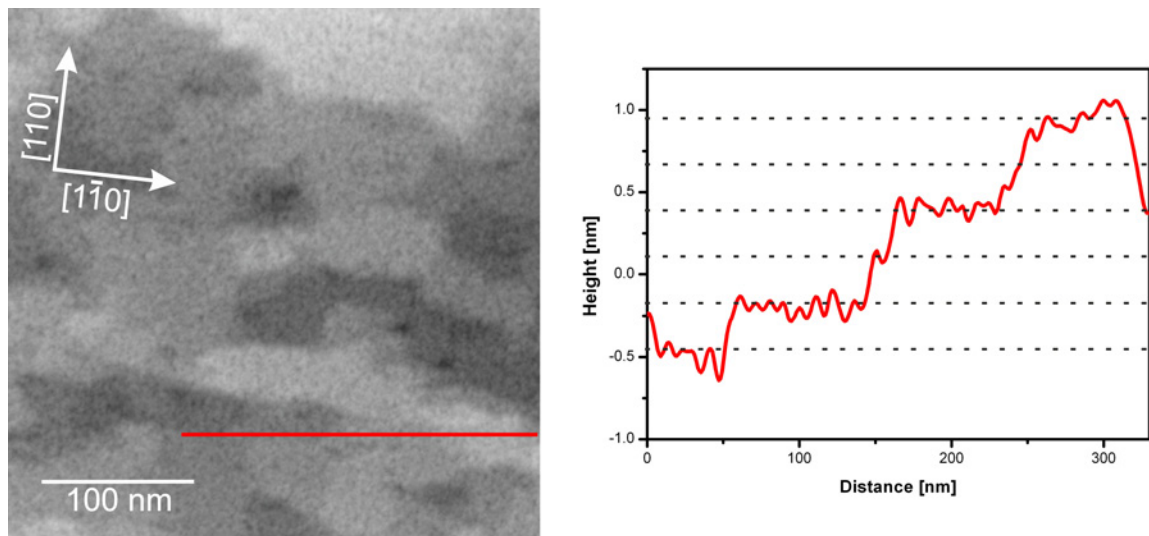


Figure 5.4: Left: Surface morphology after the deposition of 12 ML of Fe<sub>3</sub>Si on GaAs(001) as recorded by STM ( $I = 1.1 \text{ nA}$ ,  $U = 1.4 \text{ V}$ ). Terraces with edges oriented along the  $[1\bar{1}0]$  and  $[110]$  directions can be observed which are covered with unordered clusters. Right: The linescan obtained after low-passing the STM image illustrates the step heights of the terraces. The dashed lines are drawn as a guide to the eye.

electron beam evaporator but also to avoid inhomogeneities caused by shadowing effects which can occur during an oblique deposition of Si as observed in [Bar12]. The thickness as determined by RBS amounted to 12 monolayers which should be in the regime of a quasi layerwise growth. A closed film with almost layerwise growth should also serve for investigations on the atomic scale and the recipe thus obtained should be the basis for the growth of  $\text{Fe}_3\text{Si}/\text{GaAs}(001)$  at other thicknesses.

The left hand side of figure 5.4 shows an STM overview scan of a sample surface directly after growth where the above-mentioned growth parameters were used. Beneath randomly ordered clusters with diameters of  $(3.6 \pm 0.4)$  nm terraces can be recognized. Their edges show a tendency to be oriented along the  $[1\bar{1}0]$  and  $[110]$  directions. The STM line-scan on the right hand side points out the step heights of the  $\text{Fe}_3\text{Si}$  film which amount to  $(0.279 \pm 0.007)$  nm. The clusters covering the terraces cannot be resolved vertically due to their high density which inhibits the STM tip from reaching between them. At this point, a LEED pattern could not be found which can be ascribed to the unordered clusters covering the surface. As a result, using STM and LEED no statement can be made about the atomic ordering of the subjacent terraces.

Although the  $\text{Fe}_3\text{Si}$  layer shown in figure 5.4 can be considered as a closed film it is clear that the growth temperature cannot provide sufficient energy for atomic ordering at least at the film surface. Hence, the sample was stepwise post-annealed which would also allow

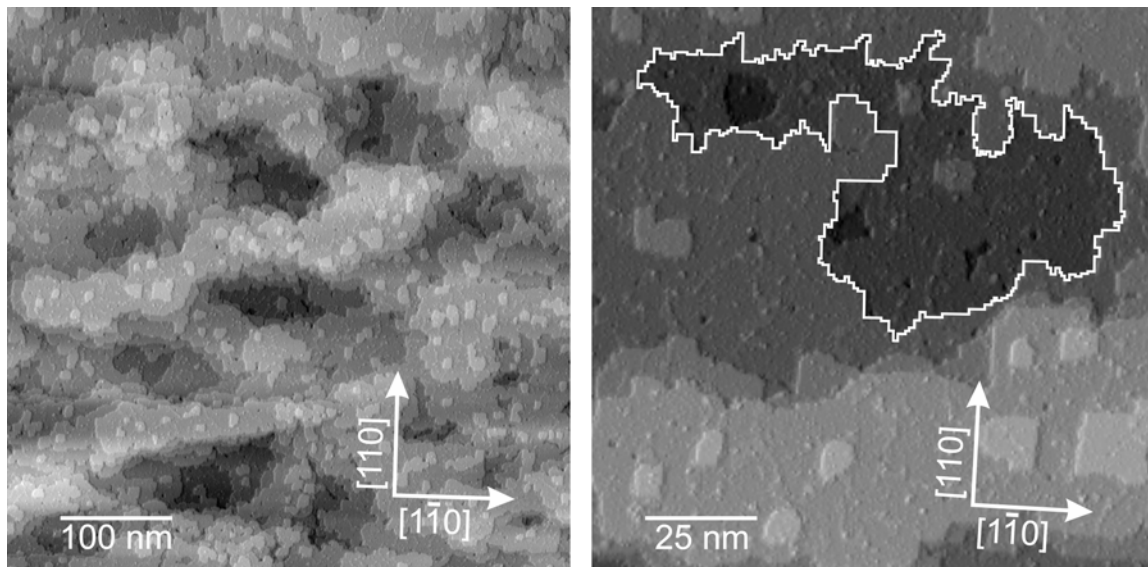


Figure 5.5: Left: STM overview scan ( $I = 1.2$  nA,  $U = 2.2$  V) of the same sample shown in figure 5.4 after post annealing at  $250^\circ\text{C}$  for 45 minutes. The surface appears to be significantly smoother after the disappearance of the unordered clusters. Right: A zoom-in of the same STM scan points out the orientation of the terrace edges along the  $\langle 110 \rangle$  directions which is emphasized by the hand-drawn border around one terrace.

the determination of the temperature dependence of the layer morphology.

After a subsequent post annealing at 250 °C for a duration of 45 minutes the film surface could be smoothed significantly as confirmed by the STM scans shown in figure 5.5. The STM images and henceforth all following STM images if not mentioned otherwise were enhanced using edge filtering. The diffusion energy was high enough for the unordered clusters to transform into atomically ordered terraces (corresponding STM images will be shown in section 5.3). The orientation of step edges along the  $\langle 110 \rangle$  directions has also become more pronounced which becomes even more apparent on a smaller scale as the right hand side of figure 5.5 illustrates. This is further emphasized by the hand-drawn perimeter around one of the terraces.

Further post-annealing was performed at 300 °C, again for a duration of 45 minutes. The resulting layer morphology imaged by STM can be seen on the left hand side of figure 5.6. While the overall smoothness of the film surface has increased with typical terrace widths of  $(100 \pm 20)$  nm, a more notable effect can be seen in the form of an increased orientation of the terrace edges which have also become more straight-lined. It appears that the energy provided by thermal treatment was sufficient for edge diffusion of the atomic species, thus minimizing the terrace perimeter. At the same time, the edge energy is reduced and further diffusion is inhibited according to equation 2.14 due to the increased number of nearest neighbours. The STM linescan shown on the right hand side illustrates a typical height

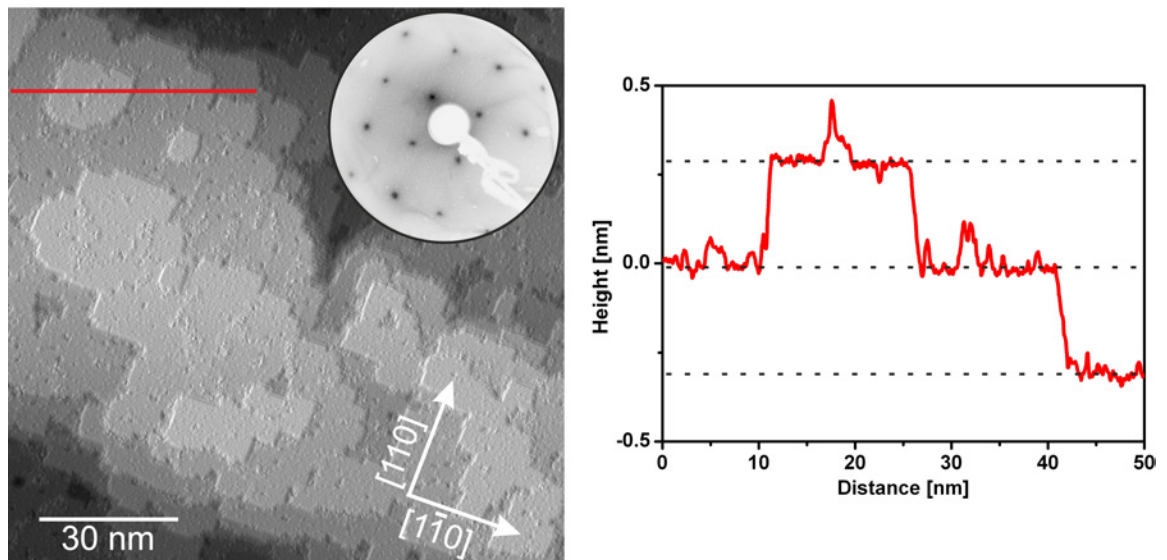


Figure 5.6: Left: Surface morphology after additional post-annealing of the sample shown in figure 5.5 at 300 °C for 45 minutes as measured by STM ( $I = 1.5$  nA,  $U = 1.9$  V). The inset shows the corresponding LEED pattern ( $E = 107$  eV) which can be associated with a square structure along the  $[1\bar{1}0]$  and  $[110]$  directions. Right: A linescan across several terraces after low-passing the STM image where again the dashed lines serve as a guide to the eye.

profile of the  $\text{Fe}_3\text{Si}$  film surface obtained in this way. The step heights are determined as  $(0.285 \pm 0.010)$  nm which is in good agreement with the bulk value of 0.282 nm [Ion05a]. The inset on the left hand side of figure 5.6 shows the photographically captured corresponding LEED pattern where an electron energy of 107 eV was employed. The pattern can be associated with a square atomic structure with an edge orientation along the  $\langle 110 \rangle$  directions or with a face-centred structure with respect to the  $\langle 100 \rangle$  direction. Considering the well-known epitaxial relation  $(001)[110]\text{GaAs}|| (001)[110]\text{Fe}_3\text{Si}$  [Her04], the LEED pattern is in accordance with the  $\text{D0}_3$  structure of  $\text{Fe}_3\text{Si}$ . Also, the distances between the diffraction spots of  $\text{Fe}_3\text{Si}$  are equal to those associated with the unreconstructed  $\text{GaAs}(001)$  surface which complies with the fact that substrate and adsorbate are almost lattice-matched.

The surface morphology was furthermore analyzed after post-annealing at  $400^\circ\text{C}$  for another 45 minutes. The STM image on the left hand side of figure 5.7 shows the incipient break-up of the  $\text{Fe}_3\text{Si}$  layer after this thermal treatment. The straightening of the terrace edges along the  $[1\bar{1}0]$  and the  $[110]$  directions is found to be reversed. In contrast to a predominantly convex morphology which is observable after post annealing at  $250^\circ\text{C}$  (see figure 5.5) a generally concave impression is conveyed. This is most likely to be attributed to the onset of substrate exposure which in turn can be ascribed to the underlying non-wetting Volmer-Weber growth mode or to the onset of an alloying between the  $\text{GaAs}$  substrate and the  $\text{Fe}_3\text{Si}$  layer. Thermal treatment at this stage also evokes a new feature in the form of trenches within the film which again have edges that are strictly oriented along the  $\langle 110 \rangle$  directions. The appearance of such rectangular-shaped holes with lateral sizes of about

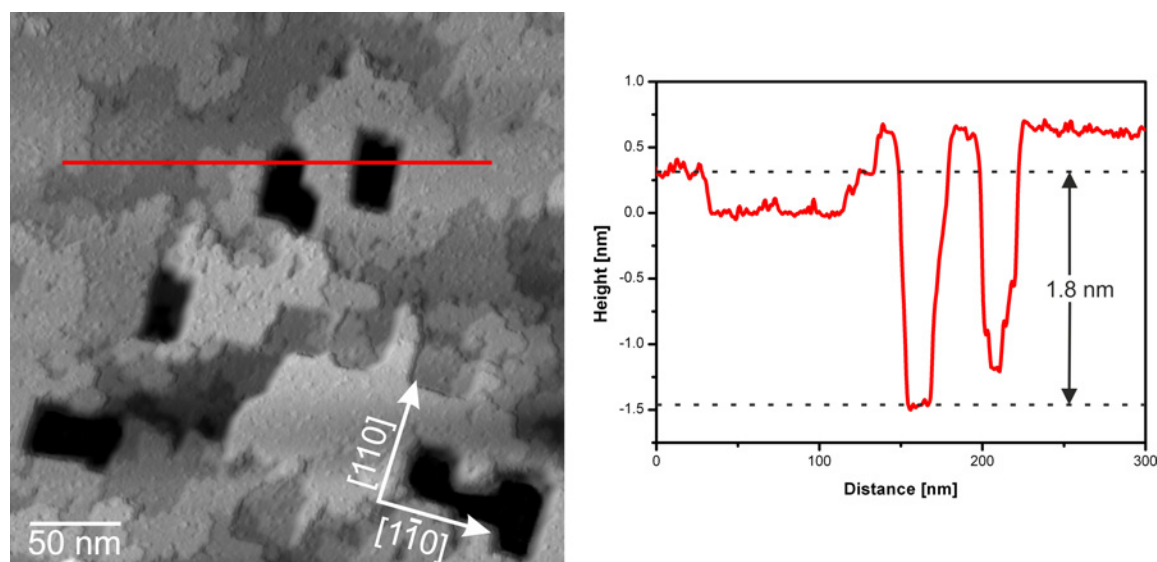


Figure 5.7: Left: STM image ( $I = 0.8\text{ nA}$ ,  $U = 1.4\text{ V}$ ) after further post-annealing at  $400^\circ\text{C}$  shows the incipient breakup of the layer. Terrace edges become less oriented and the formation of cavities can be observed. Right: Linescan across several terraces and a pair of cavities.

1  $\mu\text{m}$  after rapid thermal annealing at 500 °C was already reported in [Her05] although the corresponding AFM image was not shown there. The right hand side of figure 5.7 shows an STM linescan across a pair of such trenches. With respect to the average surface height a depth of 1.8 nm was measured which corresponds to approximately 6 monolayers of Fe<sub>3</sub>Si which clearly deviates from the film thickness of 12 monolayers. Hence, at this point of the post annealing series, the trenches do not yet seem to reach the substrate level. However, a certain reduction in the measured depth of the trenches might occur due to a finite thickness of the STM tip or multitips. Moreover, it is questionable whether the surface morphology obtained after the above mentioned post annealing duration represents an equilibrium state as STM scans do not create that impression.

A final post-annealing of the sample was done at 500 °C, again for a duration of 45 minutes. As shown in figure 5.8, this led to a fundamental alteration of the surface morphology. The image on the left hand side is an STM overview scan which reveals a 'melting' of the terrace edges. Also, the trenches observed after post annealing at 400 °C turned into larger cavities which resulted in unstable tunnelling conditions during the STM scans. Therefore, and also due to the fact that the lateral dimensions of the cavities extended into the  $\mu\text{m}$  regime, additional larger-scale scans were done ex situ by SEM. Although this would entail a possible oxidization of the sample, the use of the typical Ag and Au capping was refrained in order to influence the surface morphology as little as possible. Cavity-free regions which

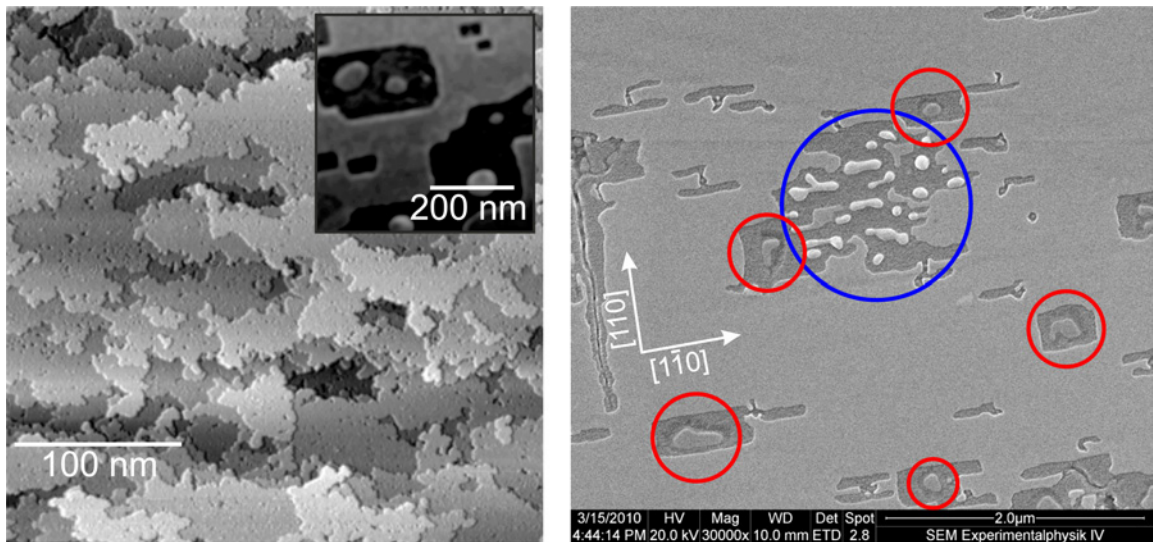


Figure 5.8: Left: Overview STM scan ( $I = 0.7 \text{ nA}$ ,  $U = 2.3 \text{ V}$ ) obtained after final post-annealing at 500 °C for 45 minutes. The terrace edges have lost their orientation. The inset is meant to illustrate that SEM images of the same surface can also, even though at the resolution limit, visualize some of the terrace levels. Right: The same sample surface as measured by SEM detecting secondary electrons. The red and blue circles indicate regions where different types of alloys between the Fe<sub>3</sub>Si layer and the substrate can be found.

could still be imaged by STM clearly exhibit a number of terraces. Due to the fact that the contrast measured by SEM when detecting secondary electrons, which is the mode with the highest lateral resolution, mainly depends on the chemical composition and on edge effects, different terrace levels would appear as homogeneous areas. However, by applying a Gaussian filter and by contrast-boosting as shown in the inset on the left hand side of figure 5.8, terraces can faintly be visualized also by SEM. This can be explained by considering that the Fe<sub>3</sub>Si film is thin enough for the substrate to contribute to the secondary electron yield and by considering that the GaAs substrate and the Fe<sub>3</sub>Si film have different secondary electron yields. Edge effects do not seem to have a large contribution which can be ascribed to the fact that they only have heights in the monolayer regime. The SEM image on the right hand side of figure 5.8 reveals that within the cavities which are found to have diameters ranging from 20 nm to 1 μm different types of islands occur which are marked by red and blue circles. The first type, marked by red circles, is surrounded by narrow trenches with different grey scales while the second type within the blue circles appears brighter and it is located in larger cavities. These islands are likely to be alloys between the GaAs substrate and the Fe<sub>3</sub>Si film. As shown in [Her05] after rapid thermal annealing at 575 °C DCXRD rocking scans exhibit a peak that is most likely to be attributed to an Fe<sub>2</sub>As reflection which can be assigned to one of the types of islands seen here. Furthermore, from the growth of Fe on GaAs the formation of the ternary alloy Fe<sub>3</sub>Ga<sub>2-x</sub>As<sub>x</sub> is known to be formed already after post annealing at 370 °C [God08].

From this series of surface morphologies obtained directly after growth ( $T_G = 200$  °C) and the different steps of post-annealing the respective RMS roughnesses  $R_{\text{rms}}$  were determined from the STM and SEM data using

$$R_{\text{rms}} = \sqrt{\frac{1}{MN} \sum_{m=1}^M \sum_{n=1}^N (h(x_m, y_n) - \langle h \rangle)^2}. \quad (5.1)$$

Here,  $h(x_m, y_n)$  are the heights in a region consisting of  $M \times N$  pixels and  $\langle h \rangle$  is the average height in that region. The resulting plot is depicted in figure 5.9 where the values along the dashed line were determined from cavity-free surface regions while the values along the solid line included the cavities in a representative amount. The RMS roughnesses were averaged several times over areas of  $(100 \text{ nm})^2$ . The  $y$ -error bars represent statistical errors of the RMS roughness and the  $x$ -error bars take into account an estimated measuring accuracy of the pyrometer of  $\pm 10$  °C. As the STM images already suggest a significant reduction of the roughness of approximately 30% could be achieved after the post-annealing steps at 250 °C and 300 °C due to the coalescence of the clusters that were initially unordered and unconnected directly after the growth. The dashed line indicates that at higher post-annealing temperatures the roughness could locally still be reduced although the overall roughness increases again due to the formation of cavities within the Fe<sub>3</sub>Si film.

In summary, the optimum result in terms of a closed layer with maximum smoothness can be obtained after post-annealing at a temperature of approximately 300 °C. Compared to

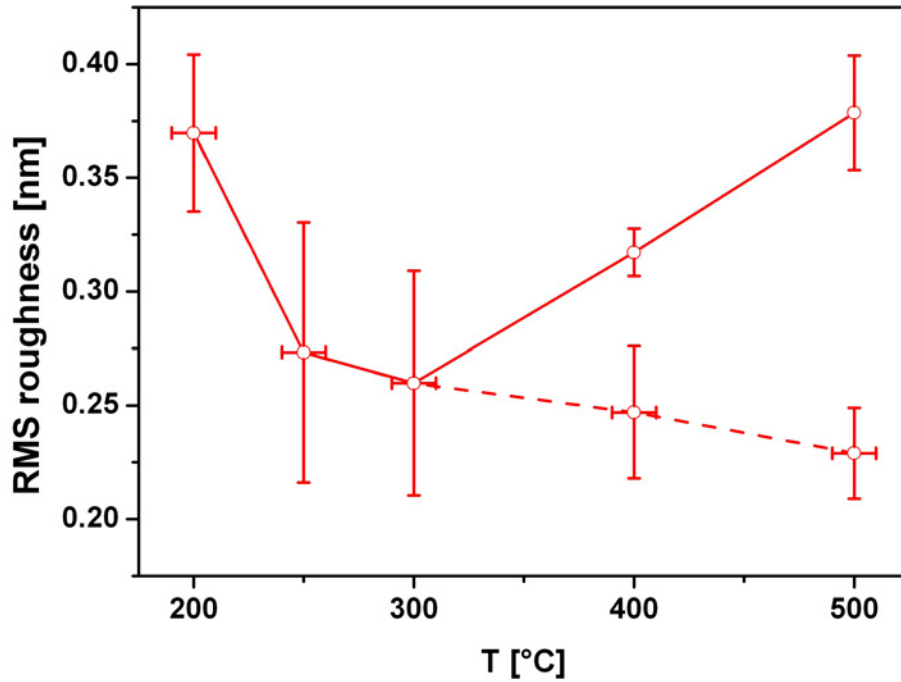


Figure 5.9: RMS roughnesses as a function of the post annealing temperatures. The roughnesses at 400 °C and 500 °C connected by the dashed red lines were measured in areas without cavities.

a previous study where the RMS roughness as measured by AFM directly after the growth ( $T_G \approx 200$  °C) was determined as 0.4 nm [Her03], which is within the range of the error bar at 200 °C in figure 5.9, the post-annealing procedure used here can reduce the roughness down to  $(0.26 \pm 0.05)$  nm. Higher temperatures at around 400 °C lead to the breaking-up of the Fe<sub>3</sub>Si film and eventually to the formation of alloys between the substrate and the adsorbate at around 500 °C. In this temperature range it is also known that the structural homogeneity degrades and that alloys start to form [Her05] where Fe<sub>2</sub>As as an antiferromagnet [Kat66] would lead to the reduction of the magnetic moment at the interface. The dendritic structure of terrace edges with lateral dimensions of 3 nm as observed by AFM in [Jen07] could not be confirmed at any stage. These features might, however, be attributed to the deposition of an additional monolayer of Fe<sub>3</sub>Si during an annealing at 310 °C in that study.

At this point it should be mentioned that the morphology similar to the one obtained here after post-annealing at 250 °C could be observed on some samples directly after growth. It appears that the coalescence of the clusters in the topmost layer takes place at  $\gtrsim 200$  °C. The observed variations can be explained by measuring accuracy of the pyrometer or by the temperature fluctuations due to the thermal radiation of the MBE sources onto the sample during growth.

Nevertheless, an optimized layer morphology cannot be attained in a one-step process as

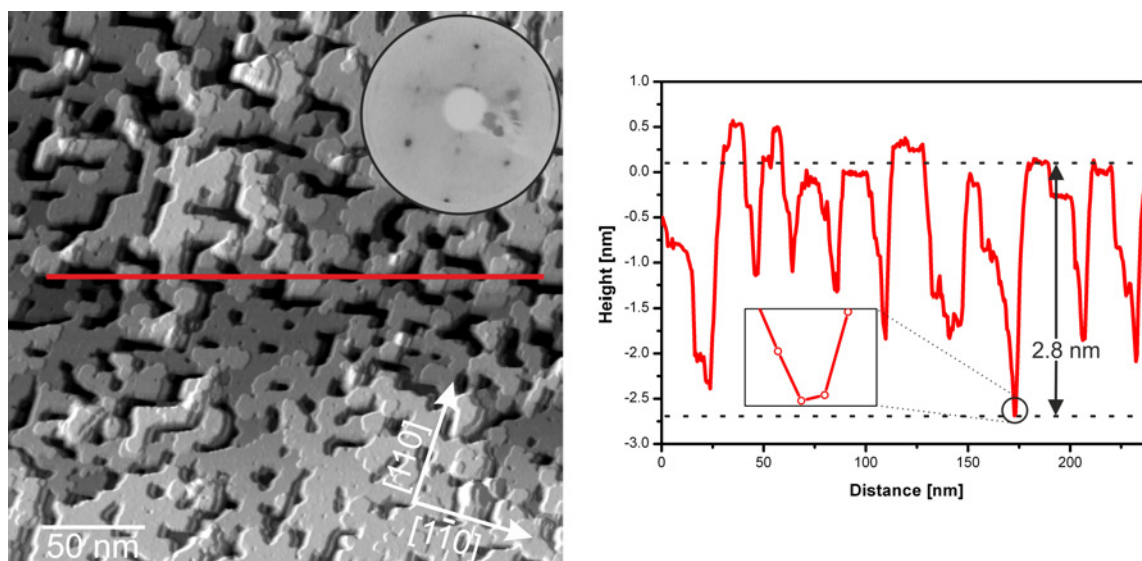


Figure 5.10: Left: Overview STM scan of 13 ML  $\text{Fe}_3\text{Si}$  on  $\text{GaAs}(001)$  after the deposition using a growth temperature of  $250^\circ\text{C}$  revealing deep trenches within the  $\text{Fe}_3\text{Si}$  layer ( $I = 0.2 \text{ nA}$ ,  $U = 2.2 \text{ V}$ ). The inset shows the corresponding LEED pattern ( $E = 48 \text{ eV}$ ). Right: Height profile across several terraces and trenches as obtained from STM data.

illustrated in figure 5.10. The growth parameters for this sample were the same only with an elevated growth temperature of  $250^\circ\text{C}$  instead of the previous  $200^\circ\text{C}$  and a slightly increased film thickness of 13 ML instead of 12 ML as determined by RBS. Higher thicknesses should in fact favour the growth of a closed film which, when looking at the STM overview scan on the left hand side of figure 5.10, is not the case. Unlike the surface morphology directly after the growth at  $200^\circ\text{C}$  the observed terraces are atomically flat but the presence of deep trenches creates the impression of a terrace network rather than that of closed layers. The vertical spacing between adjacent terrace levels amounts to  $(0.290 \pm 0.012) \text{ nm}$  as measured from STM linescans which is still in agreement with the height of one monolayer of  $\text{Fe}_3\text{Si}$ . Also, the strongest spots in the LEED pattern at the considered energy relate to the  $\text{D0}_3$  structure. Besides that, also weaker spots can be observed which correspond to the  $(4 \times 2)$  reconstructed substrate surface. This indicates that the trenches in the  $\text{Fe}_3\text{Si}$  film indeed reach down to the substrate surface level. From STM linescans such as the one shown on the right hand side of figure 5.10 this cannot clearly be seen. The dashed lines represent the average level of the terrace surfaces and the deepest position measurable by the STM tip. Their distance amounts to  $2.8 \text{ nm}$  or approximately 10 ML of  $\text{Fe}_3\text{Si}$  which is less than the film thickness. On the other hand it also becomes clear from the narrow dips in the linescan which only consists of one or two pixels as shown in the inset with the magnified linescan that the STM tip is too thick to 'reach down' into the trenches.

As described in section 2.1 the growth kinetics depend on an interplay between deposition rate and diffusion where the latter depends on the growth temperature. Basically, higher

deposition rates result in a higher density of nucleated clusters whereas higher temperatures correspond to a step towards the conditions at thermal equilibrium. For a system like Fe<sub>3</sub>Si/GaAs(001) where upward jumps of mobile species from the substrate onto the adsorbate layers are favoured this would lead to the exposure of the substrate surface. It cannot be ruled out that the observed growth behaviour at an elevated temperature can be countered by an increased deposition rate. However, for the given experimental conditions, i. e. the distance between MBE sources and sample and the achievable rates especially of the Si electron beam evaporator, substantially higher effective deposition rates could not be reached. Therefore, the samples were prepared using the above described optimized parameters.

### 5.3 Atomic scale analysis

Scanning tunnelling microscopy was used in order to investigate the atomic structure of the Fe<sub>3</sub>Si surface. It is expected that the electronic structure of the D0<sub>3</sub> sublattices has a notable influence on the information that can be gathered by STM. Therefore, the experimental data will be compared with STM simulations that were provided by Benjamin Geisler from the 'Center for Nanointegration (CeNIDE)' (University of Duisburg-Essen). Further emphasis is laid on the study of defects and to assign them to the disorder at the top two monolayers previously determined from CTR analyses of XRD measurements [Kag08].

#### 5.3.1 The atomic structure

In figure 5.11 an STM overview scan revealing both the surface morphology with the typical terraces structures obtained after post-annealing at 300 °C as described in the previous section but also the atomic structure is depicted. The inset illustrates that the atomic structure is a face-centred lattice with respect to the [100] and [010] directions. The lattice constant determined from STM linescans amounts to  $(0.570 \pm 0.020)$  nm which is in good agreement with the lattice constant of bulk Fe<sub>3</sub>Si of 0.5642 nm at stoichiometry. However, it becomes apparent that only one sublattice of the D0<sub>3</sub> structure is being imaged by STM. Previous works have shown both experimentally [Kag08] and theoretically [Haf07] that the surface of Fe<sub>3</sub>Si is mixed terminated. Thus remains the question whether the Fe or the Si sublattice is visualized in the STM scans.

In order to gather more information about the electronic structure dual voltage images were recorded during which every line was scanned twice with different bias voltages. Asymmetries in the local densities of states for different sublattices would make themselves notable by different positions of the different atomic species. An exemplary dual voltage STM scan is shown on the left hand side of figure 5.12 where the left half is an empty state image

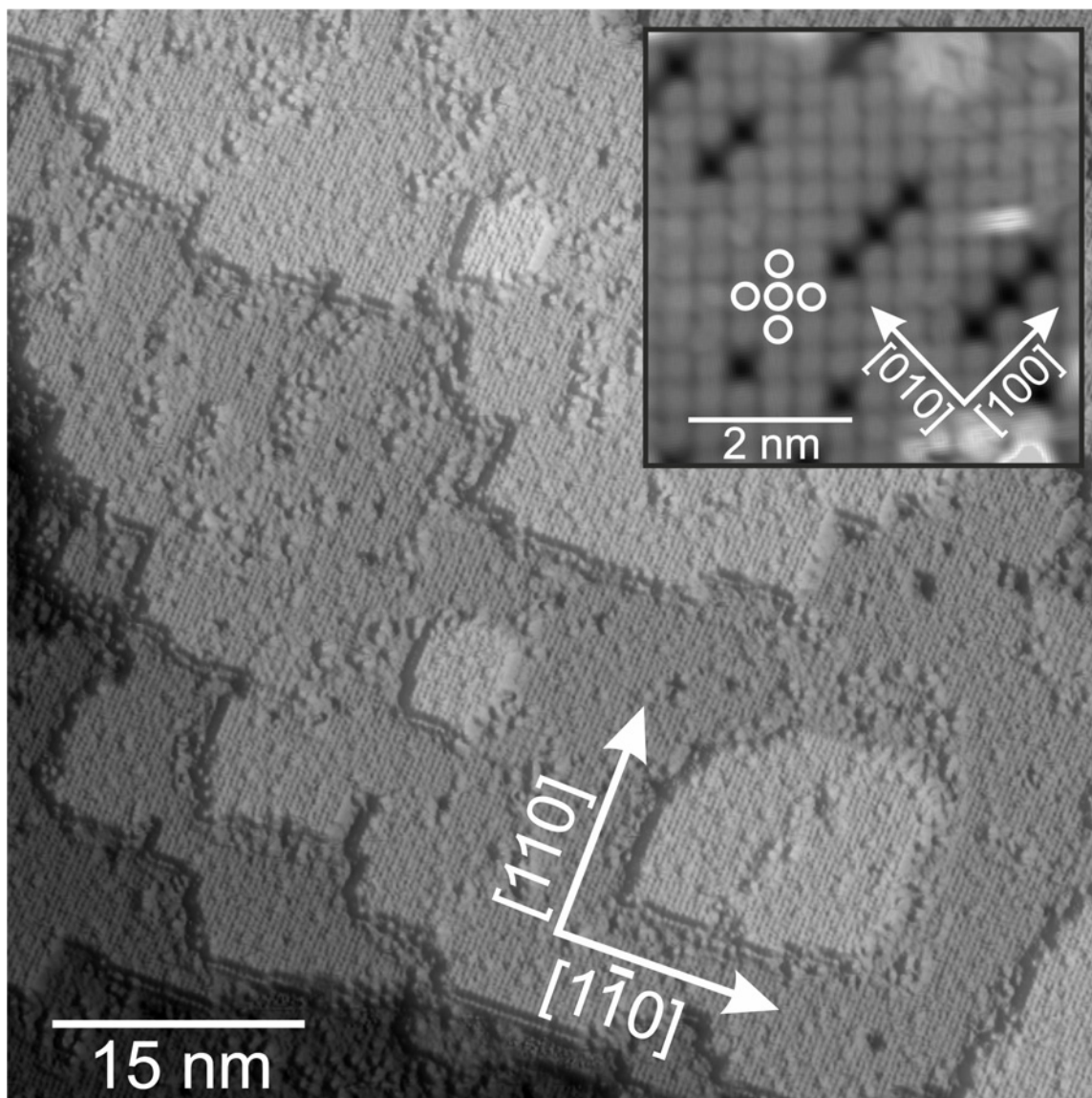


Figure 5.11: Atomic resolution STM scan ( $I = 1.5 \text{ nA}$ ,  $U = 1.9 \text{ V}$ ) of 12 ML  $\text{Fe}_3\text{Si}/\text{GaAs}(001)$ . The inset shows a zoom-in on the atomic structure revealing a face-centred lattice with respect to the  $\langle 100 \rangle$  directions.

measured at a bias voltage of 1.9 V and the right half is a filled state image measured at a bias voltage of -1.7 V. This illustration was obtained by superimposing the two scans and by removing one half of one of the scans up to the dashed line. In order to prevent a possible falsification of atomic positions, edge filtering was refrained from which also applies for the following representations of atomic scale STM images. No significant offset can be observed between the imaged sublattices. Thermal drifts or piezo creeps which could counter an offset can also be excluded as they would have to be in the order of  $100 \text{ nm min}^{-1}$  considering a scanning speed of  $0.164 \text{ s/line}$  that was used for these images.

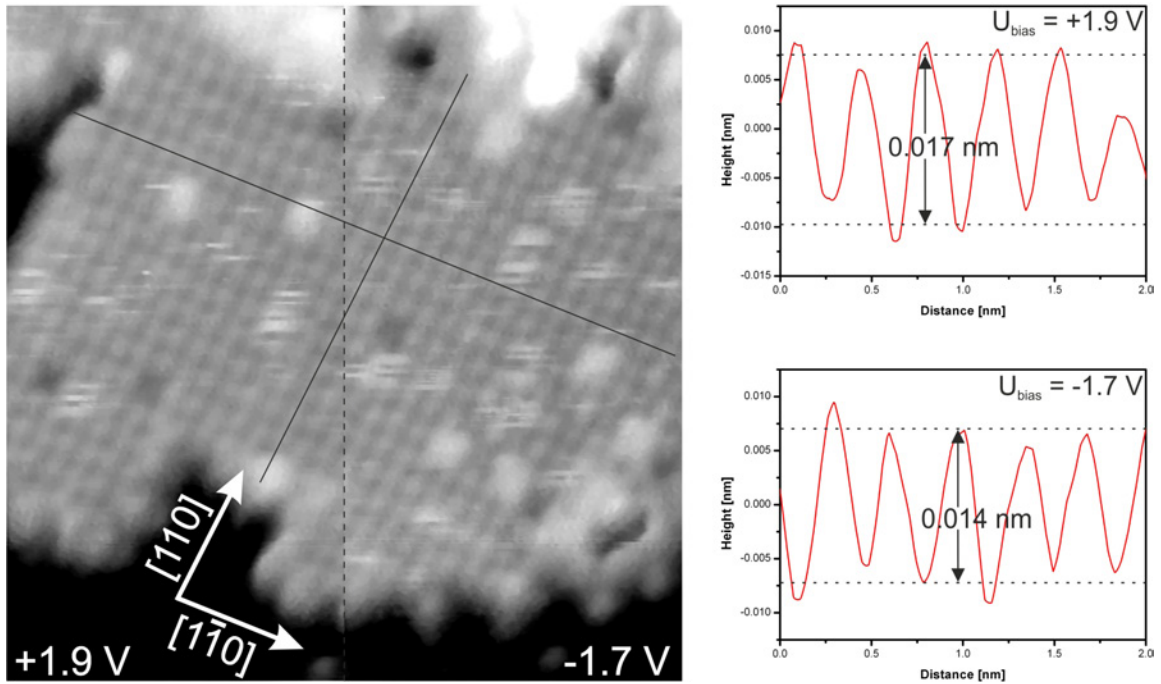


Figure 5.12: Left: Dual voltage STM scan ( $I = 1.5 \text{ nA}$ ) with bias voltages of  $1.9 \text{ V}$  imaging empty states (left part) and  $-1.7 \text{ V}$  imaging filled states (right part) where the images have been superimposed upon which one of the images has been removed up to the dashed line. The thin solid lines are drawn along the atomic rows in the  $[1\bar{1}0]$  and  $[110]$  directions. Right: The line scans illustrate the contrast given by the distances between the dashed lines for both cases.

Moreover, the sample should have been very close to thermal equilibrium with the scanning unit of the STM as the last annealing step was completed at least 120 minutes before and several scans were done at the same position thus avoiding piezo movements on a larger scale. The experimental data points out that always one and the same sublattice is visible in empty and filled state images. For comparison, STM simulations on the basis of DFT calculations are being considered. Figure 5.13 illustrates both empty and filled state images for a Fe-Si-terminated surface. Models of the atomic structure can be seen on the lower left corners of the upper two images indicating the positions of the sublattices with respect to the simulated STM images. Si and Fe(B) atoms of the top layer are yellow and bright red in colour, respectively. Fe(A,C) atoms of the subjacent layer are brown in colour. In contrast to the experimental STM data with comparable bias voltages, the simulated STM images yield a contrast inversion for filled state images at  $-1.5 \text{ V}$  and empty state images at  $1.5 \text{ V}$ . In the filled state case atoms of the Si sublattice are visible with a contrast of approximately  $0.03 \text{ nm}$  to the background. These Si atoms disappear in favour of atoms of the Fe(B) sublattice in the empty state case. Here, the contrast between the Fe(B) atoms and the background amounts to about  $0.01 \text{ nm}$ . The contrast obtained from experimental data as shown on the right hand side of figure 5.12 amounts to approximately  $0.014 \text{ nm}$

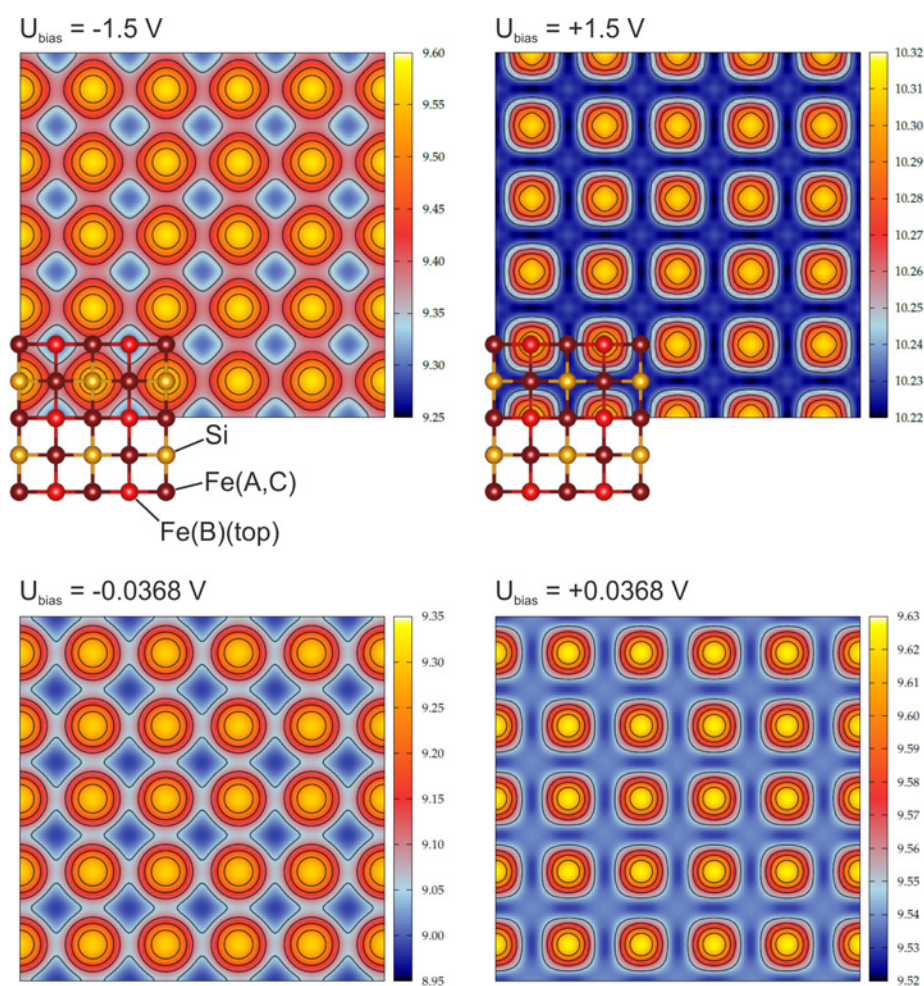


Figure 5.13: STM simulations for the Fe-Si-terminated  $\text{Fe}_3\text{Si}$  surface obtained from DFT calculations provided by B. Geisler (University of Duisburg-Essen). The position of the different sublattices are indicated on the lower left corners of the upper images. The images on the left hand side represent filled state images for bias voltages of  $-1.5\text{ V}$  and  $-0.0386\text{ V}$  while those on the right hand side represent empty state images for bias voltages of  $1.5\text{ V}$  and  $0.0386\text{ V}$ . Units of the height scales are given in  $\text{\AA}$ .

in the filled state case and  $0.017\text{ nm}$  in the empty state case, thus being almost unaffected upon inverting the bias voltage. Both the experimental and the theoretical contrast are, however, of the same order. The contrast inversion found in the simulations persists down to  $U_{\text{bias}} \lesssim 0.05\text{ V}$ . The lower two images in figure 5.13 are simulated filled and empty state images for bias voltages of  $-0.0386\text{ V}$  and  $0.0386\text{ V}$ , respectively. Here, a contrast inversion can, indeed, not be found as in both cases atoms of the Si sublattice are visible.

The question arises what might be the reason for the discrepancies between the theoretical results and the experimental data. If the effective potential difference between the STM tip and the sample does not correspond to the set bias voltage and is in fact reduced by

a voltage drop at some other point the experimental situation would correspond to the simulations at low voltages. However, this voltage drop would have to be considerable reducing the bias voltage by about 50 times. Also, the contrasts in the simulations at low bias voltages change considerably by approximately a factor of 4; an effect that is not observable in the experiments. Another explanation could be that in the experiment it is actually neither an iron nor a silicon sublattice that is imaged but a segregation of e. g. As onto the Fe<sub>3</sub>Si growth front with a  $(1 \times 1)$  reconstruction at the surface. A similar effect has been observed for the growth of Fe/ZnSe(001) where Se moves at the growth front and forms a  $(2 \times 2)$  reconstruction on the Fe surface [Mar04]. It should also be mentioned that the observed lattice constant would be in agreement with a  $c(2 \times 2)$  reconstruction of Si at the surface on top of a stabilizing CsCl structure of the iron silicide as described in [Bus97]. However, as already mentioned in section 1.1, this structure would only be formed at a temperature of 880 K which is well above the post-annealing temperature. Therefore, the latter theory is rejected for the following considerations.

### 5.3.2 Defects

As mentioned before, a previous study based on XRD measurements [Kag08] has determined the top two monolayers of an Fe<sub>3</sub>Si film to be disordered with order parameters<sup>1</sup> of  $\alpha = 0.15$  and  $\beta = 0.5$ . This section provides a real space analysis using atomic scale STM data to identify this disorder in the form of surface defects.

#### Antisite defects

One part of the disorder manifests itself in the form of antisite defects as illustrated in the STM scan shown in figure 5.14. In order to sustain the atomic contrast across several terraces a cyclic grey scale presentation was used. Drawn into the inset is a model of the two sublattices of the Fe-Si terminated surface of the Fe<sub>3</sub>Si film. In view of the conclusion of section 5.3.1 these sublattices are not assigned to Fe and Si for the time being but shall be referred to as the visible and the non-visible sublattice which shall serve as the basis for the following discussion. The two fundamental types of antisite defects can be seen in the inset where two representative specimen are indicated by dotted black and white crosslines. In the first case an additional visible protrusion is located interstitially between four atoms of the visible sublattice. This can be interpreted as atoms of the visible sublattice taking on sites in the otherwise non-visible sublattice. Alternatively, this could be atoms, both of the visible or the non-visible type, in the next higher layer. However, the data suggests that this is rather not the case as the atoms would not be exactly interstitially located which corresponds to a shift of  $(\frac{a}{2}, 0, 0)$  but shifted by  $(\frac{a\sqrt{2}}{4}, -\frac{a\sqrt{2}}{4}, \frac{a}{4})$ . The second type of antisite defects of which an example is marked by the dotted black crosslines in the inset

<sup>1</sup>The order parameter  $\alpha$  describes the fraction of Si atoms occupying Fe(B) sites and vice versa while the order parameter  $\beta$  describes the exchange of atoms between the Si and the Fe(A,C) sublattices

consist of either missing species in the visible sublattice or their replacement by non-visible species.

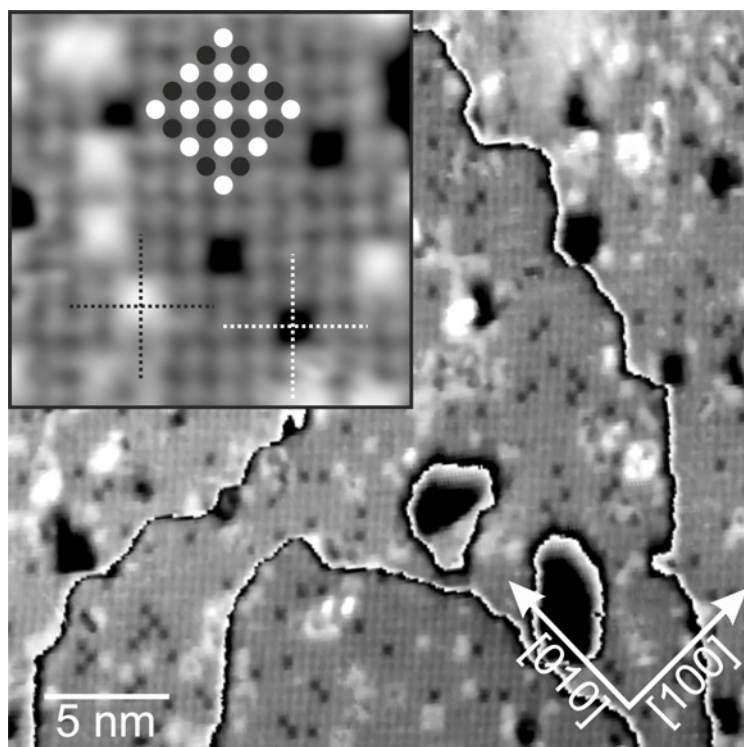


Figure 5.14: An atomic scale STM scan ( $I = 1.5 \text{ nA}$ ,  $U = 2.1 \text{ V}$ ) illustrating different kinds of antisite defects. A cyclic grey scale was used to enhance the atomic contrast across several terraces. The inset is a zoom-in showing a model of the two sublattices contained in a Fe-Si terminated surface of  $\text{Fe}_3\text{Si}$  and pointing out the exact locations of the antisite defects.

### Faulted stacking sequences

The other type of defect which has a larger contribution to the disorder can sometimes be observed in the form of faulted stacking sequences which causes whole terraces to be shifted from their regular positions. The models drawn in figure 5.15 illustrates both regular and faulted stacking sequences of  $\text{Fe}_3\text{Si}$ . Basically, the model with the faulted stacking sequence emerges when the third sublattice of the  $\text{D0}_3$  structure shifted by  $(\frac{a}{2}, \frac{a}{2}, \frac{a}{2})$  from the Fe(B) sublattice is not a silicon but again an iron sublattice. As a result, the  $\text{D0}_3$  structure is replaced by bcc Fe and B2 Fe-Si unit cells where the latter is the CsCl type. This is shown in the upper right 3D model in figure 5.15. A consequence of the  $\text{D0}_3$  structure is that atomic rows of one species along the  $\langle 110 \rangle$  direction are shifted causing them to lie exactly between two atomic rows of the same species in the adjacent layers as shown in the lower left hand side top view of figure 5.15. The top view on the lower right hand side illustrates that this is not the case for faulted stacking sequences.

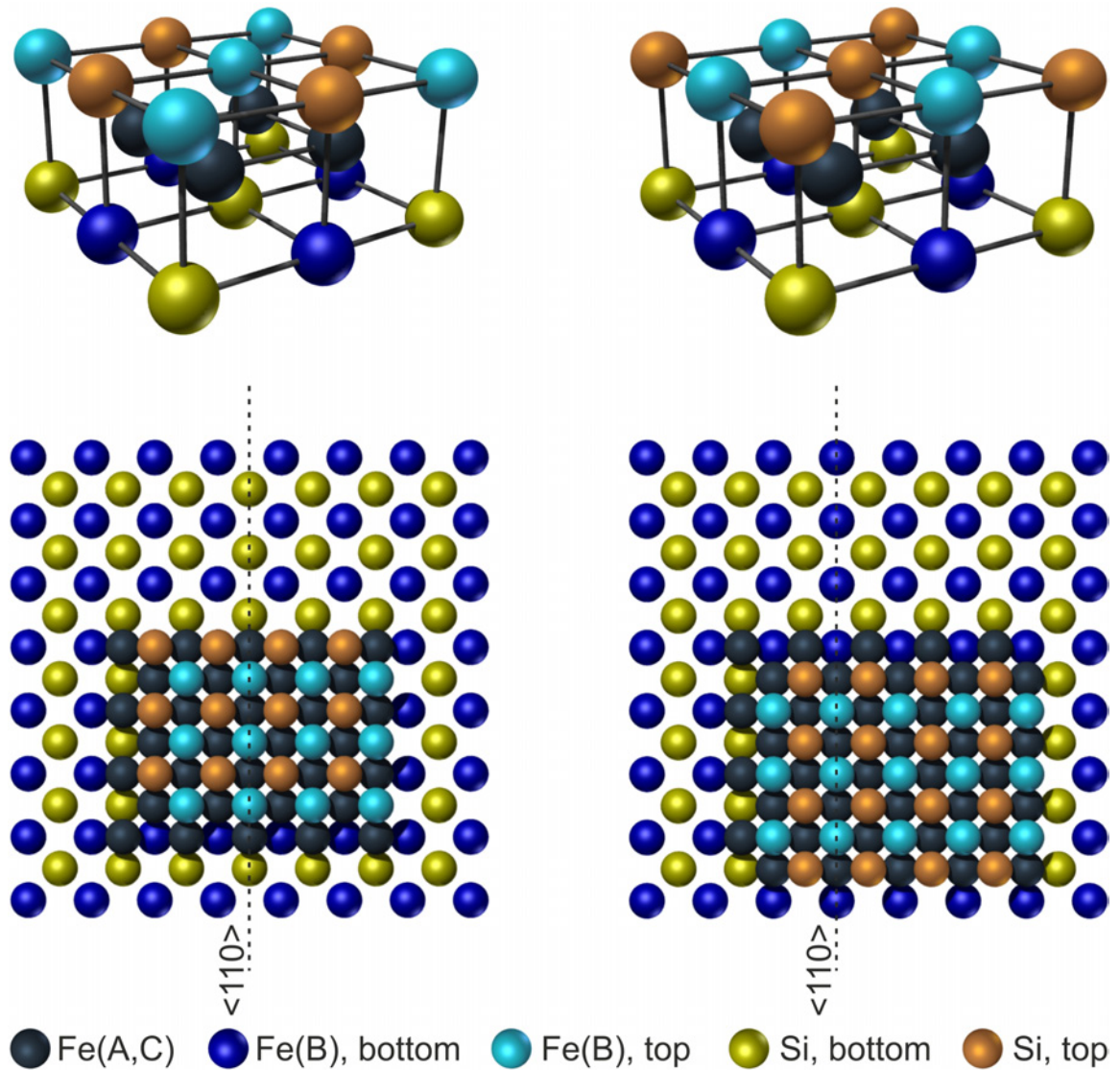


Figure 5.15: Models of the regular (left) and faulted (right) stacking sequences that can occur during the epitaxial growth of  $\text{Fe}_3\text{Si}$ . The 3D views on top illustrate the different resulting unit cells while the top views illustrate the shifting of atomic rows between adjacent layers in the case of regular stacking which cannot be observed of faulted stacking sequences.

The stacking sequences have been investigated experimentally on the basis of atomic scale STM images such as those shown in figure 5.16 where again a cyclic grey scale was used in order to enhance the atomic contrast across several terrace levels. The dashed lines in the STM image on the left hand side indicate two examples for regular stacking sequences. Here, the above-mentioned shift of the atomic rows, in this case by  $\frac{\sqrt{2}}{4}a$  along the  $[1\bar{1}0]$  direction occurs from one terrace level to the next. The STM image on the right hand is dominated by faulted sequences between the two terrace levels shown there. This is indicated by the dashed line which lies exactly between two atomic rows on the adjacent terrace levels.

Moreover, this image shows that shifts can also be found within one layer as indicated by the dotted line which implies the existence of in plane antiphase boundaries where the lattice is shifted within one terrace level. It should be mentioned that sometimes small additional offsets can be observed which make the assignment of the stacking sequences difficult. As discussed in [Özk11], this may be due to the fact that the sample surface and the scanning plane are not parallel. However, the maximum lateral displacement arising therefrom as determined from the inclination angles found in the STM linescans amounts to approximately 0.01 nm which corresponds to only 5 % of the shift that should be observed for regular stacking sequences. The additional displacement might also be attributed to tip switches. From the evaluation of different steps of adjacent terrace levels in several STM images it can be concluded that the regular and faulted stacking sequences occur with probabilities of approximately 50 %, respectively.

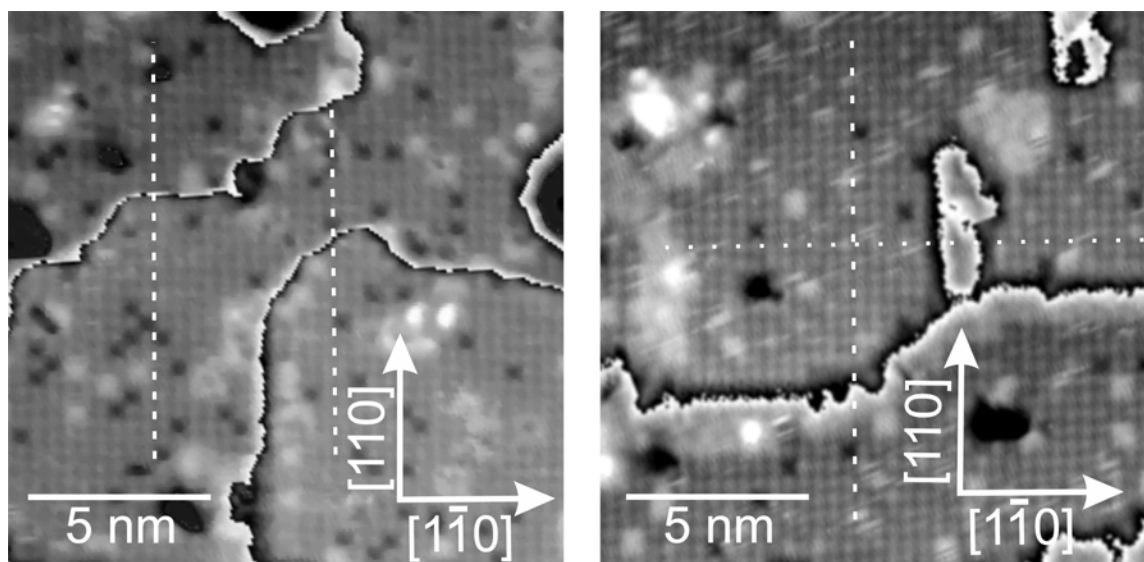


Figure 5.16: STM images using a cyclic grey scale representation of regular and faulted stacking sequences ( $I = 1.5$  nA,  $U = -2.1$  V). Left: Examples for regular stacking sequences. Right: An example of a faulted stacking sequence from one terrace to the next. Also, an antiphase boundary is shown where the shift of the sublattice occurs within one terrace.

In summary, the STM data reveal that two types of defects contribute to the disorder previously deduced from XRD measurements. The isolated antisite defects are estimated to make up  $(9 \pm 3)$  % of the surfaces where variations could be observed for several samples. Although all considered samples have a silicon content of  $(23 \pm 2)$  at.% where the error can mainly be attributed to the resolution of RBS, samples which tend to have a higher Si deficiency also tend to have a greater amount of antisite defects. Since the majority of the observed antisite defects consist of the type where atoms of the visible species are either missing or being replaced by the non-visible species this could be a hint that it is the

Si sublattice which is imaged by STM to continue the discussion from section 5.3. While the antisite defects can contribute to both order parameters, although only interchanges between the Si and the Fe(B) sublattice can be observed by STM under the assumption of an Fe-Si termination, faulted stacking sequences constitute the largest portion of the defects. Since the faulted stacking sequence can be understood as the complete interchange between Si and Fe(B) atoms for a large area, it makes up a considerable amount of the order parameter  $\alpha$ .

## 5.4 Magnetic behaviour of closed Fe<sub>3</sub>Si films

Presented in this section is a multitechnique experimental study of the magnetic behaviour of Fe<sub>3</sub>Si films epitaxially grown on GaAs(001) the structural properties of which were subject of the previous sections. While the UHV MOKE setup was used for in situ characterization, additional information, such as the thickness dependences of magnetic moments, anisotropy fields and anisotropy constants could be obtained by using ex situ SQUID magnetometry and FMR.

### 5.4.1 In situ characterization

In plane angular dependent longitudinal MOKE measurements were used for an in situ characterization of the samples directly after the MBE growth of Fe<sub>3</sub>Si. This allowed an analysis of the magnetic behaviour before the deposition of silver and gold protective layers but also the study of a possible influence of these protective layers. Furthermore, by the integration of a cryostat in the course of the modifications of the experimental setup as described in section 4.2.2 it was now possible to perform the MOKE measurements at low temperatures.

### Selected hysteresis loops and anisotropy plots

As already mentioned in section 1.1, the main contributions to the magnetic anisotropy are made by the magnetocrystalline anisotropy which has easy axes along the  $\langle 100 \rangle$  directions and the uniaxial magnetic anisotropy. By means of angular dependent in situ MOKE measurements which yield hysteresis loops and, as done here, anisotropy plots on the basis of the angular dependent remanent magnetization  $M_r$ , the interplay of these anisotropies can be investigated for samples with different growth parameters, especially the film thickness. In analogy to the structural investigations, the first sample considered here consists of 12 ML Fe<sub>3</sub>Si co-deposited on GaAs(001) where a growth temperature of 200 °C and post annealing at 300 °C for 45 minutes was used. Figure 5.17 shows hysteresis loops measured along prominent crystallographic directions, namely the  $[110]$ , the  $[100]$  and the  $[1\bar{1}0]$  directions. In order to obtain these and the following hysteresis loops measured by MOKE, quadratic contributions due to QMOKE but also possibly to the Voigt effect were separated

and subtracted as shown in section 3.3. In this thickness range it becomes apparent that the magnetic anisotropy is dominated by a uniaxial anisotropy with an easy axis along the  $[1\bar{1}0]$  direction. The  $[100]$  direction, which is the easy axis of the magnetocrystalline anisotropy, becomes an intermediate axis in this case. In contrast to the remanent magnetizations the coercive fields are isotropic amounting to 0.5 mT which is a typical value for highly ordered Fe<sub>3</sub>Si.

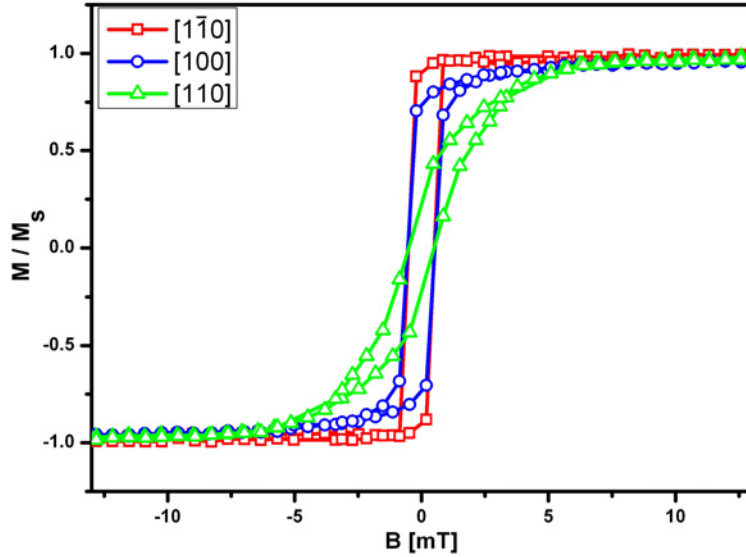


Figure 5.17: Hysteresis loops for selected crystallographic directions of 12 ML Fe<sub>3</sub>Si/GaAs(001) deposited at  $T_G = 200^\circ\text{C}$  and post-annealed at  $300^\circ\text{C}$  as measured by in situ MOKE.

According to [Her08], the direction of the uniaxial anisotropy in the case of Fe<sub>3</sub>Si/GaAs(001) depends on the layer thickness  $d$  in a way that it can be decomposed into a volume and an interface term:

$$K_u^{\text{eff}} = K_u^{\text{vol}} + K_u^{\text{int}}/d \quad (5.2)$$

This equation illustrates that the condition for a reorientation of the UMA is that  $K_u^{\text{vol}}$  and  $K_u^{\text{int}}$  have opposite signs. A more detailed discussion of this topic including the results in literature and the experimental findings within the scope of this work will be part of section 5.4.3. In addition to the thickness dependence, by comparing the results shown in [Her08] and [Len05] the direction of the UMA also seems to have a dependence on the growth temperature with a reorientation from the  $[110]$  towards the  $[1\bar{1}0]$  direction with increasing  $T_G$  in the range of  $200^\circ\text{C}$  to  $250^\circ\text{C}$ . Despite a growth temperature of  $200^\circ\text{C}$  which in these terms can be considered as low, the UMA of the sample considered here lies along the  $[1\bar{1}0]$  direction. It appears that post annealing at  $300^\circ\text{C}$  has the same effect as an increased growth temperature.

For comparison, another sample with a significantly higher film thickness of 60 ML Fe<sub>3</sub>Si but otherwise identical growth parameters within the limits of the measurements accuracies

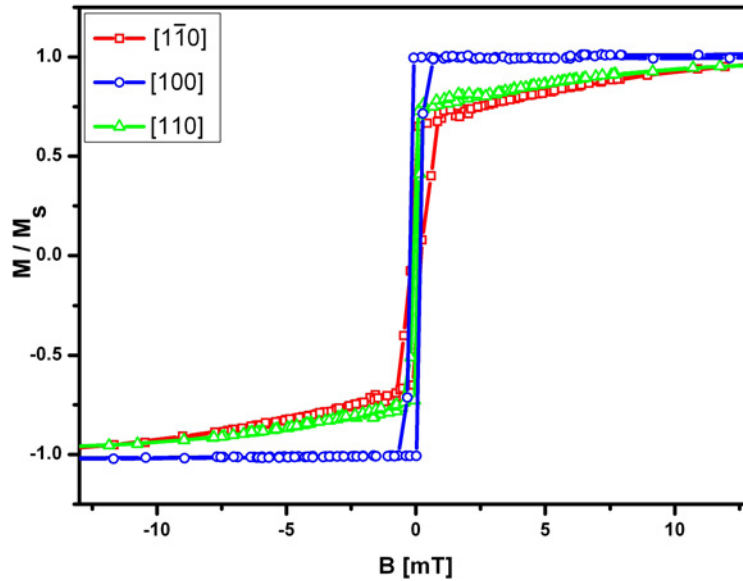


Figure 5.18: In situ MOKE Hysteresis loops for selected crystallographic directions of 60 ML Fe<sub>3</sub>Si/GaAs(001) grown at 200 °C and post-annealed at 300 °C.

is considered. Figure 5.18 shows hysteresis loops measured along the same crystallographic directions as in the previous case. At this higher film thickness the  $[100]$  becomes the easy axis while the  $[110]$  and the  $[1\bar{1}0]$  directions are intermediate axes. A closer look reveals that there is still some contribution from the uniaxial magnetic anisotropy which, however, now favours the  $[110]$  direction. Like for the sample with the thinner Fe<sub>3</sub>Si layer, the coercive fields are isotropic although in this case they are even slightly smaller amounting to 0.2 mT.

In order to convey an impression of the anisotropic behaviour the normalized remanent magnetizations are plotted as a function of the in plane crystallographic directions for samples with thicknesses of 12 and 60 monolayers (see figure 5.19). Considering that the coercive fields are isotropic and neglecting the exact shapes of the hysteresis loops, the coercive fields are roughly linearly proportional to the energy of the remagnetization process (see equation 2.28). These angular dependent plots of the remanent magnetization are, however, not to be confused with plots of magnetic anisotropy energies such as the one shown in figure 2.4 but rather inverse, i. e. where the anisotropy plot takes on a maximum the overall anisotropy energy would be at a minimum. Bearing this in mind, the plot in figure 5.19 shows that in the case of the 12 ML sample the anisotropy is twofold due to the dominant uniaxial magnetic anisotropy where the easy direction lies along the  $[1\bar{1}0]$  direction. In contrast to that, the anisotropy of the 60 ML sample almost exhibits a fourfold symmetry with easy directions along the  $\langle 100 \rangle$  directions due to the magnetocrystalline anisotropy. As was already mentioned, a small contribution from the uniaxial magnetic anisotropy can still be observed in favour of the  $[110]$  direction. However, for another

sample fabricated with the same nominal parameters the anisotropy plot exhibits a small uniaxial magnetic anisotropy in favour of the  $[1\bar{1}0]$  direction (see figure 5.22 in the context of the analysis of possible influences caused by capping layers). Again, for a more detailed discussion of this topic the reader is referred to section 5.4.3.

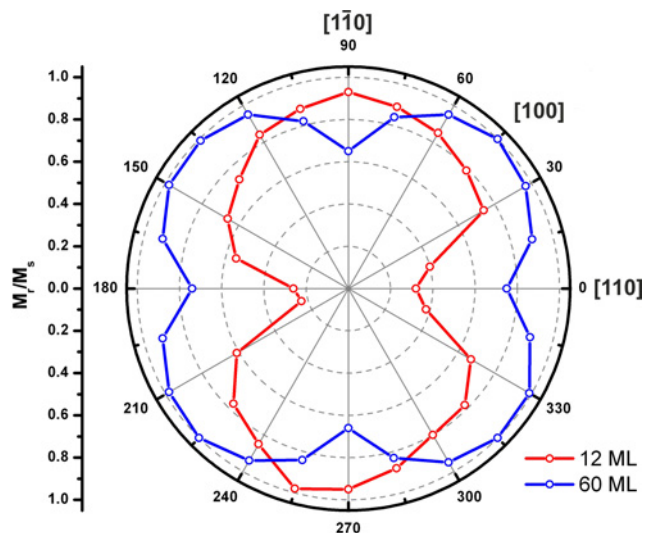


Figure 5.19: In plane angular dependencies of the normalized remanences as measured by in situ MOKE for samples with Fe<sub>3</sub>Si thicknesses of 12 and 60 monolayers.

To fabricate more samples with varying thicknesses under otherwise equal growth and post annealing conditions, single substrates were used on which layers with stepwise graded thicknesses ranging from 5 to 60 monolayers were deposited. This was realized by using a shutter mechanism that could be actuated via a linear feedthrough which was flanged onto the MOKE chamber instead of a DN38CF viewport for this series of experiments. In order to make the transitions between the different steps as sharp as possible, the shutter was placed directly beneath the sample holder. Thus, the effective distance between the shutter and the sample amounted to approximately 1.5 mm. The deposition was done in such an order that initially the entire substrate was exposed to the molecular beams of the Fe and the Si evaporators. To obtain stepwise graded thicknesses of the Fe<sub>3</sub>Si layers, the substrate was incrementally shaded by the shutter in steps of about 2.5 mm. A first magnetic characterization of these samples was again done by in situ MOKE where the laser beam could be aligned to the different steps, respectively. The hysteresis loops shown in figure 5.20 were measured along the  $[1\bar{1}0]$  direction on steps with thicknesses of 5, 10 and 20 monolayers. Although in [Her08] it is stated that from the interpolation of SQUID magnetometry data the onset of ferromagnetism at room temperature of Fe<sub>3</sub>Si/GaAs(001) starts at Fe<sub>3</sub>Si film thicknesses of about 1.8 nm which corresponds to 6.4 monolayers the MOKE measurements shown here point out ferromagnetic behaviour even at a thickness of 5 monolayers. On the other hand, it is also observed in [Her08] that the magnetization

of this system does not drop as sharply when approaching  $T_C$  as is expected from an ideal two-dimensional ferromagnet (see figure 2.3 in section 2.2.1). The reason for this may be, that in this thickness regime the Fe<sub>3</sub>Si film does not yet exhibit the pseudo Frank-van der Merwe growth but is to some extent still composed of islands with different heights (see image 5.25 in section 5.4.2). Understandably, the signal-to-noise ratio obtained from the 5 ML step is quite low even though averaging was done over 300 cycles in this case. In comparison, the 10 ML step yields hysteresis loops with significantly less noise. As in the case of the sample with an Fe<sub>3</sub>Si film thickness of 12 monolayers, the [110] direction is a hard axis due to the dominance of the uniaxial magnetic anisotropy. The remanence for the 20 ML step is found to be increased. Apparently, this is a thickness around which the transition from a predominantly uniaxial towards a predominantly magnetocrystalline anisotropy occurs. A quantitative analysis of the anisotropic behaviour, for which the samples with stepwise graded thicknesses will serve as a basis due to their identical growth conditions is the subject of section 5.4.3.

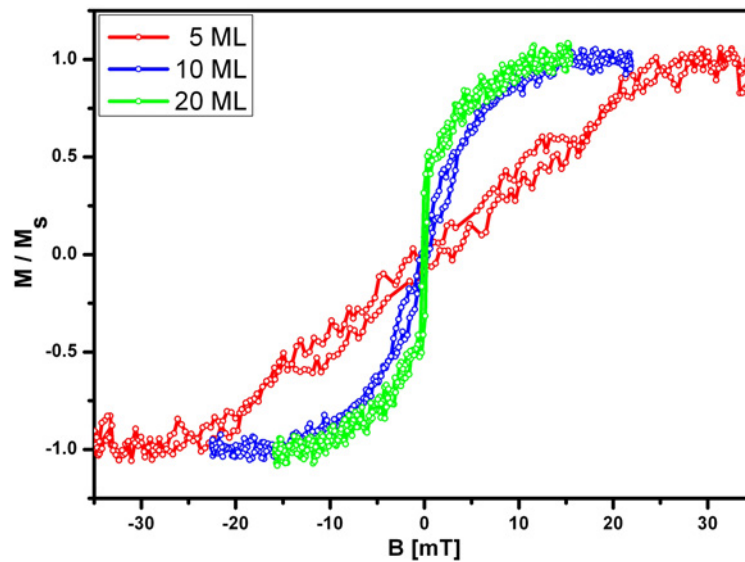


Figure 5.20: Hysteresis loops measured on the different sections of a sample with stepwise graded thicknesses along the [110] direction.

The structural analysis of an Fe<sub>3</sub>Si film deposited at an elevated growth temperature of 250 °C revealed that for comparable thicknesses parts of the substrate remain uncovered while the layer has a network-like morphology due to the interconnected terraces (see figure 5.10 in section 5.2). The corresponding hysteresis loop and the anisotropy plot of the same sample are shown in Figure 5.21. The anisotropy points out that despite the different layer morphology the sample exhibits a strong uniaxial magnetic anisotropy which is even more pronounced than in the case of a growth temperature of 200 °C. As in the case of 12 ML Fe<sub>3</sub>Si/GaAs(001) using  $T_G = 200$  °C and post annealing at 300 °C the

UMA is oriented along the  $[1\bar{1}0]$  direction which is in accordance with growth temperature dependence of the UMA direction mentioned above. However, the hysteresis loop on the left hand side of figure 5.21 also exhibits a substantially increased coercive field of 2.2 mT. Compositional deviations with a tendency of an iron surplus which could increase the coercive field can be excluded as RBS measurements of this sample again yield a silicon content of  $(23 \pm 2)$  at.%. It is rather most likely that the increased coercive field is caused by finite size effects which shift the magnetization reversal process to higher applied fields. In the case shown here, where the  $[100]$  direction is an intermediate axis, it can be assumed that the magnetization reversal process is a superposition of incoherent rotation and domain wall movement. It appears that the finite size effects have an influence on both mechanisms of the magnetization reversal processes as the coercive fields remain isotropic.

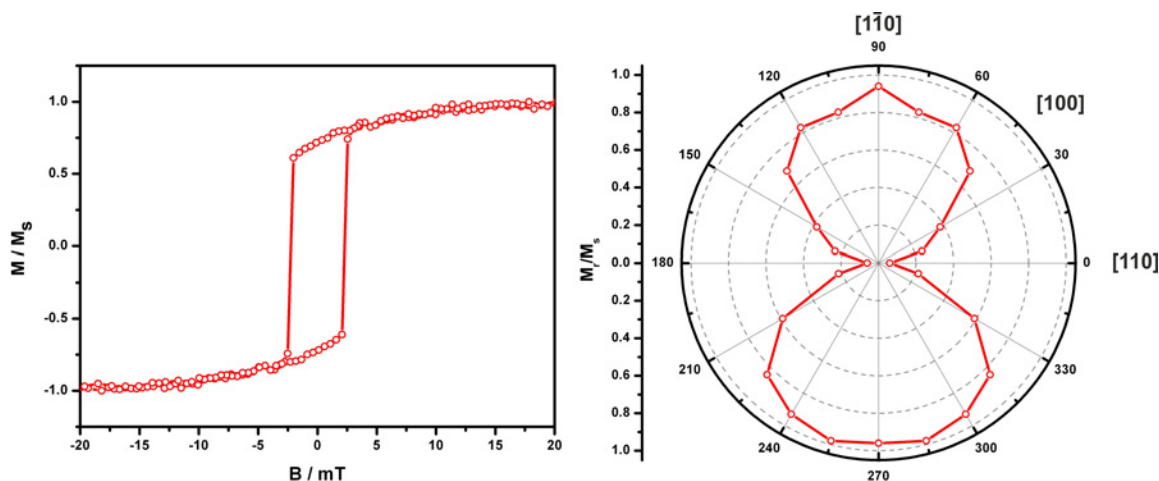


Figure 5.21: Left: Hysteresis loop measured along the  $[100]$  direction of 13 ML Fe<sub>3</sub>Si/GaAs(001) grown at a temperature of 250 °C. Right: Angular dependent normalized remanences of the same sample.

### The influence of capping layers

For magnetic ex situ analyses it was necessary to provide the samples with capping layers as the exposure to air would result in their oxidation which could alter properties such as the magnetic moment. Like in previous works [Spo04, Urb05], the capping layers were fabricated by the deposition of silver followed by the deposition of gold where in each case layer thicknesses of 2.5 nm were chosen. Thus, silver constitutes the first part of the capping layer for the ferromagnetic film where no interdiffusion and no solubility of silver in the case of iron could be observed even at 950 °C [Küh01]. Furthermore, in comparison to gold on iron which leads to a reduction of the magnetic moment there seems to be no such influence in the case of silver on iron layers [Elm88] where at this point we assume that the same accounts for Fe<sub>3</sub>Si layers. On the other hand, silver layers alone in this thickness regime

cannot safely prevent the diffusion of oxygen into the magnetic layers. Indeed, their thickness would need to be increased to approximately 20 nm [Rup02]. Therefore, an additional 2.5 nm thick layer of gold was deposited which effectively prevents oxidation. Nevertheless, it cannot be ruled out that certain magnetic properties such as the surface anisotropy can still be influenced by the capping layers which is one reason why in situ methods are still favourable.

In order to analyze the possible influence of capping layers on the remagnetization process and magnetic anisotropies, in situ MOKE measurements were performed on a 60 ML  $\text{Fe}_3\text{Si}/\text{GaAs}(001)$  sample before and after the deposition of the silver and gold capping layers as shown in figure 5.22. The left hand side shows hysteresis loops measured along the  $[100]$  direction which at this thickness corresponds to an easy axis. Obviously, the two curves are almost congruent in large parts although an increase of the coercive field of approximately 10% can be observed. However, this should not play a vital role for our magnetic characterization. The angular dependent plots of the normalized remanences before and after capping shown on the right hand side illustrate that the magnetic anisotropy remains mainly unaffected. Small deviations at some points are within the limits of the uncertainties when determining the remanent magnetization from hysteresis loops.

The in situ MOKE measurements shown here demonstrate that, at least for the considered layer thickness, no notable influence of the capping layers on the overall magnetic anisotropy can be observed.

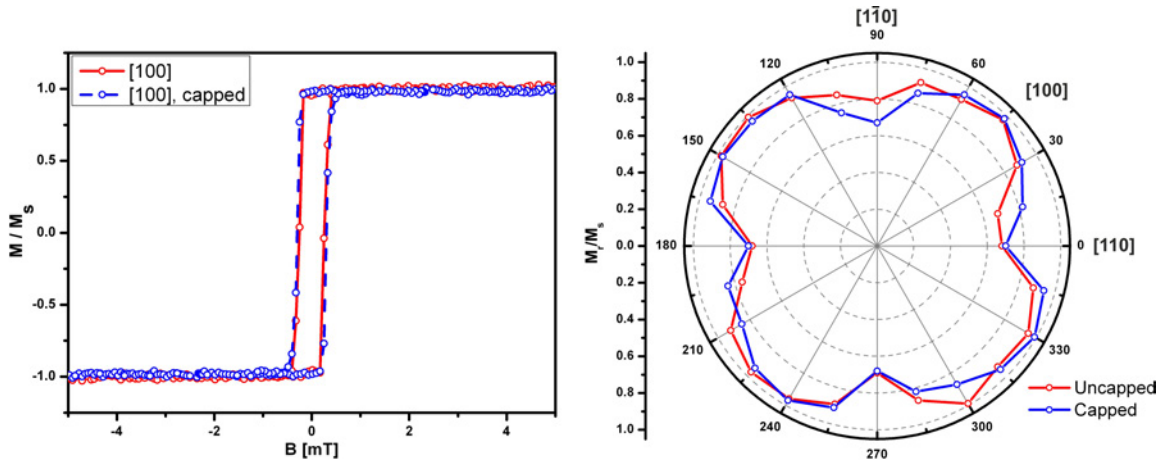


Figure 5.22: Left: Hysteresis loops measured by in situ MOKE along the  $[100]$  direction of 60 ML  $\text{Fe}_3\text{Si}/\text{GaAs}(001)$  before and after capping with 2.5 nm of Ag and Au, respectively. Right: Plot of the normalized remanences of the sample measured before and after capping.

### Temperature dependent in situ MOKE

The integration of a cryostat into the MOKE/MBE chamber and its connection to the sample mount in the framework of modifications described in section 4.2.2 allows the temperature dependent measurement of in situ MOKE hysteresis loops. First results are presented here in the context of the magnetic characterization of the system Fe<sub>3</sub>Si/GaAs(001).

A sample with a nominal Fe<sub>3</sub>Si film thickness of 40 monolayers was considered which, at least in terms of magnetic moment and in plane magnetocrystalline anisotropy as will be shown in the following sections, exhibits bulk-like properties. Of course, in this thickness range it can be assumed that shape anisotropy still has a considerable contribution to the overall magnetic anisotropy. Like for the other samples, the Fe<sub>3</sub>Si layer fabrication was done using the optimized growth parameters, i. e. a total deposition rate of 0.1 nm min<sup>-1</sup> at a growth temperature of 200 °C and post annealing at 300 °C. The D0<sub>3</sub> structure of Fe<sub>3</sub>Si was verified by low energy electron diffraction.

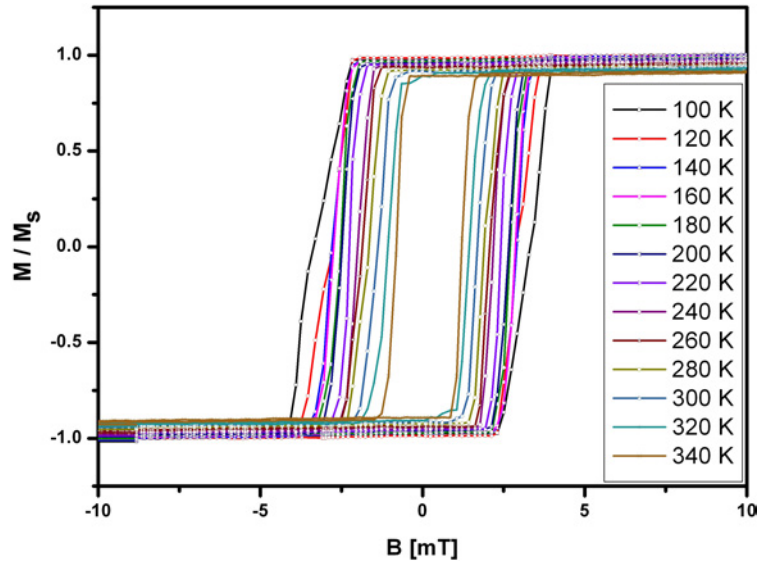


Figure 5.23: Temperature dependent MOKE hysteresis loops for an easy axis of Fe<sub>3</sub>Si/GaAs(001). The magnetization values are normalized to the saturation magnetization measured at 100 K.

Figure 5.23 shows hysteresis loops which were measured between 100 K to 340 K in steps of 20 K along an easy direction. This could be done without realigning the MOKE components and thus, the values of  $M_r$ , which for this easy direction correspond to the respective  $M_s$  within the measurement accuracy, can be brought into relation. What is, however, most noticeable from the temperature dependent hysteresis loops is the steady increase of the coercive field towards lower temperatures. The shape of the curves indicates a magnetization reversal process by domain wall motion. It becomes apparent that this motion becomes increasingly inhibited with decreasing temperature and requires higher applied fields. This is also illustrated in the temperature dependent plot of the coercive fields on

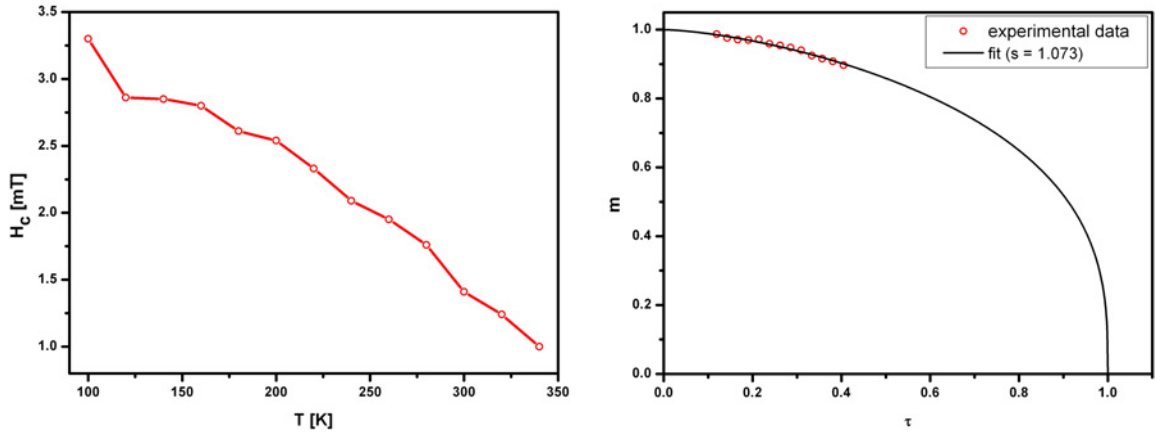


Figure 5.24: Left: Temperature dependent coercive fields determined from the hysteresis loops shown in figure 5.23. Right: The reduced magnetization  $m \equiv M_s/M_0$  as a function of the reduced temperature  $\tau \equiv T/T_C$  as determined by in situ MOKE and the corresponding fit using equation 5.3.

the left hand side of figure 5.24. It should be noted that the coercive field of this sample at room temperature was relatively high amounting to approximately 1.4 mT. Although LEED pointed out the formation of the typical D0<sub>3</sub> structure of Fe<sub>3</sub>Si differences of the coercive field might be attributed to compositional deviations.

Plotted on the right hand side of figure 5.24 is both the experimental data as well as fitted data of the reduced magnetization,  $m \equiv M_s/M_0$ , as a function of the reduced temperature,  $\tau \equiv T/T_C$  where the Curie temperature of bulk Fe<sub>3</sub>Si of 840 K [Len06] was assumed. The basis for this fit is the following semi-empirical formula for the temperature dependence of the magnetization which was introduced in [Kuz05]:

$$m(\tau) = \left[1 - s\tau^{\frac{3}{2}} - (1-s)\tau^{\frac{5}{2}}\right]^{\beta}, \quad \beta = \text{const} \approx \frac{1}{3}. \quad (5.3)$$

Here,  $s$  is the so-called shape parameter. Although the formula cannot be strictly derived from basic principles, it is up to now the only general analytical expression for  $m(\tau)$  in the whole range of  $0 \leq \tau \leq 1$  besides the molecular field approximation of Weiss (see section 2.2.1). However, it can be justified as described in [Kuz06] by bridging the gap between analytical expressions for  $m(\tau)$  for  $\tau \rightarrow 0$  [Dys56] and  $\tau \rightarrow 1$  [Cal65]. This is done by legitimate truncations of series expansions on the one hand and, more intricately, by elevating  $m$  to the power law of  $1/\beta$  on the other hand where  $\beta$  is the power by which  $m$  approaches zero close to  $T_C$ . In comparison to Weiss' mean field approximation and by considering experimental data, equation 5.3 describes  $m(\tau)$  correctly where solely the shape parameter  $s$  needs to be fitted. In the case of the Fe<sub>3</sub>Si/GaAs(001) sample considered here, the fit to experimental data yields a shape parameter of  $s = 1.073$  which is a rather typical value for the ferromagnets characterized in [Kuz05]. However, this result needs to be treated with caution as it does not claim to be representative for Fe<sub>3</sub>Si as a 3D ferromagnet.

### 5.4.2 Magnetic moments

SQUID magnetometry was used to determine the magnetic moments of the ferromagnetic layers and, by knowledge of the amount of deposited material, the magnetic moment per atom. For each sample hysteresis loops as well as the temperature dependent magnetic moment were measured. From the hysteresis loops it is possible to determine the amount of the diamagnetic contributions which can mainly be attributed to the substrate and the SQUID sample holder. This can easily be done because the magnetization due to ferromagnetism, which should maintain a constant value above the saturation field strength, is superimposed with the linear dependence  $M = \chi H$  due to diamagnetism, where  $\chi$  is a negative value with  $|\chi| \ll 1$ . The diamagnetic contribution can then be determined by generating the difference of the values of the magnetic moments between the as measured hysteresis loops and the hysteresis loops from which the linear contribution has been subtracted. In order to make a correction of the magnetic moment as a function of temperature it is only necessary to determine the diamagnetic contribution at the applied field which was used for those measurements and to shift the  $\mu(T)$  curves accordingly. For the samples considered here, the applied field amounts to 50 mT.

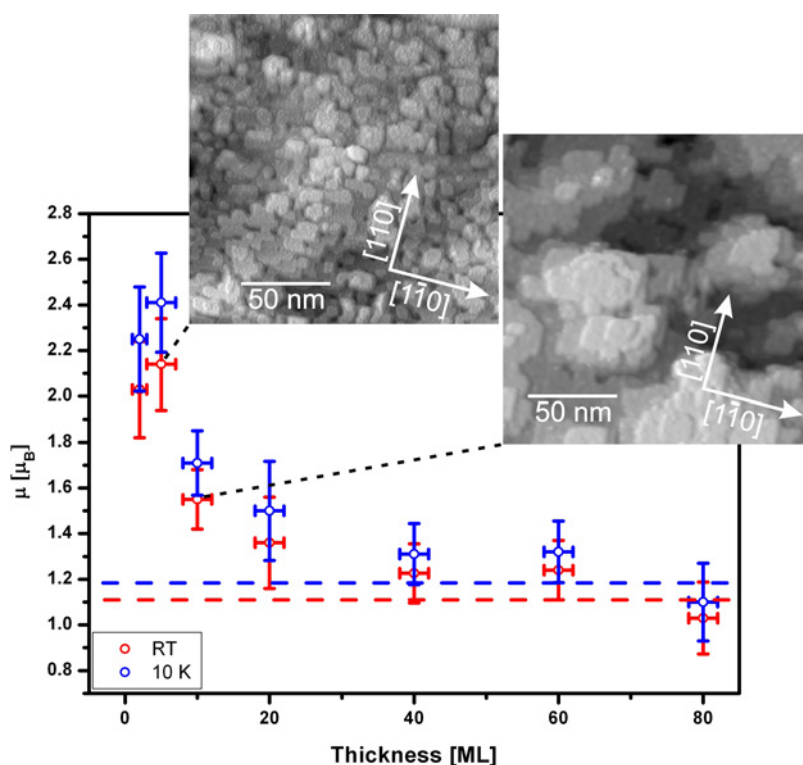


Figure 5.25: Average magnetic moments per atom at room temperature and 10 K as measured by SQUID magnetometry. The dashed lines indicate the corresponding bulk or bulk-like values. The insets show the layer morphology at thicknesses of 5 and 10 monolayers as measured by STM.

The magnetic moments as a function of the layer thicknesses in the range of 2 to 80 monolayers and measured at room temperature and 10 K are plotted in figure 5.25 in units of the Bohr magneton  $\mu_B$ . The values for layer thicknesses of 5, 10 and 20 monolayers and 40, 60 and 80 monolayers, respectively, originate from samples with stepwise graded thicknesses which were fabricated as described in section 5.4.1. These samples were then segmented into parts with the above-mentioned thicknesses using a diamond cutter under the simultaneous optical inspection with a conventional light microscope at the 'Lehrstuhl für angewandte Festkörperphysik' (University of Bochum). Although its structural and magnetic properties deviate from those of closed Fe<sub>3</sub>Si films (see section 5.5), the magnetic moments for a 2 monolayer sample are also included here for comparison. The dashed lines in figure 5.25 indicate the bulk magnetic moments which amount to  $1.175 \mu_B$  at 6.5 K [Hin76] (blue line), which in good approximation also serves as a reference at 10 K, and  $1.107 \mu_B$  at room temperature [Ion05b] (red line).

The general trend of the thickness dependent magnetic moment per atom is that the bulk value is approached for thicknesses of 40 monolayers and above. The slight reduction in comparison with the bulk values at 80 monolayers is still within in the range of the error bar but could otherwise also be attributed to a degradation of the crystalline quality which might increase with increasing layer thickness. For lower thicknesses, an increase in the magnetic moment can be observed which peaks at 5 monolayers. Here, the magnetic moment amounts to  $(2.14 \pm 0.20) \mu_B$  even at room temperature which is almost twice as large as the bulk value. This is rather unexpected as it is often believed that magnetically inactive layers would be formed at the interface due to interdiffusion processes which would reduce the magnetic moment per atom especially towards lower coverage. However, as already discussed in section 1.1, experimental results found in literature regarding the interface quality are somewhat controversial. This subject can also not be ultimately clarified here because the employed experimental methods cannot rule out a certain degree of interdiffusion at the interface. Nevertheless, it should be pointed out, especially with regard to the significance of FM/SC interfaces for spintronic applications, that in works such as [Her03] in which no interdiffusion could be detected a growth temperature of 200 °C was used. On the other hand, in works such as [Kru09] in which some interdiffusion could be found a growth temperature of 250 °C was employed. The Fe<sub>3</sub>Si layers considered here were deposited at 200 °C although they were subject to post annealing at 300 °C. As was the case for the surface morphology in section 5.2, also the interface qualities might differ depending on whether an increased growth temperature or a lower growth temperature with subsequent post annealing is used. The increased magnetic moments at thicknesses of 20 monolayers and below can possibly be attributed to two different effects. The first might be surface and interface anisotropies (see section 2.2.1 for a theoretical background). The second effect consists of an increasing contribution of the orbital moment towards lower coverage which unlike within bulk systems are no longer quenched at the surface and step edges as could already be shown for Co/Cu(001) for example [Tis95]. This is also in good

agreement with the layer morphology that can be found in this thickness regime as illustrated in the insets in figure 5.25. These STM images which show the transition from an almost 3D island-like morphology at 5 monolayers towards the onset of pseudo Frank-van der Merwe growth at 10 monolayers point out the considerable contribution of step edges at low coverage.

### 5.4.3 Quantitative analysis of the magnetic anisotropies

The magnetic anisotropies of Fe<sub>3</sub>Si layers on GaAs(001) determined by MOKE in the form of in plane angular dependent remanence plots as described in section 5.4.1 yielded a more qualitative description of the anisotropic behaviour while they had the advantage that they could be performed in situ. A quantitative analysis that can determine anisotropy fields as fit parameters according to the Smit-Beljers formalism (see section 3.5) can be done using FMR. Furthermore, by knowledge of the magnetization values that could be obtained from the SQUID magnetometry measurements shown in the previous section also the anisotropy constants can be determined. Fe<sub>3</sub>Si layer thicknesses in the range of 5 to 60 monolayers are considered here where the samples are the same as those used for the SQUID magnetometry measurements.

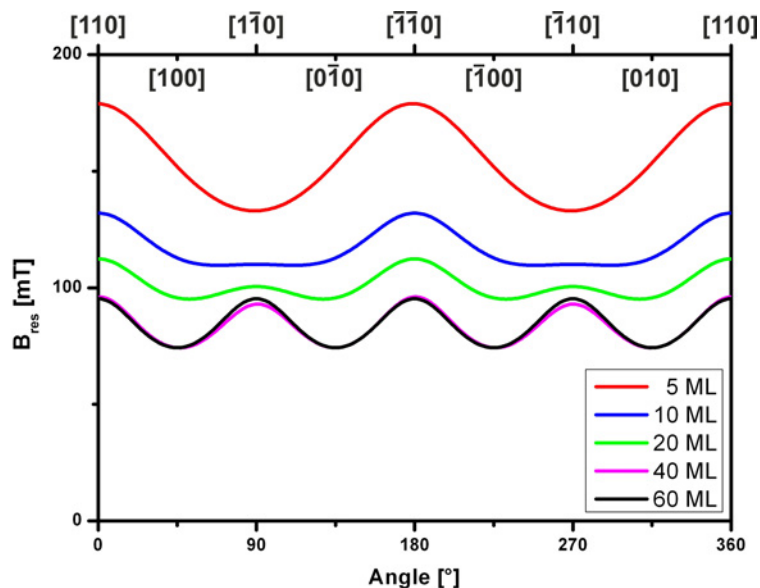


Figure 5.26: Fits of the angular dependent FMR resonance fields for Fe<sub>3</sub>Si film thicknesses in the range of 5 to 60 monolayers. The trend from a purely uniaxial anisotropy at 5 monolayers towards a predominantly fourfold magnetocrystalline anisotropy at 60 monolayers can be observed.

FMR spectra from which the resonance fields could be determined were measured in plane in steps of 2°. Figure 5.26 shows fits of these angular dependent resonance fields where, consistent with the angular dependent MOKE measurements, the [110] direction was appointed as the 0° direction. In this plot the transition from a purely uniaxial anisotropy at

5 monolayers with an easy axis along the  $[1\bar{1}0]$  direction towards a purely fourfold magnetocrystalline anisotropy at 60 monolayers becomes obvious. Also, a general reduction of the resonant fields with increasing layer thicknesses can be observed which indicates that compared to the magnetocrystalline anisotropy a higher energy is associated with the uniaxial anisotropy.

From the fit of the angular dependent resonance fields the thickness dependence of the magnetocrystalline anisotropy fields and, as mentioned above by using magnetization values from SQUID magnetometry measurements, the thickness dependence of the magnetocrystalline anisotropy constant  $K_1$  can be extracted as shown in the plot in figure 5.27. The error bars are dominated by the uncertainty of the sample volume and hence the uncertainty of the magnetization which was also the case for the SQUID magnetometry measurements. The individual FMR spectra (not shown here) oftentimes exhibited weaker resonance lines besides a dominant one which can be ascribed to a certain inaccuracy in the segmentation process of the samples with stepwise graded thicknesses. Hence, the error bars seem justified. At a thickness of 5 monolayers the magnetocrystalline anisotropy still makes no contribution to the overall anisotropy within the detection limits of FMR. The most notable increase can be observed at around 10 monolayers and, finally,  $K_1$  seems to reach a saturation value of almost  $6 \text{ kJ m}^{-3}$  at thicknesses of approximately 40 monolayers and above which is close to the bulk-like values found by theory and experiment in [Bar11].

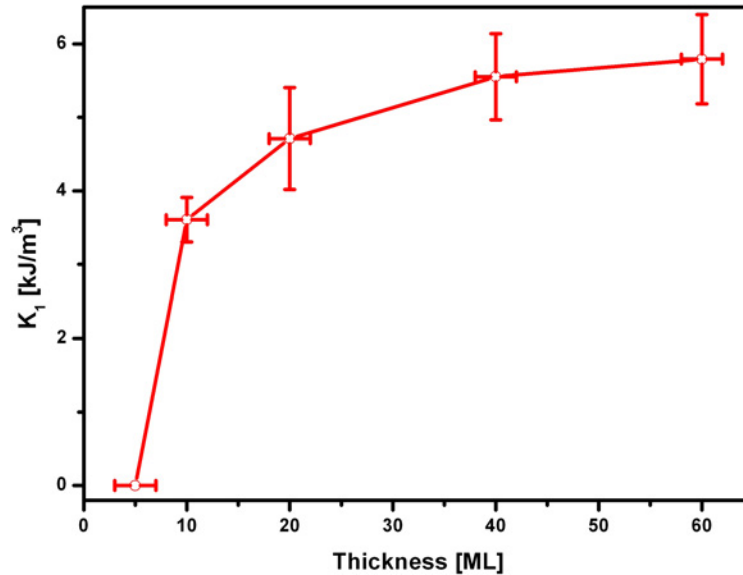


Figure 5.27: Thickness dependence of the magnetocrystalline anisotropy constant  $K_1$  determined from SQUID magnetometry and FMR measurements.

The thickness dependence of the uniaxial magnetic anisotropy constant was determined accordingly. In section 5.4.1 it was already mentioned and formulated by equation 5.2

that the effective UMA consists of a volume and an interface term where the latter has a  $1/d$  dependence. Therefore, plots of the UMA constant both as a function of the thickness but also of the inverse thickness are shown in figure 5.28. In the plot versus the thickness on the left hand side it can be observed that the UMA constant rapidly decreases with increasing film thickness, reaches values below  $5 \text{ kJ m}^{-3}$  above thicknesses of 10 monolayers and finally, again within the detection limit of FMR, reaches zero at 60 monolayers. The plot of the UMA constant versus the inverse thickness should yield a linear dependence and was therefore fitted under consideration of the error bars as weights for the data points. Thus, the effective uniaxial magnetic anisotropy is described by  $K_u^{\text{eff}} = -0.97 \text{ kJ m}^{-3} + 1.56 \cdot 10^{-8} \text{ kJ m}^{-2} \cdot 1/d$  where  $d$  is the thickness. This shows that  $K_u^{\text{vol}}$  and  $K_u^{\text{int}}$  have opposite signs and therefore that by virtue of equation 3.47 there should be a reorientation of the UMA. According to the fit, this transition should occur at a thickness of 59 monolayers. The trend observed here is in agreement with the experimental findings reported in [Her08] where, however, also Fe<sub>3</sub>Si films with significantly higher thicknesses were measured which indeed exhibited an easy UMA axis along the [1 1 0] direction. Nevertheless, already the in situ MOKE measurements in section 5.4.1 but also [Len05] and [Her08] indicated that the direction of the uniaxial anisotropy and its reorientation sensitively depend on the growth temperature. To make a more reliable statement about the growth temperature dependence of  $K_u^{\text{vol}}$  and  $K_u^{\text{int}}$  would require a more thorough investigation including the fabrication of a significantly higher amount of samples. On the other hand, this would be a purely academic pursuit. The fact for practical applications is that the UMA is always negligible compared with the magnetocrystalline anisotropy in the anent thickness regime.

The FMR and SQUID magnetometry data could furthermore be used to determine the

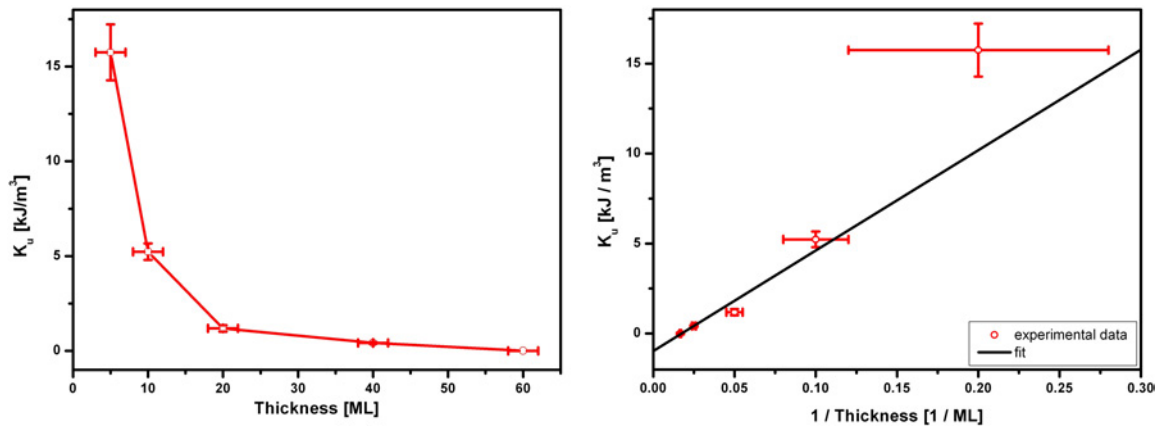


Figure 5.28: Left: Thickness dependence of the in plane uniaxial anisotropy constant  $K_u$  as measured by FMR and SQUID magnetometry. Right: Experimental data and a linear fit of  $K_u$  plotted as a function of the inverse thickness where according to equation 5.2 a linear dependence is expected.

thickness dependence of the out of plane anisotropy field which depends on contributions from the demagnetization field and volume and surface out of plane anisotropies according to  $B_{\perp} = \mu_0 M - \left( \frac{K_{\perp}^{\text{vol}}}{M} + \frac{K_{\perp}^{\text{s}}}{dM} \right)$ . Similar to the in plane uniaxial anisotropy the out of plane anisotropy has volume and surface contributions which can be subsumed under an effective out of plane anisotropy as  $K_{\perp}^{\text{eff}} = K_{\perp}^{\text{vol}} + \frac{K_{\perp}^{\text{s}}}{d}$ . This is plotted in figure 5.29 as a function of the film thickness. For a thickness of 5 monolayers  $K_{\perp}^{\text{eff}}$  takes on values of almost  $8 \cdot 10^3 \text{ kJ m}^{-3}$ . It increases with the film thickness and approaches a value of approximately  $2.7 \cdot 10^3 \text{ kJ m}^{-3}$  above 20 monolayers. Presumably this volume contribution of the out of plane anisotropy can be ascribed to stress induced during the heteroepitaxial growth of Fe<sub>3</sub>Si on GaAs(001).

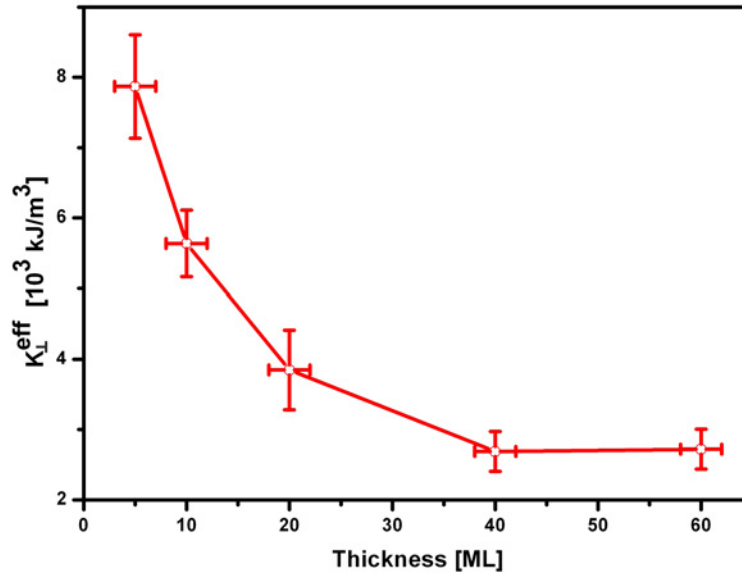


Figure 5.29: Thickness dependence of the out of plane anisotropy constant  $K_{\perp}^{\text{eff}}$  determined from SQUID magnetometry and FMR measurements.

FMR linewidths as they are shown in figure 5.30 can be used to get an estimate of the sample homogeneities. Towards higher coverage a decrease of the linewidth can be observed. At a thickness of 40 monolayers it amounts to  $(1.60 \pm 0.15) \text{ mT}$  which is comparable to the value of an 8 nm thick layer of Fe<sub>3</sub>Si on MgO(001) as determined in [Zak07] where usually the crystalline quality of Fe<sub>3</sub>Si is believed to be much better than on GaAs. It can be assumed that this is due to higher purities of the substrate surfaces which in turn is the result multiple sputter and annealing cycles before achieving a satisfactory inspection by STM as opposed to inspection simply by diffractive methods such as LEED. On the other hand, linewidths of 1.3 and 1.7 mT for Fe<sub>3</sub>Si/GaAs(001) have already been observed in [Len06] although the film thicknesses considered there were significantly higher amounting to 33 and 39 nm.

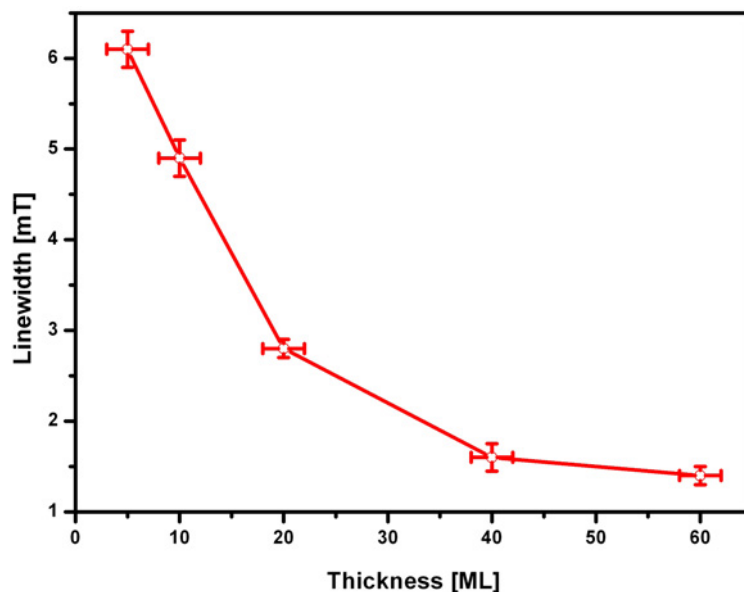


Figure 5.30: Thickness dependent linewidths obtained from the FMR spectra of the  $[1\bar{1}0]$  directions.

## 5.5 Fe<sub>3</sub>Si/GaAs(001) at low coverage

Up to now, the structural properties and the magnetic behaviour of closed Fe<sub>3</sub>Si films on GaAs(001) were considered. This section is dedicated to the characterization of Fe<sub>3</sub>Si/GaAs(001) upon nucleation in a thickness regime where the underlying Volmer-Weber growth mechanism still prevails. The Fe<sub>3</sub>Si film thickness as a function of the deposited material shown in figure 5.31 determined *in vivo* by XRD measurements [Kag09] serves as a reference.

### 5.5.1 The structure and morphology at low coverage

The STM overview scan in figure 5.32 shows the surface morphology of a 2 ML Fe<sub>3</sub>Si/GaAs(001) sample that was fabricated using optimized growth parameters (see section 5.2), i. e. a total deposition rate of  $0.1 \text{ nm min}^{-1}$  at a growth temperature of  $200^\circ\text{C}$ . The sample was also post annealed at  $300^\circ\text{C}$  for 45 minutes. It can be seen from the STM image, that the layer morphology is dominated by a 3D island-wise growth although the onset of coalescence can already be observed. The resulting structures are typically formed by  $(5 \pm 1)$  individually nucleated islands. They have widths of  $(25 \pm 10) \text{ nm}$  and heights of  $(0.92 \pm 0.08) \text{ nm}$  which corresponds to  $(3.3 \pm 0.3) \text{ ML}$ . This data point is included in the plot of the film thickness as a function of the amount of deposited material in figure 5.31 and it is found to be in good agreement with the data extracted by *in vivo* XRD measurements. The volumes of these structures amount to  $(230 \pm 40) \text{ nm}^3$ . As was the case for the terrace edges of the closed Fe<sub>3</sub>Si films but also for the edges of cavities which started to form

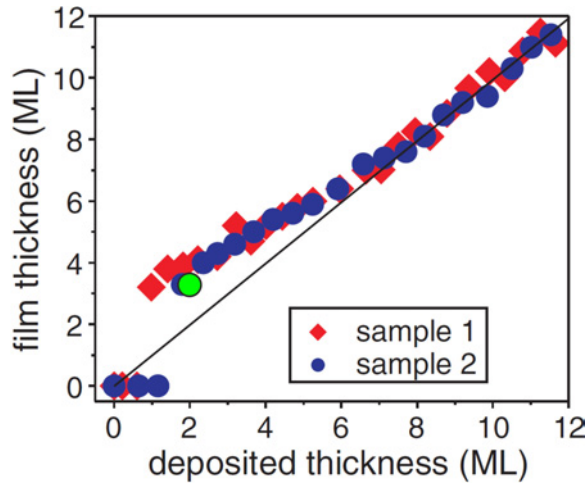


Figure 5.31: The Fe<sub>3</sub>Si film thickness as a function of the deposited material as determined from CTR fringes in XRD data [Kag09]. The green data point refers to the sample considered in this work.

upon post annealing at higher temperatures, also the structures at lower coverage exhibit a preferred edge orientation along the  $[1\ 1\ 0]$  and  $[1\ \bar{1}\ 0]$  directions. The inset on the top right hand side of figure 5.32 shows the corresponding LEED pattern. From the arrangement of the diffraction spots with respect to the substrate LEED pattern at a comparable electron energy (see figure 5.2) the existence of the D0<sub>3</sub> structure can be deduced. However, at this coverage traces of the substrate reconstructions still remain. Although the layer morphology determined by STM, i. e. the real space data, is different, the LEED pattern is comparable with the one measured on a sample with higher coverage but where Fe<sub>3</sub>Si was deposited at an elevated growth temperature of 250 °C (see figure 5.10). The close-up STM scan on the top left hand side of figure 5.32 reveals the atomic arrangement. Again, as was the case at higher coverage, a face-centred structure with respect to the  $\langle 1\ 0\ 0 \rangle$  directions is found which is in agreement with the D0<sub>3</sub> structure of Fe<sub>3</sub>Si where it is once more assumed that only one sublattice is imaged by STM.

### 5.5.2 Magnetic behaviour at low coverage

The magnetic analysis of the 2 ML Fe<sub>3</sub>Si/GaAs(001) sample required ex situ SQUID magnetometry measurements as it was not possible to obtain a signal using the in situ MOKE setup at room temperature. Figure 5.33 shows a plot of the magnetization loop that was recorded at 300 K. Compared to the hysteresis loops of the samples with closed Fe<sub>3</sub>Si films the magnetic behaviour which is observed here is fundamentally different. In relation to the large saturation field of approximately 600 mT, the magnetization loop exhibits only a small splitting. As already mentioned in section 1.1, Fe<sub>3</sub>Si/GaAs(001) is only known to become ferromagnetic only above a thickness of 3 monolayers even at low temperatures [Her08].

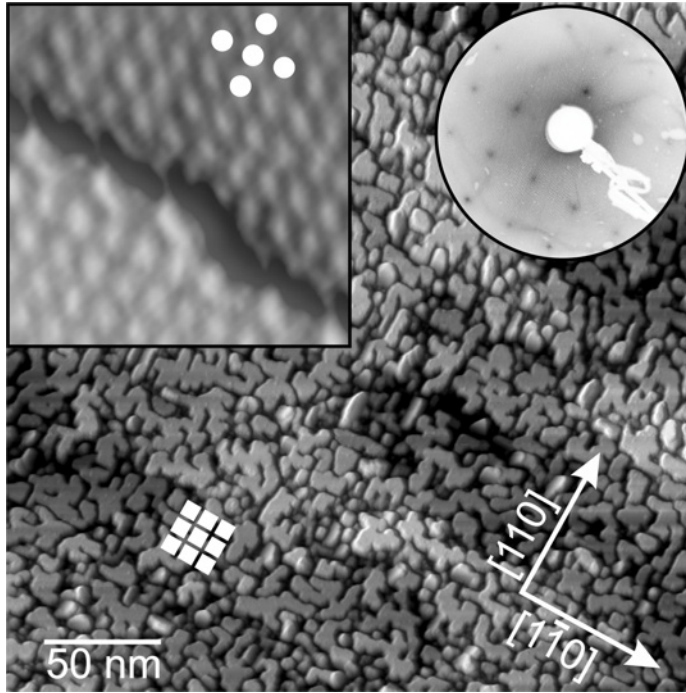


Figure 5.32: STM image of 2 ML Fe<sub>3</sub>Si/GaAs(001) ( $I = 1.0$  nA,  $U = 2.4$  V). The close-up scan on the left hand side inset shows the atomic arrangement while the inset on the right hand side shows the corresponding LEED pattern (135 eV). The small squares (for better visualization an array rather than a single square is shown) illustrate the effective size of the superparamagnetic clusters of this structure which will be discussed in the following section.

The question arises what kind of magnetic behaviour prevails in the lower thickness regime in which the morphology as observed by STM resembles a system of more or less isolated nanoparticles. As was already shown in section 5.4.2 in the context of the thickness dependence of the magnetic moments, also at a coverage of 2 monolayers the magnetic moment is found to be augmented above the bulk value amounting to  $(2.03 \pm 0.21) \mu_B$ .

If the system were superparamagnetic this could be determined by measuring zero-field-cooled (ZFC) and field-cooled (FC) curves as described in section 2.2.2. Indeed, as shown in figure 5.34 the splitting of the ZFC and FC curves which were measured at an applied field of 2 mT using a measuring time of approximately 10 s indicates superparamagnetic behaviour. Under the given parameters a blocking temperature of 55 K can be observed. Upon confirmation of the superparamagnetic behaviour, the magnetization loop in figure 5.33 was fitted with a Langevin function

$$L(y) = \coth(y) - \frac{1}{y} \quad (5.4)$$

where  $y = \frac{\mu B}{k_B T}$  with the superspin  $\mu$ . The fit yields a superspin of  $(17700 \pm 400) \mu_B$ . By knowledge of the average magnetic moment per atom this can be assigned to superparamagnetic nanoparticles consisting of  $(8730 \pm 170)$  atoms. Assuming a square-like shape in view

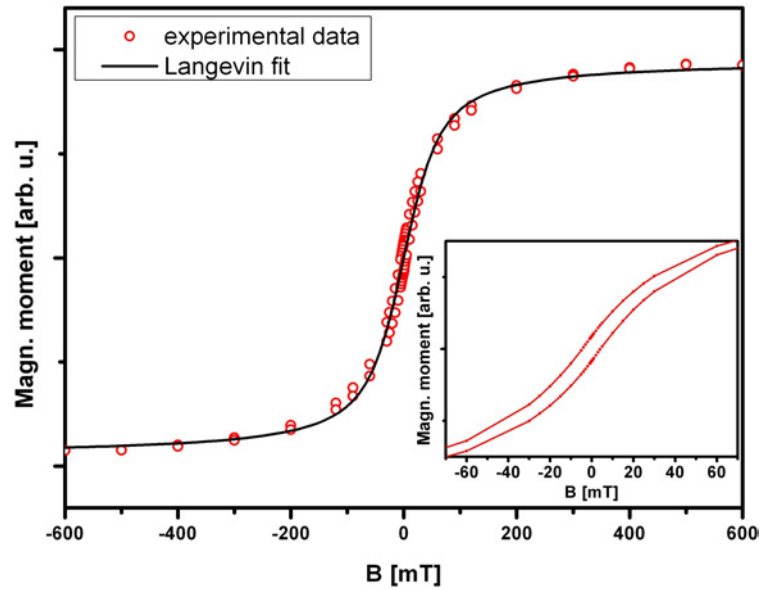


Figure 5.33: Magnetization loop of 2 ML  $\text{Fe}_3\text{Si}/\text{GaAs}(001)$  as measured by SQUID magnetometry at 300 K. The inset is a zoom-in revealing that there is still some splitting in the hysteresis loop. The solid line shows the fit of the data by a Langevin function.

of the STM data this corresponds to nanoparticles with an edge length of  $(7.8 \pm 0.2)$  nm as illustrated in figure 5.32. This is also in good agreement with the size of individually nucleated clusters or in other words the onset of coalescence does not seem to affect the magnitude of the superspins. However, a consequence might be that some regions could

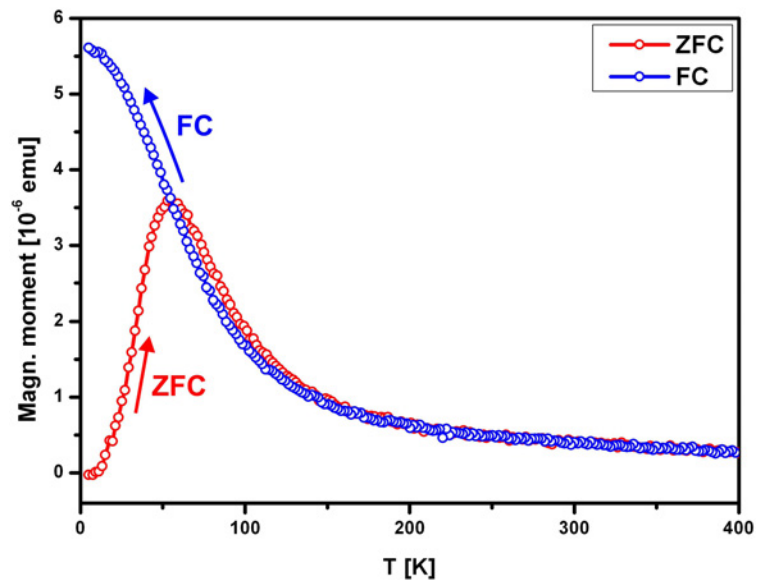


Figure 5.34: ZFC-FC-curve of the 2 ML  $\text{Fe}_3\text{Si}/\text{GaAs}(001)$  ( $B = 2$  mT,  $\Delta T/\Delta t = 2$  K/min).

deviate from the single domain state which could explain the splitting of the hysteresis loop. Retrospectively, it appears that a MOKE signal could not be detected as MOKE is only sensitive to exchange splitting.

Knowledge of the volume  $V$  of the superparamagnetic particles, the measuring time  $\tau$  and the blocking temperature  $T_B$  allows to determine the effective uniaxial anisotropy  $K$ . This can be done by rewriting equation 2.43 which yields

$$K = \frac{k_B T_B}{V} \ln \left( \frac{\alpha \tau}{\tau_0} \right). \quad (5.5)$$

Thus,  $K$  amounts to  $(370 \pm 60) \text{ kJ m}^{-3}$  which is comparable to the effective uniaxial anisotropy observed in other systems with superparamagnetic nanoparticles [Res99, Pet06].

## 5.6 Structural and magnetic correlations

At this point it shall be discussed where links between the structural and the magnetic properties for the system  $\text{Fe}_3\text{Si}/\text{GaAs}(001)$  can be established and where this is not possible.

The most obvious distinction can be made for the structural and magnetic properties for film thicknesses below 3 monolayers and for closed films. For closed films, a superposition of a magnetocrystalline and a uniaxial magnetic anisotropy is observed where the former dominates at thicknesses above 40 ML while the latter becomes substantial below 20 ML. Even at low thicknesses STM images reveal that both the surface morphology in the form of terraces as well as the atomic arrangement at the surface exhibit a fourfold symmetry. The terrace edges are oriented along the  $[110]$  and the  $[1\bar{1}0]$  direction but an elongation along of these directions cannot be observed (see figure 5.6). As a consequence, there seems to be no contribution from a structural shape anisotropy in the UMA. It must be assumed as was already suggested in [Len05] that the UMA is caused by the anisotropic bonding structure at the interface between GaAs and  $\text{Fe}_3\text{Si}$ . However, in the same thickness regime it can be shown that elevating the growth temperature changes both the layer morphology as the pseudo Frank-van der Merwe growth is shifted towards higher coverage as well as the magnetic behaviour. It appears that the formation of a terrace network rather than large-scale terraces increases the coercive field of the  $\text{Fe}_3\text{Si}$  film due to finite size effects. Not surprisingly, at higher thicknesses the fourfold magnetocrystalline anisotropy prevails due to the cubic symmetry of the  $\text{D0}_3$  structure of  $\text{Fe}_3\text{Si}$  which could be confirmed by STM and LEED. More remarkable is the increased magnetic moment that was observed towards lower thicknesses. The corresponding STM images provide evidence that this is most likely to be attributed to an increasing contribution of unquenched orbital moments due to a higher density of step edges at lower coverage (see figure 5.25). The layer morphology points out that the transition to a pseudo Frank-van der Merwe growth with increasing film thickness correlates with the asymptotic trend of the magnetic moment towards the

bulk value of Fe<sub>3</sub>Si.

As already mentioned above, both structural and magnetic properties are fundamentally different at a coverage below 3 monolayers. Here, the layer morphology is a direct consequence of the underlying Volmer-Weber growth mode, i. e. it largely consists of individually nucleated islands. The magnetic analysis showed that these Fe<sub>3</sub>Si clusters, where the structural analyses allow to identify them as such, exhibit superparamagnetic properties. Hence, Fe<sub>3</sub>Si/GaAs(001) at very low coverage behaves like a system of superparamagnetic nanoparticles.

## Chapter 6

# Fe<sub>3</sub>Si/GaAs(110)

GaAs(110) as a substrate features several interesting properties. For one, apart from a small rippling effect it does not exhibit any surface reconstructions which would facilitate theoretical considerations such as STM simulations. For structural and magnetic investigations it is furthermore interesting as all low-indexed directions, namely the  $\langle 001 \rangle$ , the  $\langle 110 \rangle$  and the  $\langle 111 \rangle$  directions, are contained in the (110) plane. The injection of spin polarized currents across GaAs(110) also seems to be favourable compared to GaAs(001) because the spin lifetimes are increased due to the suppression of the D'yakonov-Perel mechanism<sup>1</sup> [Li04, Ohn99]. The (110) face side obtained after cleaving GaAs(001) substrates is also interesting for spin LEDs with cleaved edge overgrowth (CEO) geometry. This combines the advantages of a simple conversion between spin and optical polarizations according to the Faraday geometry when emitting light via the (001) surface [Hol07] while at the same time being able to operate at magnetic remanence. The latter is due to the fact that ferromagnetic layers such as Fe grown on the (110) face side exhibit a magnetically easy axis along the  $[001]$  direction.

This chapter does not feature an extensive study of the structural and magnetic properties as was the case for Fe<sub>3</sub>Si/GaAs(001). However, the surface morphology and the atomic arrangement as well as a first magnetic characterization shall be considered here for selected film thicknesses. The parameters that were determined in section 5.2 to fabricate closed layers of Fe<sub>3</sub>Si on GaAs(001) with an optimized morphology were applied for the growth of Fe<sub>3</sub>Si on the (110) oriented substrates. As was already implied in section 1.1, the results shown here represent the first experimental work that has been done on this system.

---

<sup>1</sup>The D'yakonov-Perel mechanism describes a spin relaxation process in semiconductors without inversion symmetry like GaAs. In this case, an effective magnetic field acts on mobile electrons which results in spin precession and finally in spin relaxation. See [Zut04] for a more detailed description.

## 6.1 The (110) surface of GaAs

Unlike GaAs(001) which, depending on the preparation parameters, exhibits numerous reconstructions (see section 5.1) the (110) surface of GaAs is basically unreconstructed due to its non-polar composition. Merely a small rippling of the atomic rows at the surface can be observed which is a result of protruding As atoms and Ga atoms that are displaced inwards. As a result, the Ga-As bonds are rotated by  $\omega = 27^\circ$  (see figure 6.1) from their ideal orientation [Lub76].

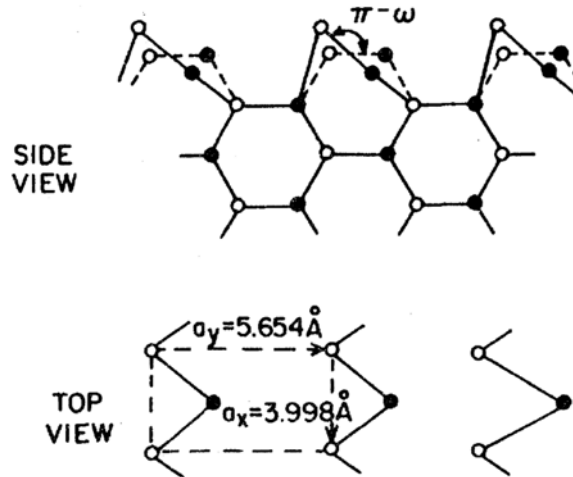


Figure 6.1: Surface atomic structure of GaAs(110) [Lub76]. Depicted in the side view is the rippling of the atomic rows due to the rotation of the Ga-As bond by  $\omega$ . The top view illustrates the (110) unit cell and the corresponding lattice constants.

GaAs(110) surface can be prepared either by cleaving bulk GaAs samples or by cleaning (110) oriented GaAs wafers by cycles of sputtering with subsequent annealing. The latter method was employed in this work because this allowed post annealing of Fe<sub>3</sub>Si/GaAs(110) samples in a more controllable fashion. Furthermore, access to the IBA-prepared samples by STM, LEED and MOKE is significantly easier due to their larger surface which amounts to approximately 5 mm × 8 mm as opposed to an estimated less than 2 mm<sup>2</sup> for cleaved edge samples.

The GaAs(110) substrates were extracted from commercially available GaAs(110) wafers (Wafer Technology Ltd.) by using a diamond cutter. Apart from the crystallographic orientation the wafers had identical parameters as in the case of GaAs(001), i.e. a thickness of  $(350 \pm 25)$  μm, a carrier concentration of approximately 10<sup>18</sup> cm<sup>-3</sup> where Si was used as a dopant and a specific resistance of about  $2 \cdot 10^{-3}$  Ω cm.

Figure 6.2 shows STM images of the clean GaAs(110) surface which in this case were obtained after three cycles of sputtering and annealing using the same parameters as described in section 5.1 for the GaAs(001) substrates without an As capping layer. The overview scan on the left hand side of figure 6.2 illustrates the terrace structure of GaAs(110) where

the layer spacing amounts to 0.2 nm which corresponds to  $\frac{\sqrt{2}}{4}$  of the lattice constant of GaAs. The STM image on the right hand side shows the atomic rows which are oriented along the  $[1\bar{1}0]$  direction. The unit cell has lattice constants of 0.5653 nm along the  $[001]$  direction and 0.3997 nm along the  $[1\bar{1}0]$  direction. The LEED pattern in the inset on the left hand side indicates the corresponding reciprocal  $(110)$  unit cell.

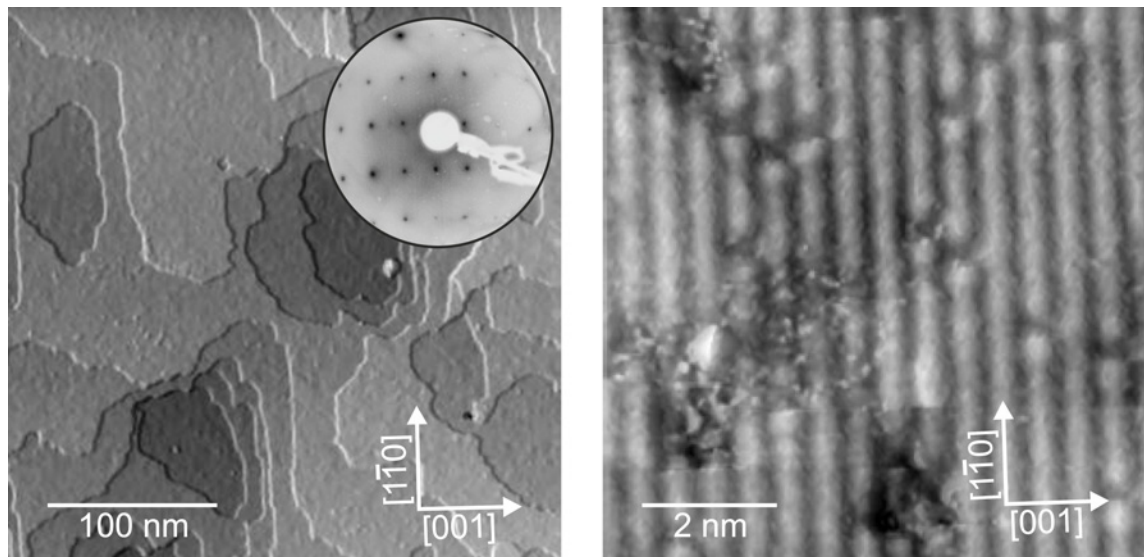


Figure 6.2: Left: STM overview scan of the GaAs(110) surface after three cycles of sputtering and annealing ( $I = 1$  nA,  $U = 3.3$  V). The inset shows the corresponding LEED pattern ( $E = 121$  eV). Right: A smaller scale STM image reveals atomic rows that are oriented along the  $[1\bar{1}0]$  direction ( $I = 0.1$  nA,  $U = 2.8$  V).

## 6.2 Structural properties

Presented here is a structural analysis by means of STM and LEED of  $\text{Fe}_3\text{Si}$  co-deposited on GaAs(110) by MBE. In analogy to  $\text{Fe}_3\text{Si}/\text{GaAs}(001)$  a total deposition rate of  $0.1 \text{ nm min}^{-1}$  and a growth temperature of  $200^\circ\text{C}$  were chosen followed by post annealing at  $300^\circ\text{C}$  for 45 minutes. In the first part of this section, the surface morphology is considered while the second part describes the atomic arrangement at the  $\text{Fe}_3\text{Si}$  surface.

### 6.2.1 Surface morphology of closed layers

The STM scan shown on the left hand side of figure 6.3 illustrates the surface morphology of  $\text{Fe}_3\text{Si}/\text{GaAs}(110)$  after post annealing. The thickness of this layer as determined by RBS amounts to 5.6 nm. RBS measurements furthermore indicate a composition of the iron silicide layer close to stoichiometric  $\text{Fe}_3\text{Si}$  as the Si content of the sample was determined to be  $(23.8 \pm 0.9) \text{ at.}\%$ .

At this considered thickness the surface appears more corrugated in comparison with Fe<sub>3</sub>Si/GaAs(001). However, the RMS roughness determined from the STM data only amounts to  $(0.4 \pm 0.04)$  nm which is not significantly higher than that of Fe<sub>3</sub>Si/GaAs(001). Moreover, it can be observed that the substrate is completely covered. STM linescans (see right hand side of figure 6.3) point out single step heights of  $(0.201 \pm 0.012)$  nm which corresponds to  $\frac{\sqrt{2}}{4}$  of the lattice constant of Fe<sub>3</sub>Si. Using the step height observed by STM as the definition for a monolayer, the Fe<sub>3</sub>Si film considered here consists of 28 monolayers.

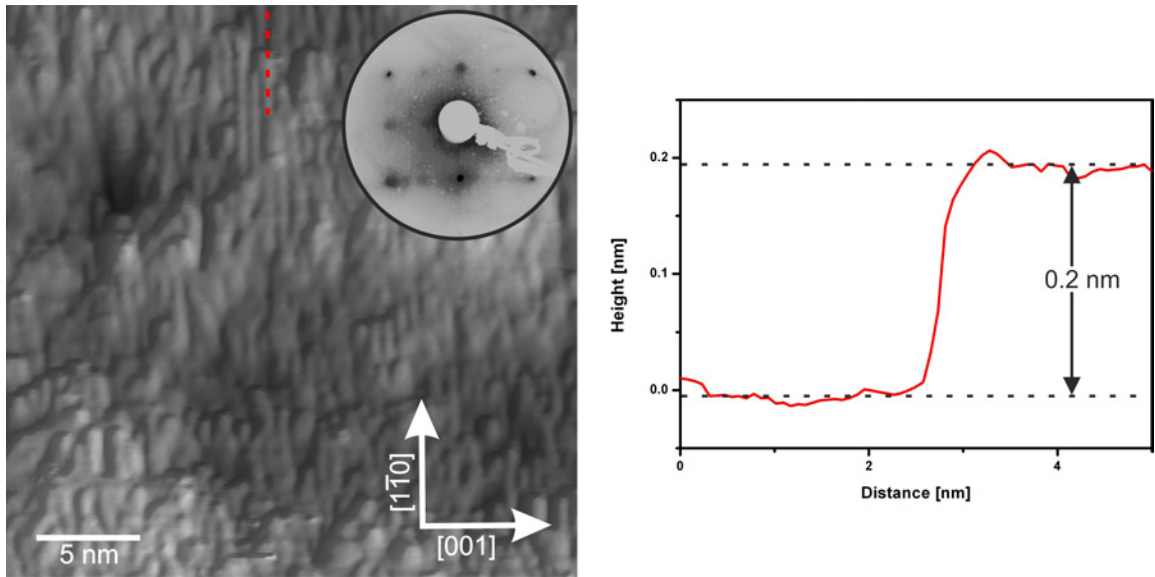


Figure 6.3: Left: Surface morphology of 28 ML Fe<sub>3</sub>Si/GaAs(110) as measured by STM ( $I = 0.4$  nA,  $U = 1.6$  V). The dashed red line indicates the shift of the visible atomic rows between adjacent layers. The LEED pattern of the surface can be seen in the inset ( $E = 91$  eV). Right: The STM linescan measured along the dashed red line in the STM image reveals a step height of approximately 0.2 nm.

The diffraction spots shown in the inset of figure 6.3 in the LEED pattern imply a rectangular atomic arrangement similar to the unit cell of the (110) surface of GaAs. It is striking that every other diffraction spot is only faintly visible. This may be ascribed to 3D effects. Compared to the large atomically flat terraces of the Fe<sub>3</sub>Si/GaAs(001) surface, scattering of electrons from different layers must be taken into account. Also, as was already mentioned, the distance between two adjacent layers has decreased. Considering that the electrons at the employed LEED energies have a penetration depth of approximately 0.5 nm [Hen94] which is large than the above-mentioned RMS roughness, the effective reciprocal lattice for LEED can no longer be simplified as the array of rods shown in figure 3.6. The result are the alternating intensities observed in the diffraction spots.

### 6.2.2 Atomic arrangement

Figure 6.4 shows the atomic arrangement of the topmost two layers of  $\text{Fe}_3\text{Si}(1\bar{1}0)$  in the unreconstructed case. The rectangular unit cell is bordered by a dashed yellow line. It is noteworthy that other than for  $\text{Fe}_3\text{Si}(001)$  the layers are not alternating Fe-Fe and Fe-Si layers but stoichiometric. The unit cell contains two Fe(A,C), one Fe(B) and one Si atom. The arrows along the  $[001]$  and the  $[1\bar{1}0]$  directions with dashed black lines point out that there is a shift of the atomic Fe(B) and Si rows from one layer to the next. This shift amounts to  $\frac{\sqrt{2}}{4}a$  for atomic rows along the  $[001]$  direction and  $\frac{a}{2}$  for atomic rows along the  $[1\bar{1}0]$  direction. Such a displacement would not be observable for the Fe(A,C) species along the considered directions.

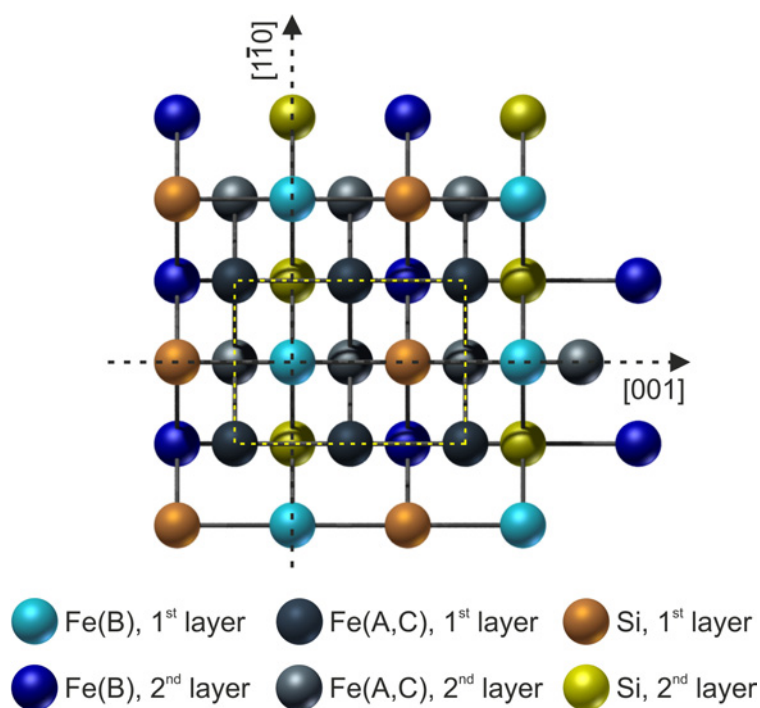


Figure 6.4: Atomic arrangement of the topmost two layers of  $\text{Fe}_3\text{Si}(1\bar{1}0)$ . The dotted yellow rectangle points out the unit cell. The dotted black lines illustrate atomic rows of Fe(B) in the first layer along the  $[001]$  and the  $[1\bar{1}0]$  directions and their displacement for adjacent layers.

The STM data as indicated by the dashed red line in figure 6.3 point out that such a shift from layer to layer can indeed be observed. However, like in the case of  $\text{Fe}_3\text{Si}/\text{GaAs}(001)$ , the question remains whether it is the Fe(B) or the Si species that is imaged.

The LEED image of the  $\text{Fe}_3\text{Si}$  surface already indicated a rectangular arrangement of the unit cell with the same orientation as that of the  $\text{GaAs}(1\bar{1}0)$  substrate. Comparable distances of the diffraction spots at similar electron energies also imply that the substrate and adsorbate lattice constants are approximately the same. This is corroborated by atomic scale STM scans such as shown on the left hand side of figure 6.5. For a better visualiza-

tion, the STM data is represented in a 3D view with a slightly tilted height profile. Atomic rows along the  $[001]$  and the  $[1\bar{1}0]$  directions are resolved. The corresponding linescans that were extracted after applying a low pass filter are shown on the right hand side of figure 6.5. The lattice constants obtained after averaging over several linescans amount to  $(0.569 \pm 0.007)$  nm for the  $[001]$  direction and  $(0.405 \pm 0.011)$  nm for the  $[1\bar{1}0]$  direction. This is in good agreement with the lateral dimensions of the unit cell of  $(110)$  oriented Fe<sub>3</sub>Si.

In summary, the STM and LEED data point out an epitaxial relation between the substrate and the adsorbate of  $(110)[001]\text{GaAs}|| (110)[001]\text{Fe}_3\text{Si}$  or, in other words, that the crystallographic orientation of the GaAs(110) substrate is sustained by the Fe<sub>3</sub>Si adsorbate layer.

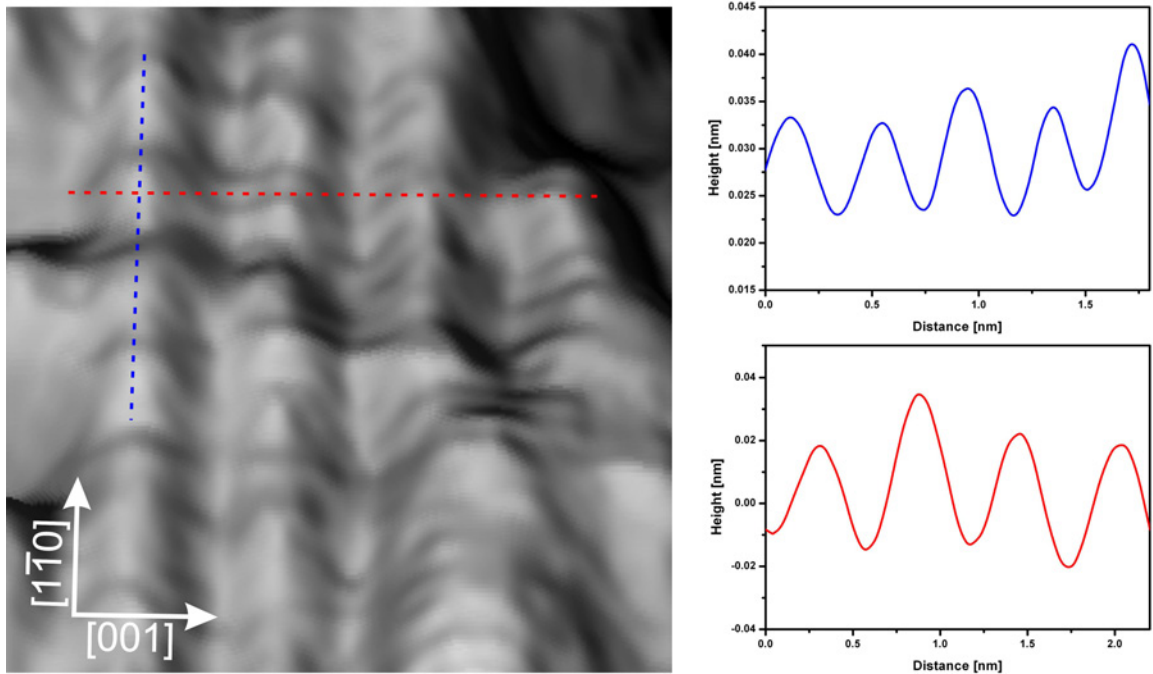


Figure 6.5: Left: 3D view of the atomic arrangement at the Fe<sub>3</sub>Si(110) surface on the basis of STM data ( $I = 0.4$  nA,  $U = 1.6$  V). For a better visualization the height profile was tilted by  $20^\circ$  around the  $[001]$  direction which results in a slight distortion along the  $[1\bar{1}0]$  direction. Right: STM linescans along the  $[001]$  and the  $[1\bar{1}0]$  directions after applying a low pass filter.

### 6.3 Magnetic characterization

The magnetic behaviour of Fe<sub>3</sub>Si/GaAs(110) samples was determined in situ by means of the UHV MOKE setup. The first sample analyzed in this way was the 28 ML Fe<sub>3</sub>Si/GaAs(110) sample the structural properties of which were considered in the preceding section. Figure 6.6 shows hysteresis loops that were measured along the  $[001]$ ,

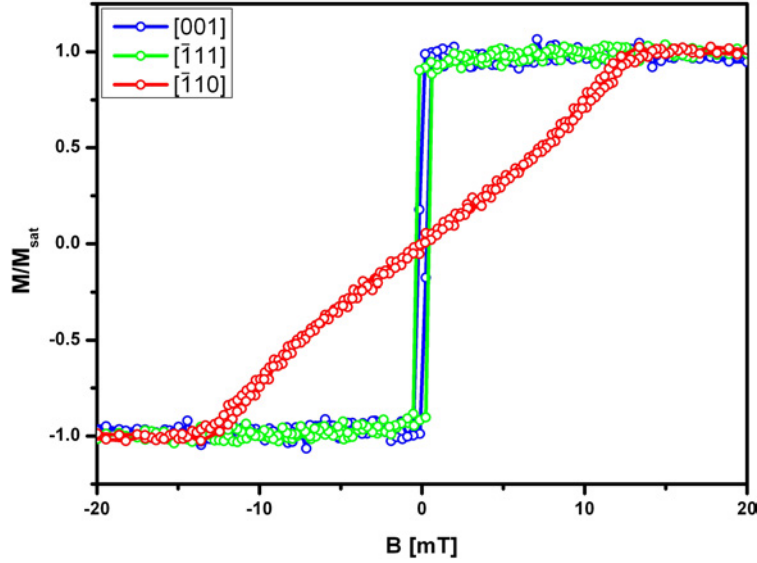


Figure 6.6: Hysteresis loops measured along selected crystallographic directions of 28 ML  $\text{Fe}_3\text{Si}/\text{GaAs}(1\ 1\ 0)$  by in situ MOKE.

the  $[\bar{1}\ 1\ 1]$  and the  $[\bar{1}\ 1\ 0]$  directions. As was the case for  $\text{Fe}_3\text{Si}/\text{GaAs}(001)$  the coercive fields are nearly isotropic. However, they are found to be even decreased down to 0.3 mT. As mentioned earlier, small values for  $H_c$  are an indication for highly ordered  $\text{Fe}_3\text{Si}$ . The  $[001]$  and the  $[\bar{1}\ 1\ 0]$  direction which are mutually perpendicular represent the magnetic easy and the hard axes, respectively. The  $[\bar{1}\ 1\ 1]$  direction is an intermediate axis. It is remarkable that the hard axis considered here exhibits a significantly larger saturation field compared to all  $\text{Fe}_3\text{Si}/\text{GaAs}(001)$  samples with comparable layer thicknesses. A similar behaviour was only observed along the  $[1\ 1\ 0]$  direction for 5 ML  $\text{Fe}_3\text{Si}/\text{GaAs}(001)$ . As a result, the hysteresis loop appears almost closed and thus completely reversible which implies a remagnetization process that is based on domain rotation. These angular dependent hysteresis loops indicate a uniaxial anisotropy. Considering the polar plot for the  $(1\ 1\ 0)$  cross section of the magnetocrystalline anisotropy energy for cubic systems as shown in figure 2.4 and the thickness at which the magnetocrystalline anisotropy begins to dominate for  $\text{Fe}_3\text{Si}/\text{GaAs}(001)$  this behaviour is unexpected. The  $[001]$  direction complies with the magnetocrystalline anisotropy but due to spin-orbit coupling the  $[\bar{1}\ 1\ 1]$  direction should be a hard axis while the  $[\bar{1}\ 1\ 0]$  direction should be an intermediate axis. It can be assumed that the structure of the  $\text{GaAs}(001)$  surface has a more sustainable effect on the UMA in terms of the layers thickness. The underlying mechanism may be the magnetoelastic anisotropy. Similar to  $\text{Fe}/\text{InAs}(001)-(4 \times 2)$  where an anisotropic relaxation of the Fe atoms could be observed due to their higher mobility between the InAs dimer rows of the reconstruction [Xu00], the reduction of tensile stress of the  $\text{Fe}_3\text{Si}$  layer might preferentially occur between the atomic rows oriented along the  $[1\ \bar{1}\ 0]$  direction at the  $\text{GaAs}(1\ 1\ 0)$  surface

shown on the right hand side of figure 6.2. In the case of Fe, a magnetization along the axis of tensile stress is favoured. Concerning Fe<sub>3</sub>Si, the elements  $\sigma_{ij}$  of the stress tensor cannot be found in literature. However, the saturation values  $\lambda_{100}$  and  $\lambda_{111}$  for magnetostriction, which describes the inverse effect of the magnetoelastic anisotropy (see section 2.2.1), determined in [Hal58] indicate a change of sign with increasing Si content<sup>2</sup>. Assuming that the relaxation indeed occurs along the  $[1\bar{1}0]$  direction and taking into account that  $\eta < 0$  and that the relative length changes for Fe<sub>3</sub>Si/GaAs are therefore positive this contradicts the orientation of the uniaxial magnetic anisotropy observed here. On the other hand, the tensile stress for Fe<sub>3</sub>Si/GaAs should only be small due to the low lattice mismatch of merely 0.2%. Therefore, the origin of the UMA may be attributed to other effects. These may be a shape anisotropy as the STM data in figure 6.3 exhibits a small elongation in the Fe<sub>3</sub>Si surface morphology along the  $[1\bar{1}0]$  direction or an anisotropic bonding as was already suggested for Fe<sub>3</sub>Si/GaAs(001).

For comparison, in situ MOKE measurements were also performed on a sample with a substantially higher coverage of 112 ML Fe<sub>3</sub>Si on GaAs(110). The composition of this sample as determined by RBS shows a silicon content of  $(21.7 \pm 1.2)$  at.%. Although this implies a small Si deficit the iron silicide layer can still be considered to be well in the D0<sub>3</sub> structure range (see figure 1.2). The hysteresis loops for the low-indexed crystallographic directions  $[001]$ ,  $[\bar{1}11]$  and  $[\bar{1}10]$  are shown in figure 6.7. While the  $[001]$  direction remains the easy

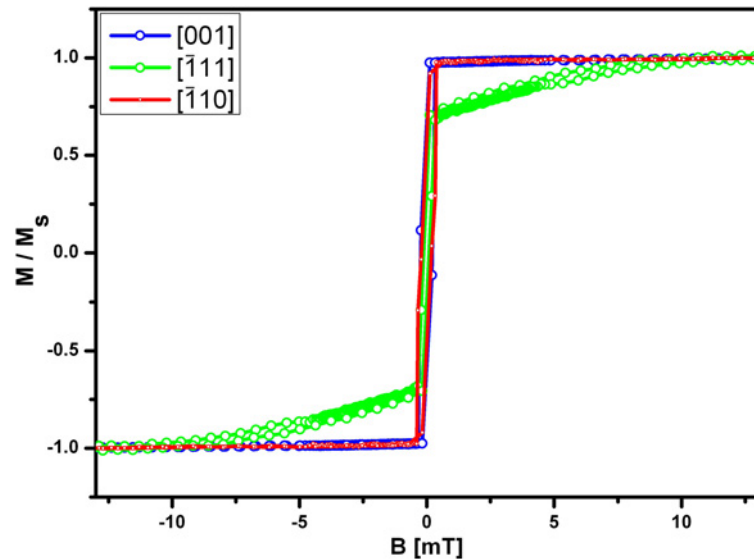


Figure 6.7: Hysteresis loops of 112 ML Fe<sub>3</sub>Si/GaAs(110) measured along selected crystallographic directions by in situ MOKE.

<sup>2</sup> $\lambda_{111}$  changes sign at a silicon content of about 4% while  $\lambda_{100}$  changes sign at approximately 6% silicon content.

axis the hard axis is now oriented along the  $[\bar{1}11]$  direction and the  $[\bar{1}10]$  direction becomes the intermediate axis which is qualitatively in agreement with the magnetocrystalline anisotropy. However, it cannot be ruled out that slight deviations from the stoichiometric composition of  $\text{Fe}_3\text{Si}$  can influence the amount of the contribution from the uniaxial magnetic anisotropy. This is due to the fact that the lattice constant of  $\text{Fe}_3\text{Si}$  and therefore also the misfit parameter  $\eta$  for  $\text{Fe}_3\text{Si}/\text{GaAs}$  depend on the exact composition [Her03]. Indeed, in the small region from a silicon content of 25 at.% at stoichiometry down to the above mentioned  $(21.7 \pm 1.2)$  at.% silicon content  $\eta$  already changes its sign. On the other hand, it is believed that the amount of silicon governs the suppression of the uniaxial-like bonding structure at the interface which determines the UMA [Len05]. In order to make clearer statements about the nature and magnitude of the UMA, a systematic study involving a greater number of samples and a quantitative analysis by methods like FMR needs to be done. It might be possible to separate the influence of composition on the lattice constant and on the effect on the bonding structure at the interface by providing substrates with lattice parameters varying around the lattice constant of stoichiometric  $\text{Fe}_3\text{Si}$ . This could be done by the fabrication of  $\text{GaAs}_x\text{P}_{1-x}$  buffer layers which can be grown epitaxially on GaAs and GaP as shown in [Art69].

The anisotropic behaviour of the 28 ML and the 112 ML sample determined from the normalized remanent magnetizations is summarized in figure 6.8. This points out that while the  $[001]$  direction specifies the easy direction for both samples additional bulges appear along the  $\langle\bar{1}10\rangle$  directions due to the magnetocrystalline anisotropy which dominates at higher coverage.

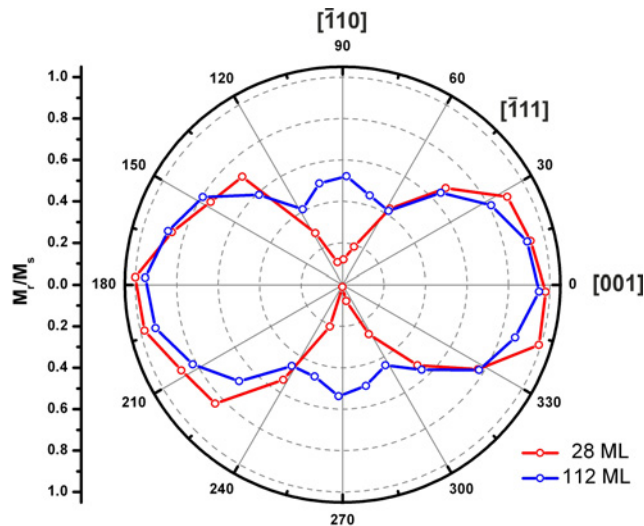


Figure 6.8: Plots of the angular dependent normalized remanences for 28 and 112 monolayers of  $\text{Fe}_3\text{Si}/\text{GaAs}(110)$ . While the anisotropy at a thickness of 28 ML is purely uniaxial contributions of the magnetocrystalline anisotropy can be observed at a thickness of 112 ML.

In order to determine the magnetic moment, Fe<sub>3</sub>Si/GaAs(110) samples with film thicknesses of 56 and 112 ML were measured with SQUID magnetometry. The data was evaluated according to the procedure described in section 5.4.2. The magnetic moment per atom at a thickness of 56 monolayers amounts to  $(1.06 \pm 0.20) \mu_B$  at room temperature and  $(1.13 \pm 0.22) \mu_B$  at 5 K. At a thickness of 112 ML the magnetic moment per atom is found to be reduced to  $(0.76 \pm 0.15) \mu_B$  at room temperature and  $(0.90 \pm 0.18) \mu_B$  at 5 K. While the magnetic moments at a thickness of 56 monolayers seem to be well in agreement with the bulk values of  $1.107 \mu_B$  at room temperature and  $1.175 \mu_B$  at 6.5 K (see section 5.4.2) the decrease at a thickness of 112 monolayers might again be ascribed to a degradation of crystalline quality at higher coverage.

## Chapter 7

# Summary, conclusion and outlook

Motivated by the lack of microscopic data and by the possible relevance for spintronic applications the centrepiece of this thesis presents a multitechnique experimental study of ultrathin layers of  $\text{Fe}_3\text{Si}$  epitaxially grown on  $\text{GaAs}(001)$  and  $\text{GaAs}(110)$ . Emphasis was laid on the extraction of structural and magnetic properties between which, where possible, correlations were elaborated.

Apart from the analysis of  $\text{Fe}_3\text{Si}/\text{GaAs}$ , a substantial amount of work done within the framework of this thesis was dedicated to modifications of the experimental setup as described in section 4.2. For the fabrication of  $\text{Fe}_3\text{Si}$  layers a stable silicon MBE source was build up on the basis of an electron beam evaporator. Both hardware and software were developed for attaining reproducible compositions of the iron silicide. In this context, the use of secondary substrates consisting of  $\text{MgO}$  for the determination of the exact composition by means of RBS was established. Although the resulting MBE setup allows the fabrication of iron silicide layers with arbitrary compositions, the analyses presented in this work are restricted to films close to stoichiometric  $\text{Fe}_3\text{Si}$ . Further modifications were done by enhancing the UHV system with a flow cryostat that can be used both for MOKE measurements as well as for film growth at low temperatures. Due to the fact that one part of the UHV chamber needed to be reconstructed in order to accommodate the flow cryostat, a revision of the MOKE setup associated with the UHV chamber was done at the same time. As a result, the revised MOKE setup provides a stronger electromagnet, easier sample transfer and sample alignment and, due to an increase of the angle of incidence of the MOKE laser beam onto the sample, an increased sensitivity to the magneto-optical Kerr effect. First experiments involving the use of the cryostat were shown in section 5.4.1 where the shape parameter of the temperature dependent magnetization according to the semi-empirical description by Kuz'min [Kuz05, Kuz06] was determined for a 40 ML  $\text{Fe}_3\text{Si}/\text{GaAs}(001)$  sample. The current setup allows MBE growth and MOKE measurement at sample temperatures down to 96 K when operating the cryostat with liquid nitrogen. According to the considerations in section 4.2.2 it can be estimated that even without the use of cryogenic shields temperatures of approximately 30 K can be reached by using liquid helium as the

coolant. This is well below the Curie temperature of many ferromagnets consisting of pure elements such as gadolinium, terbium or dysprosium as was mentioned in section 2.2.1. Moreover, this goes well below the Curie temperatures of diluted magnetic semiconductors such as  $\text{Ga}_{1-x}\text{Mn}_x\text{As}$  for which Curie temperatures as high as 173 K have already been reported [Jun05]. DMS represent an alternative way for spin transport in semiconductors as described in reviews like [Ohn98]. The setup could furthermore be used for the growth and magnetic characterization of other FM/SC combinations such as Fe/GaAs at low temperatures. Like for  $\text{Fe}_3\text{Si}/\text{GaAs}$  a quasi layerwise growth could be established which in turn might alter the anisotropic magnetic behaviour [Win08].

The main part of this thesis described the structural and magnetic properties of  $\text{Fe}_3\text{Si}/\text{GaAs}(001)$  with varying adsorbate layer thicknesses. The starting point for the structural analysis was the optimization of the layer morphology as a function of the growth parameters and post annealing processes under the observation of STM and LEED. This was motivated by the large range of growth parameters that can be found in literature (see section 1.1) and by the lack of microscopic data. In the literature it was already indicated by Monte Carlo simulations [Kag09] that a surface morphology corresponding to a pseudo Frank-van der Merwe growth mode can be achieved for layer thicknesses of above approximately 10 ML. However, at least in terms of the atomic ordering at the surface, it is found that this cannot be performed in a one-step process. On the one hand, the thermal energy at lower growth temperatures is insufficient to induce atomic ordering. On the other hand, the deposition at elevated growth temperatures leads to a layer morphology in which trenches down to the substrate level persist up to higher film thicknesses. The STM analysis points out that the layer morphology can be optimized by post-annealing the samples at 300 °C following the film growth where a deposition rate of  $0.1 \text{ nm min}^{-1}$  and a growth temperature of 200 °C were found to be most suitable. The study of the influence of post-annealing also revealed that although the  $\text{D0}_3$  structure of  $\text{Fe}_3\text{Si}/\text{GaAs}(001)$  was shown to be stable up to 425 °C [Her05] an incipient break-up of the  $\text{Fe}_3\text{Si}$  layer can already be observed at 400 °C or even below. After post annealing at an even increased temperature of 500 °C further breaking up of the layer can be observed alongside the formation of two different types of alloying between the substrate and the adsorbate.

By means of STM, the surface atomic structure of  $\text{Fe}_3\text{Si}/\text{GaAs}(001)$  could be imaged in real space for the first time. The microscopic data is in agreement with the  $\text{D0}_3$  structure of  $\text{Fe}_3\text{Si}$  but it also points out that regardless of the applied STM bias voltage always one and the same sublattice is imaged. This sublattice is tentatively assigned to the Si species as the analyses of different samples with slight compositional variations lead to this assumption. Up to now, there remains a discrepancy with STM simulations in terms of a contrast inversion which was discussed in section 5.3.1. The atomic scale images were furthermore used to assign surface defects which were previously reported in a study based on XRD measurements [Kag08]. Besides the obvious appearance of antisite defects the STM data points out that the majority of disorder must be ascribed to faulted stacking sequences of

larger areas which leads to a splitting of the iron silicide into bcc iron and B2 Fe-Si unit cells instead of the D0<sub>3</sub> structure.

While the STM study of the system Fe<sub>3</sub>Si/GaAs(001) was clearly motivated by the lack of real space data there were also different incentives for its magnetic characterization. For one, it was essential to obtain a magnetic characterization of the same samples of which the structural properties were considered in order to make reliable statements about the correlations of these properties. Moreover, despite the fact that a lot of information about the magnetic behaviour of Fe<sub>3</sub>Si/GaAs(001) can be gathered from literature as summarized in section 1.1 many open-ended questions such as the origin of the uniaxial magnetic anisotropy or the thickness dependent magnetic moment remain up to date. The conclusions that are drawn in this thesis do not claim to ultimately answer these questions but to provide information based on the connections that can be established between structural and magnetic properties.

In situ MOKE measurements were used to obtain hysteresis loops and anisotropy plots on the basis of the angular dependent normalized magnetic remanences. Beyond that, the in situ MOKE measurements were able to point out that the method used for capping iron layers [Elm88, Spo04, Urb05], i. e. the deposition of Ag and Au layers with thicknesses of 2.5 nm, respectively, can also be applied to Fe<sub>3</sub>Si layers as no notable influence on the hysteresis loops and on the anisotropy plots could be observed. More quantitative data could be obtained from ex situ SQUID magnetometry and FMR measurements. The average magnetic moment per atom of the Fe<sub>3</sub>Si layers is found to be enhanced above the bulk value below thicknesses of 40 ML. A peak value of  $(2.14 \pm 0.2) \mu_B$  at room temperature is found at a thickness of 5 ML. While it is possible that part of this increase can be ascribed to surface and interface anisotropies the STM data support an increase caused by unquenched orbital moments at the surface due to the significantly higher densities of step edges at low coverage. It was furthermore possible to determine the thickness dependences of the magnetic anisotropy constants. The experimental data confirmed that the overall magnetic anisotropy is a superposition of the magnetocrystalline and a uniaxial magnetic anisotropy. Similar to [Her08] a reorientation of the UMA is observed. This points out that there is a finite volume contribution to the UMA the origin of which, however, still remains unknown. For thicker films above 40 ML the magnetocrystalline anisotropy constant  $K_1$  reaches a bulk-like value.

One point of interest in this work consisted of the structural and magnetic properties at a coverage both below the onset of ferromagnetism and below the thicknesses at which the growth proceeds quasi layerwise. Here, the experimental data point out that the 3D island-wise growth is strongly linked to the magnetic behaviour which is comparable to a system of superparamagnetic nanoparticles. In fact, the superspin derived from a Langevin fit to the magnetization loop can clearly be brought into agreement with the average magnetic moment per atom and the size of the clusters as measured by STM (see section 5.5.1).

In comparison to Fe<sub>3</sub>Si/GaAs(001) of which many aspects have been studied to a large

extent the structural and magnetic data on  $\text{Fe}_3\text{Si}/\text{GaAs}(110)$  represent the first experimental work that has been done so far. The growth parameters and the post annealing procedure which resulted in an optimized layer morphology in the case of  $\text{Fe}_3\text{Si}/\text{GaAs}(001)$  were also applied to  $\text{Fe}_3\text{Si}/\text{GaAs}(110)$ . At a film thickness of 56 ML, where according to STM data one monolayer can be appointed as approximately 0.2 nm, the closest possible spacing between the (110) oriented atomic layers, the  $\text{Fe}_3\text{Si}$  film covers the substrate entirely. However, compared to  $\text{Fe}_3\text{Si}/\text{GaAs}(001)$  the surface is found to be rougher. STM and LEED data could furthermore determine that the crystallographic orientation of the substrate is sustained by the adsorbate, hence  $(110)[001]\text{GaAs}|| (110)[001]\text{Fe}_3\text{Si}$ . In situ MOKE measurements point out that at a thickness of 28 ML the overall magnetic anisotropy of  $\text{Fe}_3\text{Si}/\text{GaAs}(110)$  is strongly dominated by a uniaxial magnetic anisotropy while at a thickness of 112 ML it corresponds to the magnetocrystalline anisotropy. For low coverage, theoretical considerations determined an augmented average magnetic moment per atom and predicted that the bulk magnetic moment would be approached for higher thicknesses [Her08a]. The latter could be verified by SQUID magnetometry measurements which at a thickness of 56 ML yielded an average magnetic moment per atom of  $(1.06 \pm 0.20) \mu_B$  at room temperature.

In summary, structural and magnetic properties of  $\text{Fe}_3\text{Si}/\text{GaAs}$  have been investigated upon establishing the technical requirements by modifying the experimental setup. Due to the fact that the series of experiments such as the optimization of the layer morphology or the thickness dependent analyses of structural and magnetic properties were time-consuming there remain projects that could not be accomplished within the scope of this thesis and which are therefore listed here as an outlook.

Throughout this work the influence of the substrate surface reconstructions in the case of  $\text{GaAs}(001)$  was neglected. Although it can be assumed that this is appropriate for thicker films it cannot be ruled out that influences on the structural and magnetic properties might be observed. This could be studied by varying the substrate surface reconstructions as a result of different preparation methods.

The magnetic analyses showed that a uniaxial anisotropy can be observed both for  $\text{Fe}_3\text{Si}/\text{GaAs}(001)$  and  $\text{Fe}_3\text{Si}/\text{GaAs}(110)$ . Under the consideration of literature [Len05] it can be summarized that the origin of the UMA might be ascribed to different mechanisms, namely the magnetoelastic anisotropy and anisotropic bonding at the interface the magnitude of which could be influenced by the exact silicon content of the  $\text{Fe}_3\text{Si}$  adsorbate layers. This could be systematically investigated by using substrates with variable lattice constants like  $\text{GaAs}_x\text{P}_{1-x}$  as mentioned in section 6.3 and by varying the iron silicide composition.

Regarding  $\text{Fe}_3\text{Si}/\text{GaAs}(110)$ , clearly a more detailed and especially a quantitative magnetic analysis needs to be done in order to obtain a comprehensive description. Furthermore, the growth parameters were directly transferred from the  $\text{Fe}_3\text{Si}/\text{GaAs}(001)$  samples. Considering that the diffusion barrier of the (110) oriented substrates is most likely to differ

from the (100) oriented substrates an independent optimization of the growth parameters is required for Fe<sub>3</sub>Si/GaAs(110).

In the introduction it was already mentioned that the system Fe<sub>3</sub>Si/GaAs is a promising candidate for spintronic applications, e. g. due to the quasi half-metallic behaviour of the Heusler alloy Fe<sub>3</sub>Si. In total, the present work confirms this. The thickness dependent magnetic moments indicate a sharp interface with the substrate or, in other words, that magnetically dead layers which would counteract spin injection are not likely to be formed. Fe<sub>3</sub>Si layers were furthermore proven to be thermally stable up to approximately 400 °C. It was also shown in this thesis that under the appropriate choice of growth parameters atomically flat layers of Fe<sub>3</sub>Si can be grown on GaAs(001) which is a good premise to create multilayer systems for technological applications. Although the surface was found to exhibit a slightly higher roughness it could be shown that closed layers of Fe<sub>3</sub>Si can also be grown on GaAs(110) where the epitaxial relation is sustained across the interface. The magnetic anisotropy, which as in the case of Fe<sub>3</sub>Si/GaAs(001) is a superposition of the magnetocrystalline anisotropy and a uniaxial magnetic anisotropy, can be tailored by changing the film thickness of the ferromagnet.



# Bibliography

- [Arg55] P. N. Argyres, Phys. Rev. B **97**, 334 - 345, 1955
- [Art69] J. R. Arthur, J. J. LePore, J. Vac. Sci. Technol. **6**, 545 - 548, 1969
- [Bai88] M. N. Baibich, J. M. Broto, A. Fert, F. Nguyen Van Dau, F. Petroff, P. Eitenne, G. Creuzet, A. Friederich, J. Chazelas, Phys. Rev. Lett. **61**, 2472 - 2475, 1988
- [Bar61] J. Bardeen, Phys. Rev. Lett. **6**, 57 - 59, 1961
- [Bar09] H. Bardenhagen: *Vektor-MOKE-Untersuchungen an epitaktischen Eisenschichten*, Diploma thesis, Universität Osnabrück, 2009
- [Bar11] I. Barsukov, S. Mankovsky, A. Rubacheva, R. Meckenstock, D. Spoddig, J. Lindner, N. Melnichak, B. Krumme, S. I. Makarov, H. Wende, H. Ebert, M. Farle, Phys. Rev. B **84**, 180405, 2011
- [Bar12] I. Barsukov, P. Landeros, R. Meckenstock, J. Linder, D. Spoddig, Z.-A. Li, B. Krumme, H. Wende, D. L. Mills, M. Farle, Phys. Rev. B **85**, 014420 (2012)
- [Bat87] I. P. Batra, N. García, H. Rohrer, H. Salemink, E. Stoll, S. Ciraci, Surf. Sci. **181**, 126 - 138, 1987
- [Bau58] E. Bauer, Z. Kristallogr. **110**, 372 - 394, 1958
- [Bau82] E. Bauer, Appl. Surf. Sci. **11/12**, 479 - 494, 1982
- [Ber92] Bergmann, Schäfer: *Lehrbuch der Experimentalphysik, Band 6, Festkörper*, Walter de Gruyter, 1992
- [Ber10] K.-H. Bernhardt: *Vacuum Technology Compendium*, Pfeiffer Vacuum GmbH, 2010
- [Bie90] D. K. Biegelsen, R. D. Bringans, J. E. Northrup, L.-E. Swartz, Phys. Rev. B **41**, 5701 - 5706, 1990
- [Bin89] G. Binasch, P. Grünberg, F. Saurenbach, W. Zinn, Phys. Rev. B **39**, 4828 - 4830, 1989

- [Blu01] S. Blundell: *Magnetism in Condensed Matter*, Oxford University Press, 2001
- [Bre11] A. Brennscheid: *Magnetkraftmikroskopie an lateral strukturierten magnetischen Dipolgittern: Ummagnetisierungsprozesse, Ordnung und Frustration in Honigwabenstrukturen*, PhD thesis, Ruhr-Universität Bochum, 2011
- [Bri97] M. Brinkmann: *Supraleitung und normaleitende elektrische Transporteigenschaften von elektrondotierten Hoch- $T_C$ -Supraleiter-Einkristallen*, PhD thesis, Ruhr-Universität Bochum, 1997
- [Brü13] F. Brüsing: *Magnetization reversal of laterally structured multilayers*, PhD thesis, Ruhr-Universität Bochum, 2013
- [Buc04] W. Buckel, R. Kleiner: *Supraleitung*, Wiley-VCH, 2004
- [Bus97] H. Busse, J. Kandler, B. Eltester, K. Wandelt, G. R. Castro, J. J. Hinarejos, P. Segovia, J. Chrost, E. G. Michel, R. Miranda, Surf. Sci. **381**, 133 - 141, 1997
- [Cal65] E. Callen, H. Callen, J. Appl. Phys. **36**, 1140 - 1142, 1965
- [Che93] J. Chen: *Introduction to Scanning Tunneling Microscopy*, Oxford University Press, 1993
- [Dum02] M. Dumm, B. Uhl, M. Zöfl, W. Kipferl, G. Bayreuther, J. Appl. Phys. **91**, 8763 - 8765, 2002
- [Dys56] F. J. Dyson, Phys. Rev. **102**, 1230 - 1244, 1956
- [Eim09] J. Li, M.-S. Lee, W. He, B. Redeker, A. Remhof, E. Amaladass, C. Hassel, T. Eimüller, Rev. Sci. Instr. **80**, 073703, 2009
- [Elm88] H. J. Elmers, U. Gradmann, J. Appl. Phys. **64**, 5328 - 5330, 1988
- [Far46] M. Faraday, Phil. Trans. Roy. Soc. **136** 1, 1846
- [Far98] M. Farle, Rep. Prog. Phys. **61**, 755 - 826, 1998
- [Fli00] T. Fließbach: *Quantenmechanik*, Spektrum Akademischer Verlag, 2000
- [Fra05] M. Fraune: *Magnetische Anisotropie und Spintransport in magnetoelektronischen Schichtsystemen und Nanostrukturen*, PhD thesis, RWTH Aachen, 2005
- [God08] C. Godde, S. Noor, C. Urban, U. Köhler, Surf. Sci. **602**, 3343 - 3351, 2008
- [Haf07] J. Hafner, D. Spišák, Phys. Rev. B **75**, 195411, 2007
- [Hal58] R. C. Hall, J. Appl. Phys. **30**, 816 - 819, 1958
- [Hei28] W. Heisenberg, Zeitschrift für Physik **49**, 619 - 636, 1928

- [Hen94] M. Henzler, W. Göpel: *Oberflächenphysik des Festkörpers*, Teubner Studienbücher, 1994
- [Her03] J. Herfort, H.-P. Schönherr, K. H. Ploog, Appl. Phys. Lett. **83**, 3912 - 3914, 2003
- [Her04] J. Herfort, H.-P. Schönherr, K.-J. Friedland, K. H. Ploog, J. Vac. Sci. Technol. B **22**, 2073 - 2078, 2004
- [Her05] J. Herfort, H.-P. Schönherr, A. Kawaharazuka, M. Ramsteiner, K. H. Ploog, J. Cryst. Growth **278**, 666 - 670, 2005
- [Her08] J. Herfort, H.-P. Schönherr, B. Jenichen, J. Appl. Phys. **103**, 07B506, 2008
- [Her08a] H. C. Herper, P. Entel, Philos. Mag. **88**, 2699 - 2707, 2008
- [Hin76] W. A. Hines, A. H. Menotti, J. O. Budnick, T. J. Burch, T. Litrenta, V. Niculescu, K. Raj, Phys. Rev. B **13**, 4060 - 4068, 1976
- [Hol07] M. Holub, P. Bhattacharya, J. Phys. D: Appl. Phys. **40**, R179 - R203, 2007
- [Hon57] R. E. Honig, RCA Rev. **18**, 195 (1957)
- [Hub98] A. Huber, R. Schäfer: *Magnetic Domains*, Springer-Verlag, Berlin Heidelberg New York, 1998
- [Ich01] A. Ichimiya, Y. Nishikawa, M. Uchimiya, Surf. Sci. **493**, 232 - 237, 2001
- [Ion05a] A. Ionescu, C. A. F. Vaz, T. Trypiniotis, C. M. Gürtler, M. E. Vickers, H. García-Miquel, J. A. C. Bland, J. Magn. Magn. Mater. **286**, 72 - 76, 2005
- [Ion05b] A. Ionescu, C. A. F. Vaz, T. Trypiniotis, C. M. Gürtler, H. García-Miquel, J. A. C. Bland, M. E. Vickers, R. M. Dalgliesh, S. Langridge, Y. Bugoslavsky, Y. Miyoshi, L. F. Cohen, K. R. A. Ziebeck, Phys. Rev. B **71**, 094401, 2005
- [Jen05] B. Jenichen, V. M. Kaganer, J. Herfort, D. K. Satapathy, H. P. Schönherr, W. Braun, K. H. Ploog, Phys. Rev. B **72**, 075329, 2005
- [Jen07] B. Jenichen, V. M. Kaganer, W. Braun, J. Herfort, R. Shayduk, K. H. Ploog, Thin Solid Films **515**, 5611 - 5614, 2007
- [Jon41] R. C. Jones, J. Opt. Soc. Am. **31**, 488 - 493, 1941
- [Jul75] M. Julliere, Phys. Lett. **54A**, 225 - 226, 1975
- [Jun05] T. Jungwirth, K. Y. Wang, J. Mašek, K. W. Edmonds, Jürgen König, Jairo Sinova, M. Polini, N. A. Goncharuk, A. H. MacDonald, M. Sawicki, A. W. Rushforth, R. P. Campion, L. X. Zhao, C. T. Foxon, B. L. Gallagher, Phys. Rev. B **72**, 165204, 2005

- [Kag08] V. M. Kaganer, B. Jenichen, R. Shayduk, W. Braun, Phys. Rev. B **77**, 125325, 2008
- [Kag09] V. M. Kaganer, B. Jenichen, R. Shayduk, W. Braun, H. Riechert, Phys. Rev. Lett. **102**, 016103, 2009
- [Kat66] H. Katsuraki, N. Achiwa, J. Phys. Soc. Jpn. **21**, 2238 - 2243, 1966
- [Kaw04] A. Kawaharazuka, M. Ramsteiner, J. Herfort, H.-P. Schönherr, H. Kostial, K. H. Ploog, Appl. Phys. Lett. **85**, 3492 - 3494, 2004
- [Kei82] K. Keil, J. L. Berkley, L. H. Fuchs, Am. Mineral. **67**, 126 - 131, 1982
- [Ker99] J. Kerr, Phil. Mag. **3**, 321, 1877
- [Kle97] M. Klein, G. Schwitzgebel, Rev. Sci. Instrum. **68**, 3099 - 3103, 1997
- [Kne62] E. Kneller: *Ferromagnetismus*, Springer-Verlag, 1962
- [Kne03] M. Knepe: *Initiale Nukleation bei der Deposition von Eisen auf Silizium und InAs(001)*, PhD thesis, Ruhr-Universität Bochum, 2003
- [Kös56] W. Köster: *Beiträge zur Theorie des Ferromagnetismus und der Magnetisierungskurve*, Springer-Verlag, 1956
- [Kot94] E. Kotai, Nucl. Instr. Meth. B **85**, 588 - 596, 1994
- [Kru09] B. Krumme, C. Weis, H. C. Herper, F. Stromberg, C. Antoniak, A. Warland, E. Schuster, P. Srivastava, M. Walterfang, K. Fauth, J. Minár, H. Ebert, P. Entel, W. Keune, H. Wende, Phys. Rev. B **80**, 144403, 2009
- [Kub82] O. Kubaschewski: *Iron-Binary Phase Diagrams*, Springer-Verlag, 1982
- [Küh01] E. Kühl: *Magnetische Eigenschaften von Eisen auf und in Kupfer und Silber*, PhD thesis, Hamburg, 2001
- [Kuz05] M. D. Kuz'min, Phys. Rev. Lett. **94**, 107204, 2005
- [Kuz06] M. D. Kuz'min, M. Richter, A. N. Yaresko, Phys. Rev. B **73**, 100401, 2006
- [Len05] K. Lenz, E. Kosubek, K. Baberschke, H. Wende, Phys. Rev. B **72**, 144411, 2005
- [Len06] K. Lenz, E. Kosubek, K. Baberschke, J. Herfort, H.-P. Schönherr, K. H. Ploog, phys. stat. sol. (c) **3**, 122 - 125, 2006
- [Li04] C. H. Li, G. Kioseoglou, O. M. J. van 't Erve, A. T. Hanbicki, B. T. Jonker, R. Mallory, M. Yasar, A. Petrou, Appl. Phys. Lett. **85**, 1544 - 1546, 2004

- [Lin02] J. Lindner: *Ferromagnetische Resonanz an ultradünnen magnetischen Einfach- und Mehrfachlagen der 3d-Übergangsmetalle - Statik und Dynamik*, PhD thesis, Freie Universität Berlin, 2002
- [Lub76] A. R. Lubinsky, C. B. Duke, B. W. Lee, P. Mark, Phys. Rev. Lett. **36**, 1058 - 1061, 1976
- [Mar04] M. Marangolo, F. Gustavsson, G. M. Guichar, M. Eddrief, J. Varalda, V. H. Etgens, M. Rivoire, F. Gendron, H. Magnan, D. H. Mosca, J.-M. George, Phys. Rev. B **70**, 134404, 2004
- [Mas82] N. Masud, J. Phys. C: Solid State Phys. **15**, 3209 - 3222, 1982
- [May03] M. Mayer: *Rutherford Backscattering Spectrometry*, Lecture, Max-Planck-Institut für Plasmaphysik, 2003
- [Mes01] D. Meschede: *Gerthsen Physik*, Springer-Verlag, 2001
- [Mue04] G. Müller et al.: *Crystal Growth - From Fundamentals to Technology*, Elsevier B.V., 2004
- [Nag74] H. Nagai, J. Appl. Phys. **45**, 3789 - 3794, 1974
- [Nat01] K. G. Nath, F. Maeda, S. Suzuki, Y. Watanabe, J. Appl. Phys. **90**, 1222 - 1226, 2001
- [Noo07] S. Noor: *Untersuchungen zum magnetooptischen Kerr-Effekt und zur Kerr-Mikroskopie*, Diploma thesis, Ruhr-Universität Bochum, 2007
- [Now10] G. Nowak: *Superconducting Spin Valves Based on Epitaxial Fe/V-Hybrid Thin Film Heterostructures*, PhD thesis, Ruhr-Universität Bochum, 2010
- [Ohn98] H. Ohno, Science **281**, 951 - 956, 1998
- [Ohn99] Y. Ohno, R. Terauchi, T. Adachi, F. Matsukura, H. Ohno, Phys. Rev. Lett. **83**, 4196 - 4199, 1999
- [Özk11] M. S. Özkan: *Strukturelle und magnetische Untersuchungen von Ferromagnetschichten auf Verbindungshalbleitern*, Diploma thesis, Ruhr-Universität Bochum, 2011
- [Pet06] O. Petravic, X. Chen, S. Bedanta, W. Kleemann, S. Sahoo, S. Cardoso, P. P. Freitas, J. Magn. Magn. Mater. **300**, 192 - 197, 2006
- [Pet10] O. Petravic, Superlattices and Microstructures **47**, 569 - 578, 2010
- [Pic75] S. Pickart, T. Litrenta, T. Burch, J. I. Budnick, Phys. Lett. **53A**, 321 - 323, 1975

- [Pol08] S. Polisetty, J. Scheffler, S. Sahoo, Y. Wang, T. Mukherjee, X. He, C. Binek, *Rev. Sci. Instrum.* **79**, 055107, 2008
- [Ras00] E. I. Rashba, *Phys. Rev. B* **62**, R16267 - R16270, 2000
- [Red07] B. Redeker: *Konstruktion und Aufbau eines Femtosekunden-Laser-Mikroskops zur Abbildung ultraschneller Magnetisierungsprozesse sowie zur dreidimensionalen Nanostrukturierung von Polymeren*, Diploma thesis, Technische Fachhochschule Georg Agricola Bochum, 2007
- [Res01] K. Reshöft: *Zeitaufgelöste STM-Untersuchungen zur Silizid- und Metall-Epitaxie der Systeme Fe-, Cu-, Pt/Si(111) und Cu/W(110)*, PhD thesis, Christian-Albrechts-Universität zu Kiel, 2001
- [Res99] M. Respaud, *J. Appl. Phys.* **86**, 556 - 561, 1999
- [Rup02] L. Ruppel, G. Witte, C. Wöll, T. Last, S. F. Fischer, U. Kunze, *Phys. Rev. B* **66**, 245307, 2002
- [Sch99] F. Schäfer: *Die Elementarschritte bei der Diamantabscheidung: Charakterisierung mit Hochtemperatur-Rastertunnelmikroskopie*, PhD thesis, Ruhr-Universität Bochum, 1999
- [Sch01] H.-P. Schönherr, R. Nötzel, W. Ma, K. H. Ploog, *J. Appl. Phys.* **89**, 169 - 173, 2001
- [Sch07] F. Schwabl: *Quantenmechanik*, Springer Verlag, 2007
- [Sch66] R. L. Schwoebel, *J. Appl. Phys.* **37**, 3682 - 3686, 1966
- [Sea79] M. P. Seah, W. A. Dench, *Surf. Interface Anal.* **1**, 2 - 11, 1979
- [Sil67] A. H. Silver, J. E. Zimmerman, *Phys. Rev.* **157**, 317 - 341, 1967
- [Sin04] L. J. Singh, Z. H. Barber, Y. Miyoshi, Y. Bugoslavsky, W. R. Branford, L. F. Cohen, *Appl. Phys. Lett.* **84**, 2367 - 2369, 2004
- [Sou98] R. J. Soulen Jr., J. M. Byers, M. S. Osofsky, B. Nadgorny, T. Ambrose, S. F. Cheng, P. R. Broussard, C. T. Tanaka, J. Nowak, J. S. Modeera, A. Barry, J. M. D. Coey, *Science* **282**, 85 - 88, 1998
- [Spo04] D. Spoddig: *Untersuchung mittels Ferromagnetischer Resonanz an Kobalt, Nickel und Eisen Filmen aus elektrochemischer und molekular epitaktischer Abscheidung*, PhD thesis, Ruhr-Universität Bochum, 2004
- [Sta01] U. Starke, J. Schardt, W. Weiss, W. Meier, C. Polop, P. L. de Andres, K. Heinz, *Europhys. Lett.* **56**, 822 - 828, 2001

- [Ter83] J. Tersoff, D. R. Hamann, Phys. Rev. Lett. **50**, 1998 - 2001, 1983
- [Ter85] J. Tersoff, D. R. Hamann, Phys. Rev. B **31**, 805 - 813, 1985
- [Tis95] M. Tischer, O. Hjortstam, D. Arvanitis, J. Hunter Dunn, F. May, K. Baberschke, J. Trygg, J. M. Wills, B. Johansson, O. Eriksson, Phys. Rev. Lett. **75**, 1602 - 1605, 1995
- [Urb05] C. Urban: *Aufbau einer UHV-MOKE-Messapparatur und Messungen von Eisenschichten auf Indiumarsenid und Galliumarsenid*, Diploma thesis, Ruhr-Universität Bochum, 2005
- [Vav00] P. Vavassori, Appl. Phys. Lett. **77**, 1605 - 1607, 2000
- [Veg21] L. Vegard, Z. Phys. **5**, 17, 1921
- [Ven73] J. A. Venables, Phil. Mag. **27**, 697 - 738, 1973
- [Ven84] J. A. Venables, Rep. Prog. Phys. **47**, 399 - 459, 1984
- [Ven94] J. A. Venables, Surf. Sci. **299/300**, 798 - 817, 1994
- [Voi99] W. Voigt, Ann. d. Phys. u. Chem. **303**, 345, 1899
- [Was05] G. Wastlbauer, J. A. C. Bland, Advances in Physics **54**, 137 - 219, 2005
- [Wal62] D. Walton, J. Chem. Phys. **37**, 2182, 1962
- [Web69] P. J. Webster, Contemp. Phys. **10**, 559 - 577, 1969
- [Wei07] P. Weiss, Journ. de Phys. **6**, 661 - 690, 1907
- [Wes07] A. Westphalen: *Advanced MOKE Investigations: Remagnetization Processes of Microsized Structures*, PhD thesis, Ruhr-Universität Bochum, 2007
- [Win08] L. Winking, M. Wenderoth, J. Homoth, S. Sievers, R. G. Ulbrich, Appl. Phys. Lett. **92**, 193102, 2008
- [Woo64] E. Wood, J. Appl. Phys. **35**, 1306 - 1312, 1964
- [Yan93] Z. J. Yang, M. R. Scheinfein, J. Appl. Phys. **74**, 6810 - 6823, 1993
- [Xu00] Y. B. Xu, D. J. Freeland, M. Tselepi, J. A. C. Bland, Phys. Rev. B **62**, 1167 - 1170, 2000
- [Xue95] Q. Xue, T. Hashizume, J. M. Zhou, T. Sakata, T. Ohno, T. Sakurai, Phys. Rev. Lett. **74**, 3177 - 3180, 1995
- [Xue97] Q. Xue, T. Hashizume, T. Sakurai, Prog. Surf. Sci. **56**, 1 - 131, 1997

- 
- [You96] C.-Y. You, S.-C. Shin, *Appl. Phys. Lett.* **69**, 1315 - 1317, 1996
- [Zak07] K. Zakeri, J. Lindner, I. Barsukov, R. Meckenstock, M. Farle, U. von Hörsten, H. Wende, W. Keune, J. Rucker, S. S. Kalarickal, K. Lenz, W. Kuch, K. Baberschke, Z. Frait, *Phys. Rev. B* **76**, 104416, 2007
- [Zut04] I. Žutić, J. Fabian, S. Das Sarma, *Rev. Mod. Phys.* **76**, 323 - 410, 2004

# Curriculum vitæ

## Personal details:

First name: Sani  
Family name: Noor  
Date of birth: 7 May 1975  
Place of birth: Düsseldorf  
Nationality: German  
Marital status: Single  
E-mail address: sani.noor@ruhr-uni-bochum.de

## Résumé:

09/1981 - 08/1985 Brüder-Grimm-Schule in Meerbusch (elementary school)  
09/1985 - 12/1985 Mataré-Gymnasium in Meerbusch (secondary school)  
01/1986 - 08/1994 German School Singapore, Abitur (A levels)  
10/1994 - 09/1995 Study of Musicology, Ruhr-Universität Bochum  
10/1995 - 04/1997 Study of Physics, Ruhr-Universität Bochum  
05/1997 - 02/1998 Military service  
04/1998 - 08/2007 Study of Physics, Ruhr-Universität Bochum,  
Diplom (Master equivalent)  
09/2007 - PhD student and research assistant,  
AG Oberflächenphysik, Experimentalphysik IV,  
Ruhr-Universität Bochum



# Acknowledgement

There are a number of people to whom I owe gratitude as they helped to contribute to an accomplishment of this work and whom I would like to mention here.

First and foremost, my thanks go to my advisor, Prof. Dr. Ulrich Köhler, who has given me the opportunity to be part of his group and to indulge in my doctoral studies. I sincerely appreciate his kindness, patience and help inside and outside of the lab.

I furthermore thank PD Dr. Oleg Petracic, who has also willingly agreed to be the second assessor of my thesis, for answering many questions in matters of magnetism. A substantial amount of measurements was done based on his expert knowledge and ideas.

Thanks also to Prof. Dr. Westerholt for helping to clarify various physical problems.

Perhaps most importantly, I would like to express my thanks to my former and current colleagues, Ralf Funke, Martin Kroll, Carsten Godde, Sebastian Frey, Samet Özkan, Hasmik Harutyunyan, Wera Fehl, Aniela Scheffzyk, Lina Elbers, Dietmar Rother, Stefan Borgsdorf and Daniel Laumann, for contributing to a good working atmosphere. At this point I would also like to thank Lina, Sebastian, Stefan and Daniel for proofreading this manuscript during the last DPG meeting. I apologize to my former colleagues that I could not convey their passion for table football to the next generation. Martin and Carsten, I wish you all the best for completing your theses.

Throughout my work I knew that I could always rely on the technicians of our group, Elisabeth Bartling and Conny Leschke, who so often managed to combine work with amusement. Seriously, I am grateful for all the little and bigger repairs and constructions they did or helped me with. In this context, I also thank Peter Stauche for his knowledge and advice on many experimental setups at EP IV, chemicals and safety issues and for being such a great entertainer at the same time.

I would also like to thank Claudia Wulf for handling administrative and related work in such an easy manner. Although experience has incorporated a certain amount of fear in me when approaching secretarial offices, this was not the case for Claudia. In fact, I was glad to stop by sometimes for a chat over coffee.

A huge thanks goes to the people of the workshop for precision mechanics, especially Volker Hegenberg who made many of my designs come alive and who was always spontaneous with his help often against the rules and regulations. Great thanks also to Michael Marx who completed the modifications of my setup in next to no time.

I would furthermore like to express my thanks to Detlef Rogalla and Hans-Werner Becker for the RBS measurements and analyses.

Thanks also to Igor Barsukov and Nikita Melnichak for the FMR measurements and Benjamin Geisler for providing the STM simulations.

Beside the people at work, I would like to mention the support of my friends and family. Thanks to my grandmother, uncle and aunt for always being there for me and literally being the closest family I have here. This shall not diminish the meaning of my parents, my brother and my sister who are just so far away. I hope that I will see you more often in the future.

At this point, I would also like to thank Pemi, Judith and Hanno for their understanding that I couldn't take part in the recent jam sessions due to the fact that I had to write this thesis.

Finally, thanks to Yu-Ying Hu for food and love.

Financial support by the Deutsche Forschungsgemeinschaft through the Sonderforschungsbereich 491 is gratefully acknowledged.